2018

Fundamentals Of Srcoo3 Based Oxygen-Deficient Perovskites As Cathodes For Solid Oxide Fuel Cells

Tianrang Yang
University of South Carolina - Columbia

FUNDAMENTALS OF $SrCoO_{3-\delta}$ BASED OXYGEN-DEFICIENT PEROVSKITES AS CATHODES FOR SOLID OXIDE FUEL CELLS

by

Tianrang Yang

Bachelor of Engineering
Chaohu University, 2011

Master of Engineering
University of Science and Technology Beijing, 2014

Submitted in Partial Fulfillment of the Requirements

For the Degree of Doctor of Philosophy in

Mechanical Engineering

College of Engineering and Computing

University of South Carolina

2018

Accepted by:

Kevin Huang, Major Professor

Ralph E. White, Committee Member

Thomas Vogt, Committee Member

Xinyu Huang, Committee Member

Cheryl L. Addy, Vice Provost and Dean of the Graduate School

DEDICATION

Dedicated to the memory of my grandmother,

Qingrong Tao,

who always loved me and had faith in me.

ACKNOWLEDGEMENTS

I would like to express my sincere appreciation to **Dr. Kevin Huang**, my academic advisor, mentor and friend. All my research work and publications at USC could not be done without his extraordinary guidance and efforts. His dedication to science and diligent working spirit have profoundly affected my professional life as a researcher, and beyond. When I lost the motivation to continue my research, Dr. Huang was there helping me. Overall, it has been a great pleasure working with Dr. Huang over the last three years.

I am indebted to **Dr. Thomas Vogt** for opening the door of resolving a crystal structure from neutron diffraction data, serving as my committee member, and the great help in my career. My sincere thanks go to **Dr. Ralph E. White** and **Dr. Xinyu Huang**, for their knowledge, encouragement and valuable time serving as my committee members. I also want to thank **Dr. Dong Ma**, **Dr. An Ke**, **Dr. Yan Chen**, **Dr. Ashfia Huq** at Oak Ridge National Lab and **Dr. Steven McIntosh** at Lehigh University for their help in conducting the *in-situ* neutron diffraction experiments and very useful discussions.

Dr. Jie Wang, **Dr. Nansheng Xu**, **Dr. Xinfang Jin**, **Ms. Allison H. Matthews**, **Dr. Libin Lei**, **Dr. Peng Zhang** and other members of SOFC center have offered great help to my research.

Finally, special thanks are due to my girlfriend, my parents and sisters. Without their unconditional love and endless support over the years, I would not be able to finish this dissertation.

ABSTRACT

The local structure and oxygen stoichiometry in oxide systems have a profound impact on oxygen electrocatalysis encountered in metal-air batteries and solid oxide fuel cells (SOFCs). However, this knowledge is often obtained under conditions different from the real working conditions of the material, resulting in misinterpretation and misunderstanding. This PhD dissertation aims to obtain the structure and oxygen-stoichiometry information of a class of perovskite oxides under their real working conditions in solid oxide fuel cells. Several perovskite oxides were selected for the study: $Sr_{0.9}Y_{0.1}CoO_{3-\delta}$ (SYC10), $Sr_{0.9}Y_{0.3}CoO_{3-\delta}$ (SYC30), $SrCo_{0.9}Nb_{0.1}O_{3-\delta}$ (SCN10) and $SrCo_{0.9}Ta_{0.1}O_{3-\delta}$ (SCT10).

The local crystal structure and oxygen stoichiometry of these materials were systematically characterized with *in-situ* neutron diffraction (ND). The oxygen stoichiometry was also measured by thermogravimetric analysis (TGA) and iodometric titration methods. To establish the correlation among structure, oxygen stoichiometry and oxygen reduction reaction (ORR) activity, high temperature electrochemical impedance spectroscopy, oxygen permeation and single cell testing were also performed. In chapter 2, SYC10 is described to have a more symmetrical structure and $V_o^{\cdot\cdot}$ distribution, and higher $V_o^{\cdot\cdot}$ concentration than SYC30. Molecular orbital energy analysis based on the local structure of the ORR-active Co1-polyhedra indicates SYC30 has a higher Fermi level

relative to O-2p energy level in the active Co1-polyhedra, and thus a higher motional enthalpy for $V_o^{\cdot\cdot}$ migration. However, the ORR activity of Y-doped $SrCoO_{3-\delta}$ (SCO) are found uncompetitive with other popular catalysts. In chapter 3 and 4, systematic structural studies are presented for Nb and Ta-doped SCO, namely SCN10 and SCT10, respectively. The methodology of unrevealing the structure-activity relationships in chapter 2 is also found applicable to SYC10, SCN10 and SCT10 as presented in chapter 5. The electrochemical tests indicate that SCT10 is the best catalyst due to its excellent thermal and electrochemical stability. In chapter 6, SCT10 is evaluated in a real solid oxide fuel cell in the form of nanoscaled SCT10 layer coating on the commercial $(La_{0.6}Sr_{0.4})_{0.95}Co_{0.2}Fe_{0.8}O_{3-\delta}$ (LSCF). The bilayer structured cathode shows excellent properties of coarsening-resistant, Sr-segregation-free and high ORR-activity.

TABLE OF CONTENTS

LIST OF TABLES

LIST OF FIGURES

LIST OF SYMBOLS

J_{O_2}	Oxygen permeation flux
$J_{V_O^{\cdot\cdot}}$	Oxygen vacancy permeation flux
$P_{O_2}^{s}$	Oxygen partial pressures at sweeping side surface
$P_{O_2}^{f}$	Oxygen partial pressures at feeding side surface
σ_e	Electronic conductivity
σ_i	Ionic conductivity
$\nabla \eta_{V_O^{\cdot\cdot}}$	Electrochemical potential gradient
$\nabla \mu_{V_O^{\cdot\cdot}}$	Chemical potential gradient
$\nabla \phi$	Electrostatic potential gradient
$\mathrm{a}_{V_O^{\cdot\cdot}}$	Activity of $V_O^{\cdot\cdot}$.
$D_{V_O^{\cdot\cdot}}$	Diffusion coefficient of $V_O^{\cdot\cdot}$.
$\mathrm{c}_{V_O^{\cdot\cdot}}$	Concentration of $V_O^{\cdot\cdot}$.
$\widetilde{D}_{V_O^{\cdot\cdot}}$	Chemical diffusion coefficient of $V_O^{\cdot\cdot}$
k_s	intrinsic rate constant of surface gas/oxygen-lattice exchange at sweeping side

LIST OF ABBREVIATIONS

ABE..... Average Bonding Energy

AO..... Atomic Orbital

BSCF..... $(Ba,Sr)(Co,Fe)O_{3-\delta}$

BVS..... Bond valence sums

EDX ..... Energy dispersive X-Ray spectroscopy

EIS..... Electrochemical impedance spectroscopy

FESEM.....Field emission scanning electron microscope

FIB ..... Focused ion beam

GDC20 ..... $Gd_{0.2}Ce_{0.8}O_{2-\delta}$

HRTEM.....High-resolution transmission electron microscope

LCAO.....Linear combination of atomic orbitals

LSCF ..... $(La,Sr)(Co,Fe)O_{3-\delta}$

LSM .....Sr-doped $LaMnO_3$

MIECs .....Mixed ionic and electronic conductors

MO .....Molecular orbital

ND.....Neutron diffraction

OCV .....Open circuit voltage

ORR .....Oxygen reduction reaction

R_p.....polarization resistance

RT.....Room temperature

SALC ..... Symmetry adapted linear combination

SCN10..... $SrCo_{0.9}Nb_{0.1}O_{3-\delta}$

SCO..... $SrCoO_{3-\delta}$

SCT05 ..... $SrCo_{0.95}Ta_{0.05}O_{3-\delta}$

SCT10 ..... $SrCo_{0.9}Ta_{0.1}O_{3-\delta}$

SOFC..... Solid oxide fuel cell

STEM..... Scanning transmission electron microscope

SYC10..... $Sr_{0.7}Y_{0.1}CoO_{3-\delta}$

SYC30..... $Sr_{0.7}Y_{0.3}CoO_{3-\delta}$

TEC .....Thermal expansion coefficient

TGA .....Thermogravimetric analysis

TPB .....Triple phase boundary

XPS ..... X-ray photoelectron spectroscopy

YSZ..... Y_2O_3 stabilized zirconia

CHAPTER 1

LITERATURE REVIEW

1.1 Motivation of Study

The world economy is projected to double with a growth rate averaging 3.4% over the next 20 years. The energy consumption is expected to increase from current 13 billion TOE (tonne of oil equivalent) to nearly 18 billion TOE by the year of 2035.[1] Oil, gas and coal remain the dominant sources of energy powering the global economy, which is obviously not sustainable due to their finite nature. In addition to the fast depletion, consuming those fossil fuels has generated a significant amount of polluting gases, such as CO_2, SO_x, NO_x, etc. The resulting climate change and environmental pollution looms a great threat to the prosperity of our planet.[2] These growing concerns act as a continued driving force to improve the energy efficiency, as well as finding green and sustainable energy sources. Giving another fact that the consumer preferences is shifting towards electricity as a fuel, which is clean and convenient at the point of use, extensive efforts have been put on new power generation techniques, such as wind farms, geothermal power plants, and solar cells. However, several drawbacks are preventing them from large scale application, such as location specific which are usually far from population centers and unstable nature due to characteristic weather fluctuations. The uncertainty in generation output add extra difficulties in grid balancing between electricity supply and demand. It presents

technological challenges in integrating those renewable power into the grid smoothly. The renewable power output variability is currently handled almost exclusively by conventional reserves, which is not sustainable as renewable penetration grows.[3] Hydrogen/fuel cell system offers a promising sustainable energy storage/conversion solution for those renewable power generation techniques. Hydrogen is not only clean and easily transportable but also of high energy density. Fuel cells are attractive energy converter because they are efficient, free of noise and vibration, reliable and entirely nonpolluting. They can power devices requiring power input ranging from a few milliwatts to megawatts due to the controllable power capacities. Hence, in hydrogen/fuel cell system renewable energy is stored in hydrogen while the fuel cell converts it back to electricity effectively.

1.2 Solid Oxide Fuel Cells

Among all the types of fuel cells, e.g., proton exchange membrane fuel cell (PEMFC), alkaline fuel cell (AFC), phosphoric acid fuel cell (PAFC) and molten carbonate fuel cell (MCFC), solid oxide fuel cell (SOFC) operates in the highest temperature range (500-1000 ^{o}C). High operating temperature promotes rapid electrochemistry processes and thus high system efficiency, reaching 55% when working alone and 70% when applying its high-temperature exhaust heat to gas turbine power generation.[4] Moreover, the high operation temperature renders SOFC the ability to handle not only hydrogen but also other common industrial fuels, such as reformed gas mixture (CO, H_2). This fuel flexibility offers SOFC another advantage of bridging the technological gap between currently common fossil energy and clean renewable energy in the future.

- 1.2.1 Operation Principles

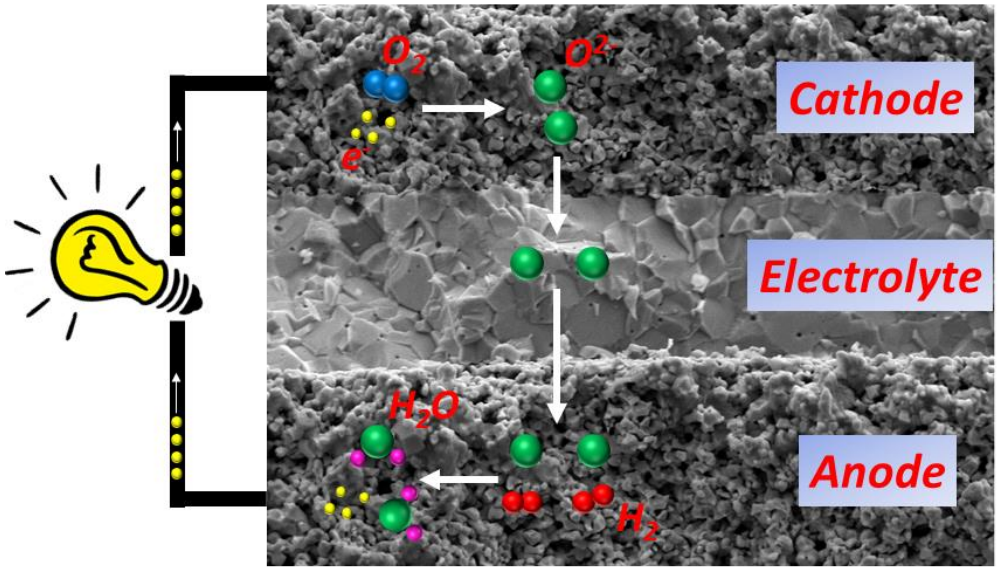

Figure 1.1 Schematic of SOFC working principle with H_2 as fuel and air as oxidant.

A single SOFC consist of porous anode, porous cathode, and dense electrolyte as illustrated in Figure 1.1. The key processes include oxidant reduction at cathode, fuel oxidation at anode and ions transportation through electrolyte. Electrons flow through external circuit from anode to cathode to keep charge balance. Air is typically supplied to cathode. The cathode obtains electrons from the external circuit and catalyzes the oxygen reduction reaction (ORR):

$$\frac{1}{2}O_2(\mathrm{g})+2\mathrm{e}^- \rightarrow O^{2-}(s) \tag{1-1}$$

Anode catalyzes the oxidation of fuel and releases the electrons to the external circuit. Depending on the fuel type, the half-cell reaction could be:

$$H_2(g)+O^{2-}(s) \rightarrow H_2O(g)+2e^- \tag{1-2}$$

$$CO(g)+O^{2-}(s) \rightarrow CO_2(g)+2e^- \tag{1-3}$$

The dense electrolyte separates the air and fuel. More importantly, it transports only oxygen-ion (negligible electrons pass through) from cathode to anode, and thus help development of an electrical potential to balance the chemical potential gradient.

- 1.2.2 Reversible Cell Potential and Polarization Losses

Reversible cell potential

The first law of thermodynamics states that the change in the internal energy (U) of a closed system equal to the heat (Q) being transferred to the system minus the work done by the system (W). The expression goes

$$dU = dQ - dW \tag{1-4}$$

The second law of thermodynamic tells us that the entropy change of a system is greater or equal than the transferred heat divided by the temperature (T) of the system as expressed in equation (1-5). The equality holds when the transfer of heat is reversible.

$$dS \geq \frac{dQ}{T} \tag{1-5}$$

The equation below defines the Gibbs free energyG,

$$G = U - TS + pV \tag{1-6}$$

where p and V are the system pressure and volume, respectively. We can write the Gibbs free energy change as

$$dG = dU - TdS - SdT + pdV + Vdp \tag{1-7}$$

Combine equation (1-4), (1-5) and (1-7):

$$dG \leq -dW - SdT + pdV + Vdp \tag{1-8}$$

For a system only involves electrical work under constant pressure and temperature,

$$dW_e \leq -dG \tag{1-9}$$

Hence, the maximum electrical work ($W_{e,\max}$) in a fuel cell under constant pressure and temperature can be obtained when all electrochemical reactions are reversible with no losses and is given by the negative of the Gibbs free energy change. For a reaction on a per-mole basis:

$$W_{e,\max} = -\Delta G_{rxn} \tag{1-10}$$

Table 1.1 The reversible cell potentials at standard pressure for a hydrogen-oxygen SOFC.

T (°C)	ΔG_{rxn} (J/mol)[5]	E_{rev} (V)
400	-210230	1.09
500	-204940	1.06
600	-199550	1.03
700	-194060	1.01
800	-188500	0.98
900	-182860	0.95
1000	-177150	0.92

The ΔG_{rxn} represents the change in Gibbs free energy of the reactants and the products for one molar reaction. The total charge (q) being carried by one molar of reaction is

$$q = nF \tag{1-11}$$

where n is the number of moles of electrons transferred and F is Faraday's constant. The maximum electrical work done by moving a charge of q under reversible electrical potential (E_{rev}) is

$$W_{e,\max} = qE_{rev} \tag{1-12}$$

Combine equations (1-10), (1-11) and (1-12),

$$\Delta G_{rxn} = -nFE_{rev} \tag{1-13}$$

For a hydrogen-oxygen SOFC, the total reaction is

$$H_2(g) + \frac{1}{2}O_2(g) \rightarrow H_2O(g) \tag{1-14}$$

Given the Gibbs energy change of reaction, n equals 2 and F equals 96485 C/mol, the reversible cell potentials at standard pressure in SOFC working temperature range are listed in Table 1.1.

Beyond the standard pressure condition, E_{rev} is connected to pressure and reversible cell voltage at standard condition (E_{rev}^{o}) through the Nernst equation:

$$E_{rev} = E_{rev}^{o} - \frac{RT}{2F}\ln\frac{P_{H_2O}}{P_{H_2}P_{O_2}^{\frac{1}{2}}} \tag{1-15}$$

Polarization losses

The real SOFC working electrical potential is always smaller than the reversible cell potential whenever a current pass through the cell. There are three major types of voltage losses: activation losses, ohmic losses and concentration losses.

The activation energy barrier in electrochemical reactions can be manipulated by varying the cell potential since charged species are involved either as reactants or products. Certain amount of the reversible cell voltage must be sacrificed to move an electrochemical reaction from its equilibrium toward a favored direction. The Butler-Volmer equation expresses the relation between half-cell activation overvoltage (η_{act}) and working current density. Even though Butler-Volmer is developed for single electron transfer reaction, it can generally serve as an excellent approximation for most single step electrochemical reactions and multistep electrochemical reactions inside which a rate limiting step is much slower than the rest steps.[6] Assuming the concentrations of reactant and product species at electrode are not affected by the net reaction rate, the expression goes

$$j = j_o(e^{\alpha nF\eta_{act}/(RT)} - e^{-(1-\alpha)nF\eta_{act}/(RT)}) \quad (1\text{-}16)$$

where j is current density; j_o is the exchange current density which denotes the reaction rate at equilibrium for forward or reverse electrode reaction; α is transfer coefficient (typically range from 0.2 to 0.5), the value of which depends on the symmetry of the activation barriers for forward and reverse electrode reaction. From equation (1-16), it is not hard to find that the activation overpotential greatly depends on the size of j_o.

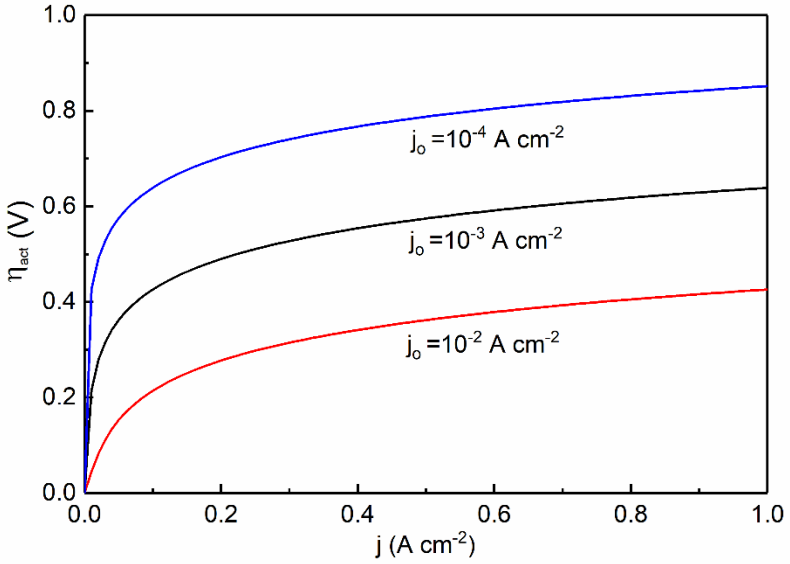

Figure 1.2 Effect of j_o on activation overpotential. Curves calculated with α =0.5, n =2 and T =1073 K.

Figure 1.2 better illustrate the effect of j_o on the activation overpotential, where α, n and T are fixed at 0.5, 2 and 1073 K, respectively. The required overpotential is lower as well as the electrode losses with a larger exchange current density. The effective ways to increase exchange current density include increase in the temperature, decrease in the activation barrier, and increase in the number of possible reaction sites. For SOFCs, the activation polarization is dominated by the oxygen reduction reaction (ORR) at the cathode as hydrogen oxidation at anode is usually very fast. The materials choice of electrolyte

limits the working temperature. Hence, it's important to develop cathode with high catalytic activity and more active sites.

Ohmic losses are caused by ionic and electronic conduction. When those charged species are transported, a voltage drop exists and its value at a given current flow can be calculated by Ohm's law:

$$\eta_{Ohm} = j \times ASR \tag{1-17}$$

where ASR denotes the area specific resistance with unit Ω cm^2.

Concentration losses happened when the mass transport of reactant across the reaction interfaces is insufficient compared to consumption rate. Reactant depletion decrease both the Nernst cell voltage and the kinetic reaction rate. Thus, the depletion of reactant at those active sites leads to losses in fuel cell output voltage. The concentration polarization overpotential (η_{con}) can be expressed as

$$\eta_{con} = \frac{RT}{nF} \ln(1 - \frac{j}{j_{lc}}) \tag{1-18}$$

where j_{lc} is the limiting current density. j_{lc} is the current density at maximum mass transfer rate when assuming the reactant concentration at interfaces is zero. The concentration polarization is normally negligible at low current densities. Concentration losses at cathode are typically much more severe than that for anode at a given thickness. This is because air is often supplied to cathode and O_2 diffuses much slower than H_2.

1.3 Oxygen-deficient Perovskites for Intermediate-temperature Solid Oxide Fuel Cell Cathode

Recent development of solid oxide fuel cell (SOFC) technology has been mostly concentrated on materials advancement aiming to enable high power generation at reduced temperatures with improved durability and cost. A key material being actively developed is mixed ionic and electronic conductors (MIECs) that can catalyze the sluggish ORR at cathode side. The intrinsic mixed ionic/electronic conduction in single-phase MIECs can significantly expand the number of ORR reactive sites from triple-phase boundaries (3PBs) to two-phase boundaries (2PBs)[7-8], thus substantially enhancing the ORR activity. This is in marked contrast with those of only electron-conducting cathodes (*e.g.* Sr-doped $LaMnO_3$ (LSM)[9]) or bi-phasic cathodes comprised of an electron-conducting (*e.g.* LSM) and an ion-conducting phase (*e.g.* Y_2O_3-stabilized zirconia or YSZ)[10], both of which have limited ORR-active sites near 3PBs regions and a low ionic/electronic conductivity. There are several new materials been proposed, such as perovskite-type [$(Sm,Sr)CoO_{3-\delta}$[11-12], $(Ba,Sr)(Co,Fe)O_{3-\delta}$ (BSCF)[13-15], $(La,Sr)(Co,Fe)O_{3-\delta}$ (LSCF)[16-18]], layered perovskite-related K_2NiF_4 ($Ln_2NiO_{4+\delta}$, Ln=La, Pr, Nd[19-21]) and ordered double perovskites ($AA'Co_2O_{5+\delta}$, A=rare earth or Y, A'=Ba, Sr)[22-24]. All these newly proposed perovskites or its related structures contain rare earth or alkaline ions at A-site and transition metal ions at B-site. The different combinations of cations at A and B-sites can result in the generation of oxygen vacancies ($V_O^{\bullet\bullet}$) or interstitial oxygen ($O_i^{''}$). These are of great importance for ionic conduction since they are the charge carriers. The electronic conductivity of perovskites originates from the interaction between transition metal ion at B-site and its surrounding oxygen-ion. The electronic structure is also tunable through cation substitution

even from insulating to metallic.[25] More importantly, the ORR activity in perovskite is greatly affected by the defects state and electronic structure since they closely relate to the oxygen species adsorption, migration and charge transfer process, etc.[26] In this section, the basics of electronic and ionic conduction in perovskite are explained. Then, a brief discussion is given to understand the ORR activity and its relationship with electronic structure and defects properties for oxygen-deficient perovskites.

- 1.3.1 General Structure Consideration

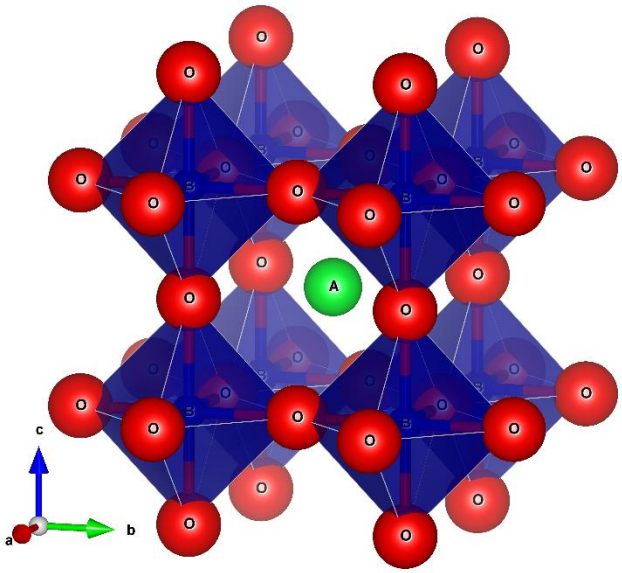

Figure 1.3 Crystal structure of Pm-3m perovskite.

The perovskite structure has the general formula ABO_3. A and B can adopt various charge combination, such as +1/+5, +2/+4, +3/+3, or even mixed charge ions sit on the same site. This compositional flexibility leads to versatile crystal symmetry. Fortunately, most of this diversity can be rationalized in terms of its highest symmetry Pm-3m (space group #221). Figure 1.3 shows its space-filling polyhedral structure. Each B-ion is coordinated by six oxygen-ion and thus form a BO_6 octahedra. The octahedra are corner connected to each other in a regular and parallel way. All the B-O bond lengths are equal, and the bond angle

of O-B-O is either 180 º or 90 º. The larger A-ion is surrounded by BO_6 octahedra and sits in the center of a cuboctahedra cage formed by 12 oxygen-ion. The above structure can also be described in the way of close packing. Every A-ion is surrounded by six oxygen-ion in (111) plane, as shown in Figure 1.4. The (111) planes stack along the cell body diagonal direction in a sequence …1/2/3/1'/2'/3'/1''… as shown in Figure 1.5. The same number means they shift in no other but the stack direction. When ignoring the size difference between A- and oxygen-ion, this stacking manner is exactly the so-called cubic close packing (CCP). The small B-ion are accommodated into the octahedral gap formed only by oxygen-ion in those close packed layers.

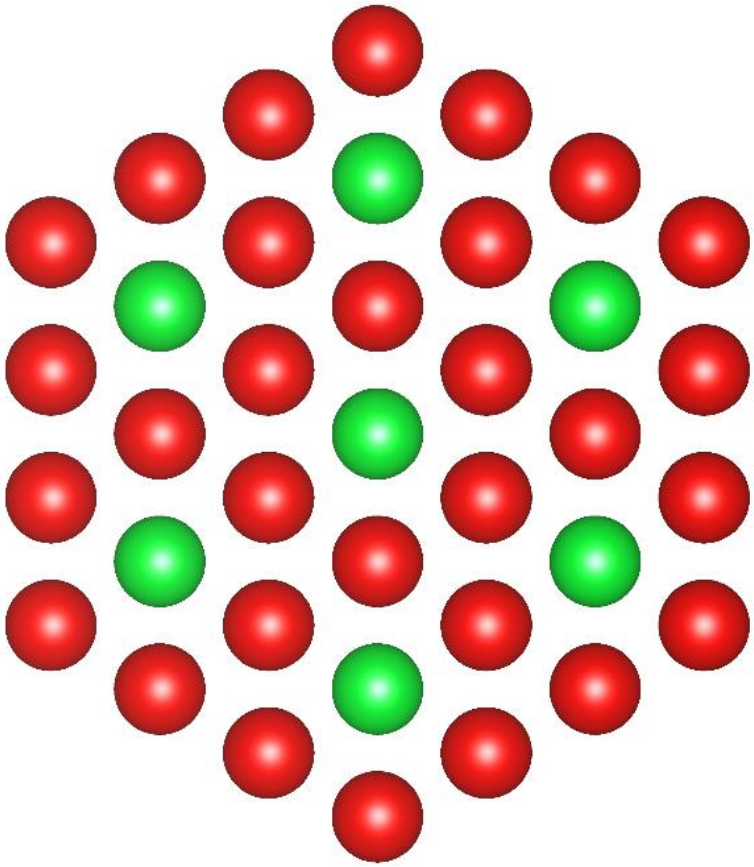

Figure 1.4 A-ion (Green) and oxygen-ion (red) arrangement in (111) plane of Pm-3m perovskite. The plane is drawn in an arbitrary size.

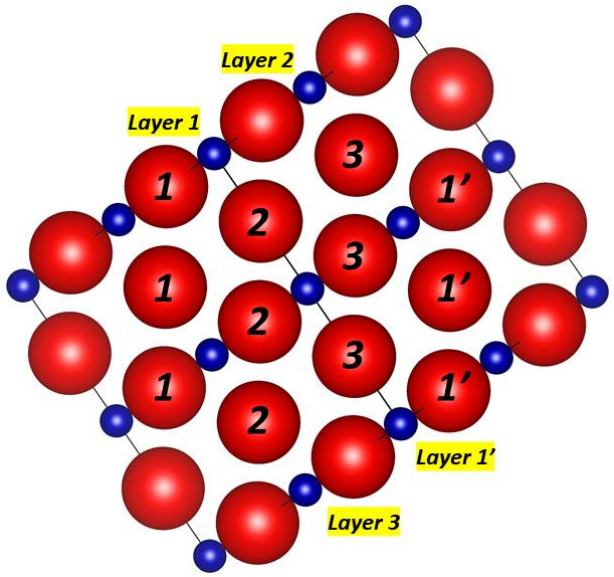

Figure 1.5 View normal to cell body diagonal [111] along (111) lattice plane for a 2×2×2 supercell of Pm-3m perovskite unit cell.

When treating perovskite as pure ionic compound, it is not hard to calculate the ion radius relation in a Pm-3m perovskite that

$$R_A + R_O = \sqrt{2}(R_B + R_O) \tag{1-19}$$

Only very limited amount of compositions satisfies the above requirement. The tolerance factor t is introduced to describe the ionic radii deviation, which goes

$$t = \frac{R_A + R_O}{\sqrt{2}(R_B + R_O)} \tag{1-20}$$

It is suggested that perovskite structure can be obtained only in certain range of t. Non-perovskite structures are preferred when t >1 or <0.71.[27] A hexagonal packing is preferred when t >1 because B-ion is too small to support a corner shared BO_6 octahedra, leading to face sharing BO_6 arrangement. Both A-ion and B-ion are small compared to oxygen-ion and they can both fit into the octahedral sites in those close packing layers of oxygen-ion

when t<0.71. In this case, either corundum structure (hexagonal close packing of oxygen with 2/3 of the octahedra-site being filled by A- or B-ion randomly) or ordered corundum structure (ilmenite, A- and B-ion occur in alternate layer) is formed. A Pm-3m perovskite structure is still possible when $0.9 < t < 1.0$. When t is even smaller in the range of 0.71-0.9, cooperative rotations of BO_6 octahedra occur to reduce the A-ion site volume so it can better fit in the small A-ion. These rotations will lower the symmetry, e.g. rotation about the [111] axis give rhombohedral R-3c symmetry; rotation about [110] axis give orthorhombic Pbnm or Pnma symmetry.[28] It should be noted that the tolerance factor is only a rough estimate since perovskites are not truly ionic compounds and the values of which also depend on the choices of ionic radii. Furthermore, more than one structure are often found for a perovskite with a given composition depending on temperature and preparation methods.

- 1.3.2 Electronic structure

Atomic Orbital (AO) of d-electron

In principle, the exact solution of the Schrödinger equation allows one to determine all the properties concerning the structure, energetics, and dynamics of a molecule. However, it is hardly possible at present to obtain the exact solution for a multi-atom system. The problem of electronic structure can be simplified by introducing approximations. One of the commonly used approaches is the so-called one-electron approximation, which assumes that each electron in an atom moves independently in the mean field created by the rest matters of this system (nuclei, other electrons). The wave function of atomic orbital (AO) can be solved and presented in a more understandable way under this assumption. The solution goes

$$\psi_{lmn} = R_{nl}(r)Y_{lm}(\theta,\phi) \tag{1-21}$$

where $R(r)$ is the radial wavefunction and $Y(\theta,\phi)$ is the angular wavefunction; r, θ and ϕ are spherical coordinates; l, m and n are those three quantum numbers (principle quantum number, angular quantum number, magnetic quantum number). Radial wave function depends only on the distance (r) from the nucleus while angular wave function depends upon directions, and in effect, describe the shape of an orbital. It should be noted that the angular wave functions for all s, all p or all d are the same regardless of the principal quantum number n. Hence, different s, p or d orbital has the same general shape, but the energy and size grow with the principal quantum number, such as 1s < 2s < 3s. The atomic orbital shape is important in MO theory because it determines how to choose the bases for the linear combinations of atomic orbitals in constructing molecular orbitals (MOs). The atomic orbitals of interests for most oxygen-deficient perovskites p (l=1) and d (l=2) orbitals. Figure 1.6 shows their shapes.[29] The sign in each lobe, either + or -, dictates whether the wave functions of adjacent electrons can interfere with each other constructively or destructively. The wave functions of these AOs have the same transformation properties under symmetry operations (mirror, rotation, etc.) with their subscripts x, y, z, x^2-y^2, etc. in a Cartesian coordination system.

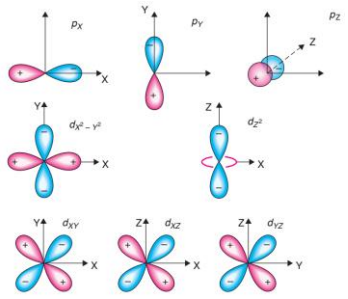

Figure 1.6 The shapes of three p and five d orbitals. The origin is at the nucleus.[29]

Molecular Orbital (MO) analysis of perovskite

It is easily seen that the electrons in AOs are localized around nuclei. In the conventional valence bond theory, all bonds are two-center bonds between two atoms. The concept of hybridization in valence bond theory somehow extends the AOs to the entire molecular. Take methane (CH_4) as an example, the three 2p AOs and the 2s AO on carbon atom cannot be arranged spatially in the form of a tetrahedron because of the mutual perpendicularity of 2p AOs (Figure 1.6) and the spherical symmetry of the 2s AO. Following the hybridization those four AOs are combined to give four equivalent sp^3 hybrid AOs arranged tetrahedrally, which can overlap with the adjacent 1s AOs of hydrogen atoms leading to covalent bond. But still, the electrons are treated localized at the bonds and any interactions between such bonds are not considered in valence bond theory. However, MO theory does not take localization as a postulate when treating the orbital mixing. All MOs of a polyatomic system in general extend over the entire system, which means that the electrons occupying these orbitals may be delocalized throughout the system. MO theory is initially developed for organic complexes. It is also called ligand field theory when applying MO method to transition metal complexes, which is perovskite in our case.

The one-electron approximation is also a priori in MO theory, which assumes that each electron moves independently in the mean field created by the nuclei and remaining electrons. The evaluation of MO under the one-electron approximation is still a complicated problem. Its wavefunction ϕ is commonly simplified in the form of linear combination of atomic orbitals (LCAO):

$$\phi(r) = \sum_i c_i \psi_i(r) \tag{1-22}$$

where ψ_i is the *i*th one-electron atomic wavefunction; c_i are coefficients. The LCAO means that each MO electron can be found at each atom of the system with a probability of $|c_i|^2$; it moves as a usual atomic electron when it is near the given atom. Before constructing the MOs for perovskites, it is beneficial to look at how the AOs interact with each other to form delocalized MOs in diatomic molecule H_2. The 1s atomic wavefunctions of those two hydrogen atoms can interact either constructively or destructively to form equal number of MOs. Constructive interfering gives bonding MO (σ_s) while destructive interfering gives antibonding MO (σ_s^*). The bonding MO orbital results in increased electron density between the two nuclei. It is more stable and has lower energy than the two separate atomic orbitals. The anti-bonding MO results in a node (at which the electron density is zero and the wavefunction change sign) between the two nuclei and is of greater energy than the two separate atomic orbitals. The MO diagram is shown in Figure 1.7. The MOs formed by two s atomic orbitals in which the associated electron density is concentrated in the space between adjacent atoms are referred to as σ orbitals. If the principal overlap regions are not along the line connecting atomic nuclei, the resulted MOs are referred to as π orbitals. The π orbitals overlap side-by-side which is less than that of end-on-end along the bond axis in σ orbitals. As a result, the π orbital will be higher in energy.

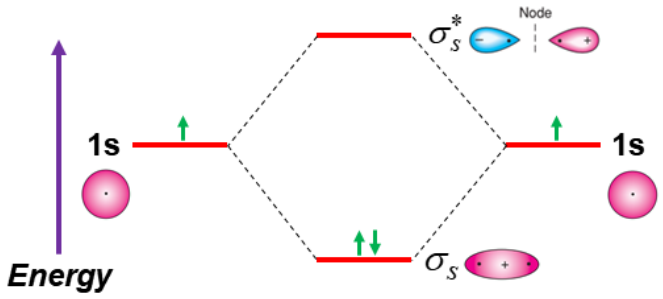

Figure 1.7 MOs diagram of H_2.

Another general rule of forming MOs is that the AOs are of similar energy. For instance, 1s orbitals will not combine with 2s or 2p orbitals to form MOs. For most perovskite of interests in SOFC cathodes, the valence electrons of A-site ions (5s for Sr, 6s for Ba, 4f, 5d or 6s for lanthanides) are much higher in energy than those of B-site atom (first row transition metal, 3d and 4s) and oxygen-ion (2p). As a result, the valence AOs of A-site atom are mostly localized and well removed from Fermi level.[30] Therefore, the orbitals of A-site atom do not play any significant role in determining the electronic structure and are usually omitted when constructing the MOs. The main difference will be the overlap extent between AOs as the octahedra has different size. It is also important to consider the symmetry when using MO LCAO method. With a specific symmetry point group, group theory analysis can determine the possible MOs. Table 1.2 shows character table of O_h point group, to which the BO_6 octahedra belongs in cubic perovskite. At the upper left is the symbol for the point group. The top row shows the symmetry operations of the point group, such as identity, proper rotation, mirror, etc. The left column gives the Mulliken symbols for each of the irreducible representations. “A”, “E” and “T” represent non-degenerate, double-degenerate and triple-degenerate, respectively. “g” or “u” subscripts denote symmetric or antisymmetric with respect to inversion operation (i). Subscript “1” or “2” denote symmetric or antisymmetric with respect to a vertical mirror plane perpendicular to the principal axis (σ_v or σ_d). The rows at the center of the table give the characters of the irreducible representations. The certain functions listed at right showing the irreducible representation for which the function can serve as a basis. When a MO belongs to A_{1g}, it means that MO can serve as a basis for A_{1g}; the MO transforms under symmetry operations as A_{1g}. Here the symmetry allowed MOs are directly presented

without detailed group theory analysis. The symmetry allowed σ MOs in O_h point group are A_{1g}, E_g and T_{1u}. Both AOs on B-site atom and oxygen atom should match the symmetry above to form MOs. The AOs of B-site atom fall into the categories from Table 1.2 as follow:

A_{1g}: s (s orbital on central atom always transform as totally symmetric representation hence not included in character table)

E_g: $(d_{z^2}, d_{x^2-y^2})$

T_{1u}: (p_x, p_y, p_z)

The 2p AOs of six oxygen atoms are linear combined under symmetry restrictions, which is also called symmetry adapted linear combination (SALC) to form orbitals of corresponding symmetry. The oxygen atom SALCs are

A_{1g}: $\frac{1}{\sqrt{6}}(\psi_1+\psi_2+\psi_3+\psi_4+\psi_5+\psi_6)$

E_g: $\frac{1}{\sqrt{12}}(2\psi_5+2\psi_6-\psi_1-\psi_2-\psi_3-\psi_4)$, $\frac{1}{2}(\psi_1-\psi_2+\psi_3-\psi_4)$

T_{1u}: $\frac{1}{\sqrt{2}}(\psi_1-\psi_3), \frac{1}{\sqrt{2}}(\psi_2-\psi_4), \frac{1}{\sqrt{2}}(\psi_5-\psi_6)$

Table 1.2 Character table of O_h point group

O_h	E	$8C_3$	$6C_2$	$6C_4$	$3C_4^2$	i	$6S_4$	$8S_6$	$3\sigma_h$	$6\sigma_d$		
A_{1g}	+1	+1	+1	+1	+1	+1	+1	+1	+1	+1	-	$x^2+y^2+z^2$
A_{2g}	+1	+1	-1	-1	+1	+1	-1	+1	+1	-1	-	-
E_g	+2	-1	0	0	+2	+2	0	-1	+2	0	-	(z^2, x^2-y^2)
T_{1g}	+3	0	-1	+1	-1	+3	+1	0	-1	-1	(R_x, R_y, R_z)	-
T_{2g}	+3	0	+1	-1	-1	+3	-1	0	-1	+1	-	(xz, yz, xy)
A_{1u}	+1	+1	+1	+1	+1	-1	-1	-1	-1	-1	-	-
A_{2u}	+1	+1	-1	-1	+1	-1	+1	-1	-1	+1	-	-
E_u	+2	-1	0	0	+2	-2	0	+1	-2	0	-	-
T_{1u}	+3	0	-1	+1	-1	-3	-1	0	+1	+1	(x, y, z)	-

T_{2u}	+3	0	+1	-1	-1	-3	+1	0	+1	-1	-	-

The bonding and antibonding MOs are constructed by bringing the AOs of B-site atom and the SALCs of oxygen atom 2p AOs together to give positive overlap and negative overlap. The energies of MOs generally follow the number of nodes; the lowest always has no nodes and is fully bonding, the highest has nodes between each pair of atoms and is thus fully antibonding. The bonding and anti-bonding MOs have the same symmetry, but their energies will go down and up by the same amount at a first approximation. The energies of various σ SALCs are viewed the same because the direct interaction of oxygen 2p AOs can be treated as negligible.[31] The σ MO diagram is thus constructed in Figure 1.8 as red lines.

The symmetry allowed π MOs in O_h point group are T_{2g}, T_{1u}, T_{1g} and T_{2u}. It can be seen from Table 1.2 that T_{1g} and T_{2u} AOs are not available on B atom. For T_{1u} AOs, they mainly form σ MOs which is stronger than π MOs. Hence, the π SALCs T_{1u}, T_{1g} and T_{2u} are non-bonding orbitals. T_{2g} SALCs are left to form bonding and anti-bonding π MOs with those three T_{2g} AOs of B atom. The π MOs diagram is displayed in Figure 1.8 as blue lines.

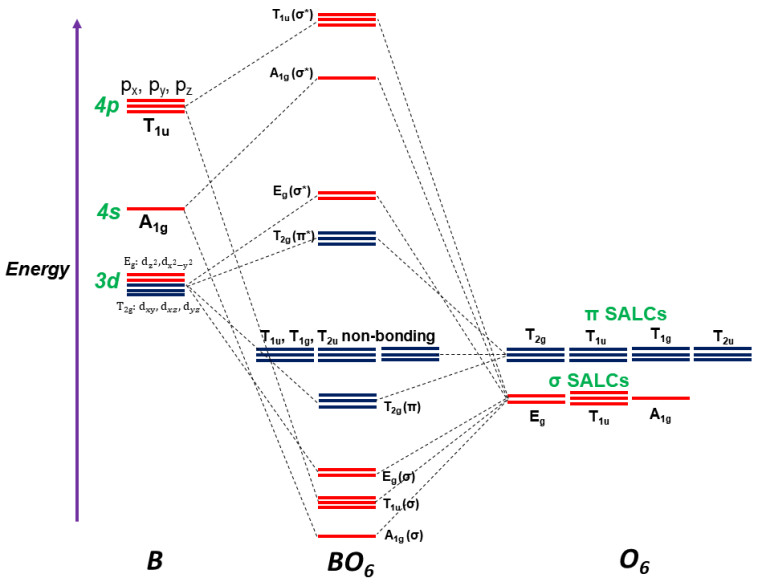

Figure 1.8 MO diagram for BO_6 in a cubic perovskite.

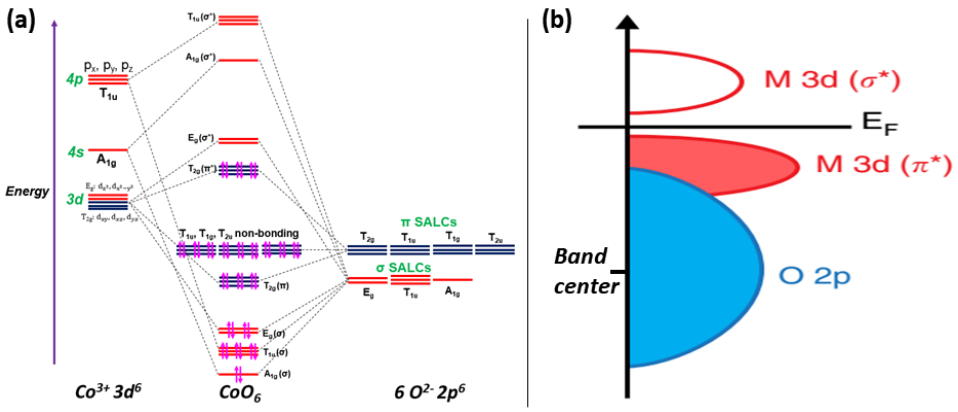

Figure 1.9 (a) Electronic configuration of octahedral $Co^{3+}O_6$; (b)[32] band structure of $LaCo^{3+}O_3$.

The molecular orbital analysis above explains the nature of metal-oxygen bond in perovskite to the best without any computation. As seen from Figure 1.8, the energies of O-2p orbitals lie below those of the metal orbitals. The bonding combination are dominated by the ligand, while the antibonding combination will be predominantly metal in character. The bonding between metal and oxygen orbitals stabilize O-2p orbitals while destabilize the metal orbitals. The metal E_g orbitals ($d_{z^2}, d_{x^2-y^2}$) form σ bond with O-2p orbitals which have higher overlap than that of π bond between T_{2g} (d_{xy}, d_{xz}, d_{yz}) and O-2p orbitals. Hence, the metal E_g orbitals (σ^*) are more destabilized and higher in energy than T_{2g} orbitals (π^*). Take $Co^{3+}O_6$ as an example, the total number of valence electrons are 42 (6 electrons from Co^{3+} and 36 electrons from six O^{2-}) and the electrons fill into MOs following Hund's rule. Its electronic structure at low spin state is shown in Figure 1.9 (a). The highest occupied molecular orbital (HOMO) is antibonding π orbital T_{2g} and the lowest unoccupied molecular orbital is antibonding σ orbital E_g, which correspond to valence band and conduction band respectively when extending to 3D in solids. The Fermi level lie between those two MOs as shown in Figure 1.9 (b).

- 1.3.3 Electronic structure, defects, and catalytic activity

ORR mechanisms

Two various pathways for ORR are illustrated in Figure 1.10.[33] In "bulk pathway" the ORR happens over the entire electrode surface and the formed oxygen ions diffuse from electrode to electrolyte through bulk. In "surface pathway", the adsorbed oxygen first diffuse and then reacts at triple phase boundary (TPB), the electrode/electrolyte/gas interface. The ORR mainly takes place through "bulk pathway" for a MIEC material. The surface exchange coefficient (k^*) and bulk chemical diffusion coefficient (D_{chem}) are essential for efficient cathode processes. The bulk oxygen diffusion in perovskites are well understood and can be evaluated with various methods, such as ^{18}O isotope tracer diffusion or oxygen permeation test. The surface exchange process usually becomes the performance-limiting considering the commonly used thin cathode architecture. A higher k^* value correspond to more rapid splitting of oxygen and incorporation into the cathode, which in turns correlates with a better ORR performance. However, attempts to understanding the surface reaction mechanism on perovskite have faced major challenges due to the complexity of materials and difficulties in performing *in-situ* surface characterization. Most of the insightful understanding of reaction mechanism at atomic/molecular level come from computational techniques. The general steps of the surface reaction include oxygen adsorption, dissociation, charger transfer and incorporation into the lattice.[26, 33-35] Gaseous oxygen is first adsorbed molecularly on the surface without dissociation. The electronic state of molecular oxygen being chemisorbed can be superoxide (O_2^-) or peroxide (O_2^{2-}).[36] Then, the adsorbed species dissociate into two

O^- bonded to surface. Finally, O^- meets with oxygen vacancies to be further reduced to lattice oxygen-ion O^{2-}.

The (001) surface are generally most stable in perovskites.[36-37] The MnO_2 and FeO_2 termination has been predicted to be the most stable ones under SOFC operation conditions for $LaMnO_3$[34] and $LaFeO_3$[38], respectively. Two types of chemisorbed dioxygen, which are O_2^- and O_2^{2-}, have been observed by diffuse reflectance Fourier transformed infrared spectrometry on the surface of LSM in 773-873 K.[39] Ab initio calculations predict that the stable adsorbates are O_2^- for $LaBO_3$ (B=Mn, Fe and Co) at (001) BO_2 surface.[36] No clear difference in adsorption energies are found for different B-ions. DFT computations for $LaMnO_3$ show that both the chemisorption of O_2^- and O_2^{2-} are exothermic while O_2^- has higher surface coverage.

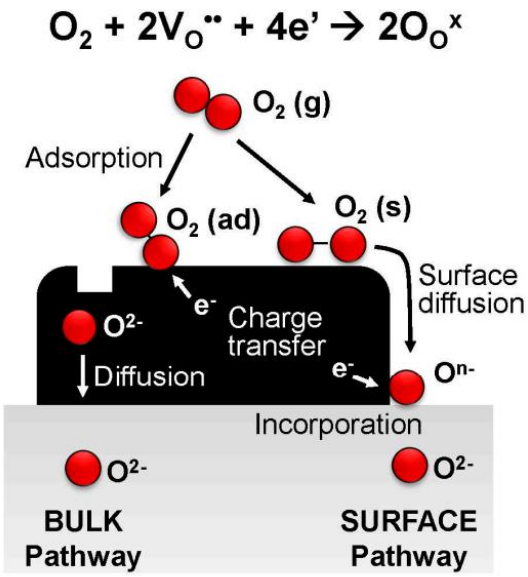

Figure 1.10 Two ORR pathways in SOFC cathode.[33]

The adsorption of molecular oxygen on the surface is the initial step of the surface reactions, which is also generally assumed to be fast.[35] The following steps for

conventional cathode LSM and the state-of-the-art BSCF and LSCF will be compared here. The dissociation of superoxide (O_2^-) or peroxide (O_2^{2-}) into two O^- can occur with or without the active participation of $V_O^{\cdot\cdot}$. The $V_O^{\cdot\cdot}$ formation energy is as high as 1.6 eV even at 1100 K resulting in very limited amount of surface $V_O^{\cdot\cdot}$ for LSM.[40] Computational calculation predicts an energy barrier of 0.6 eV for the adsorbates dissociation on a perfect surface without surface $V_O^{\cdot\cdot}$.[34] The step after dissociation is incorporate O^- into the lattice as O^{2-}before which the O^- have to encounter with a $V_O^{\cdot\cdot}$. The migration along the surface is much easier for $V_O^{\cdot\cdot}$ (0.7 eV) than that for O^- (2.0 eV).[35] The subsequent charge transfer after meeting each other occurs without barrier. Thus, the rate-limiting step is more likely to be the adsorbates dissociation on a perfect surface or the surface $V_O^{\cdot\cdot}$ migration for LSM. Both BSCF and LSCF have much higher $V_O^{\cdot\cdot}$ concentration than LSM. Hence, the dissociation process mainly occurs with the assistance of $V_O^{\cdot\cdot}$. Figure 1.11[33] shows the suggested surface reaction processes for BSCF. After gas oxygen being fast chemisorbed on the surface (I), the $V_O^{\cdot\cdot}$ migrates toward the adsorbates (O_2^- or O_2^{2-}) (II). The dissociation of dioxygen adsorbates first incorporates one oxygen atom into lattice O^{2-} and release an O^- (III). The approach of another $V_O^{\cdot\cdot}$ to the O^- and incorporating into the lattice is the last step (IV). The charge transfer reaction in step III and IV is expected to occur fast with negligible barrier.[33, 35, 40] The $V_O^{\cdot\cdot}$ migration in step II and IV is slower step while the larger coverage of O^- than O_2^- or O_2^{2-} leaves the rate-limiting step being step II.[34] LSCF is found to have higher $V_O^{\cdot\cdot}$ migration barrier than BSCF with the ×20 lower bulk mobility at 1000 K.[41] It is reasonable to assume that the surface $V_O^{\cdot\cdot}$ migration is much

slower on LSCF than BSCF. Hence, the surface reaction process of LSCF is different from BSCF that the adsorbates prefer to migrate towards $V_O^{\cdot\cdot}$, which is much slower than the reverse migration in BSCF.

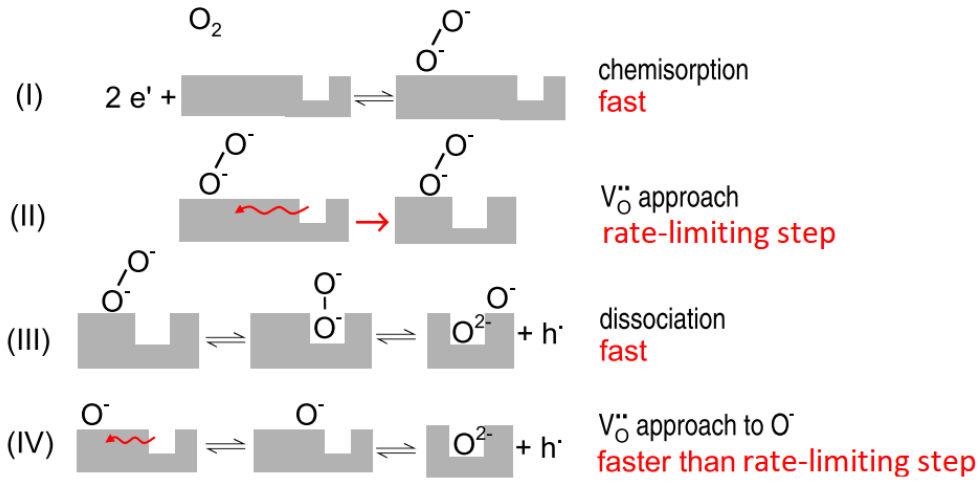

Figure 1.11 Surface reaction mechanism for BSCF.[33]

Electronic structure and catalytic activity

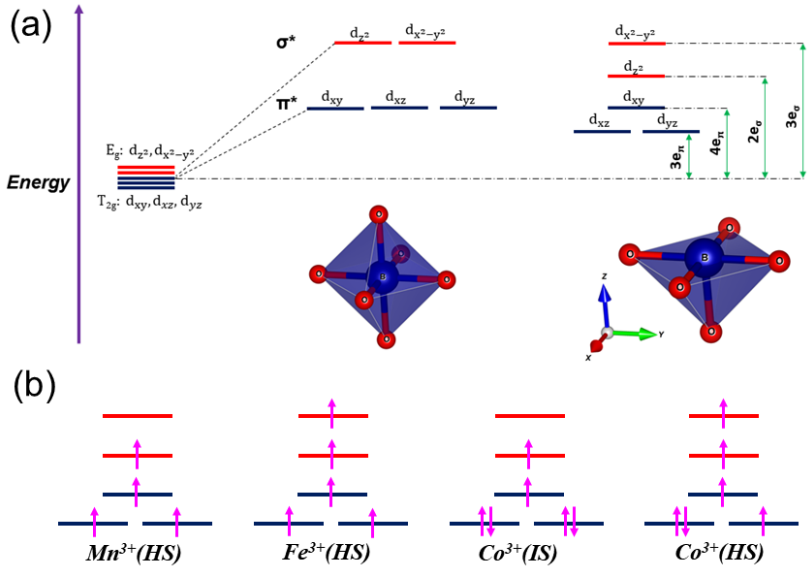

Figure 1.12 (a) Metal d-orbitals splitting energy diagram in cubic BO_6 and BO_5. e_σ and e_π are the orbital energy changes at maximum overlap for σ and π bond, respectively; (b) d electronic configurations for several transition metal ions.

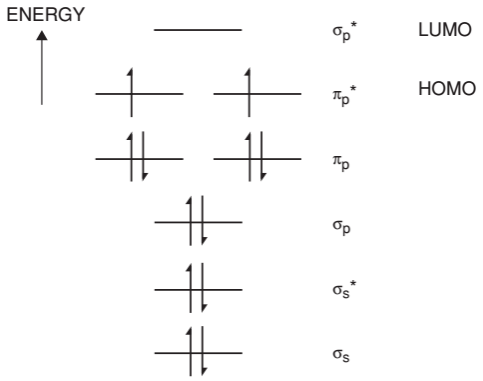

Figure 1.13 MO diagram of O_2.

The driving force of oxygen molecular adsorption atop B-site ion are the binding energy originating from the frontier orbitals interaction between each other. The coordination symmetry at surface is slightly different from bulk that it has coordination symmetry of BO_5. The impacts of coordination geometries on metal d orbitals energies or degeneracies can be estimated by simple crystal field theory or, in a more accurate form, angular overlap model in MO theory.[42] The BO_5 geometry further splitting E_g and T_{2g} orbitals as shown in Figure 1.12 (a). The spin-state reported at SOFC operating temperature for popular B-site ions are HS ($T_{2g}^3E_g^1$), HS ($T_{2g}^3E_g^2$), IS/HS ($T_{2g}^5E_g^1/T_{2g}^4E_g^2$) for ($Mn^{3+}$)[43], ($Fe^{3+}$)[44] and ($Co^{3+}$)[45], respectively. Their electronic configurations at surface are shown in Figure 1.12 (b). The frontier orbital (HOMO) is E_g (σ^*) which has different symmetry with that of oxygen molecule as its HOMO is π_p^* as shown in Figure 1.13.[29] Hence, their frontier orbitals can only partially overlap with oxygen π_p^* in a tilted configuration. For surface reaction in aqueous environments, the strength of this interaction determines its reaction kinetics. If the interaction is too weak, O_2^{2-}/OH^- exchange is limiting step; if the interaction is too strong, the O^{2-} removal is difficult and the rate is limited by the generation of OH^-.[46] The

strength of this adsorbate binding can be approximated by the amount of E_g occupancies, with lower filling corresponding to stronger interaction. For example, the B-O_2 binding is too strong for $LaCrO_3$ ($T_{2g}^3 E_g^0$) while too weak for $LaFeO_3$; the intermediate interaction strength for $LaMnO_3$, $LaCoO_3$ results in a peak of ORR activity in aqueous solution for perovskites.[46-47]

However, the surface reaction activity at SOFC working conditions cannot be simply predicted from E_g occupancies. On the one hand, the B-site ion covers an extended range of oxidation states from +2 to +4 because of the oxygen non-stoichiometry variation with temperature and the commonly existed charge disproportion. On the other hand, the kinetics of the limiting-step may not directly correlate with the surface binding energies. Recently Morgan's group found that the experimental surface exchange coefficient k^* are strongly correlated with the first-principle calculated O-2p center (relative to the Fermi energy).[48-50] Figure 1.14 shows such a correlation that the surface exchange reaction is faster when O-2p band center is higher, relative to Fermi level. The correlation demonstrates that O-2p center controls the rate-limiting step behind the oxygen surface reaction even though it is a bulk property. It can be easily seen from the ORR mechanism above that the oxygen species transport dominates the surface reaction kinetics, as well as bulk diffusion process. When oxygen species transport to adjacent position in bulk or on the surface, the O-2p state energy at original position is decreased with respect to the metal-3d states along with an increase of Fermi energy level. The reaction energies correlate with the number of interchanged electrons between the Fermi level and O-2p band level. In addition, the $V_O^{\cdot\cdot}$ formation energy and hopping activation energy are also linearly

correlated with the bulk O-2p band center. Hence, it is not surprising that a higher ionic conductivity will typically exhibit a faster surface reaction as they are close related.

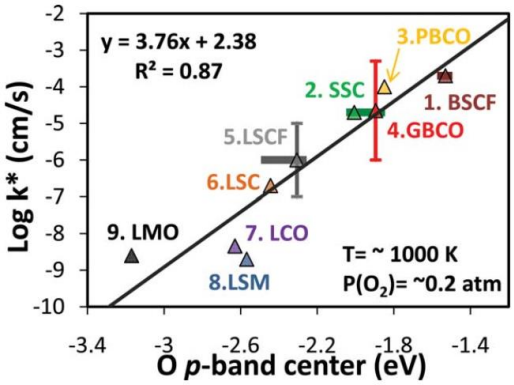

Figure 1.14 Experimental surface exchange coefficient vs the O-2p band center for popular cathode materials.[48]

1.4 $SrCoO_{3-\delta}$ based Oxygen-deficient Perovskite as a SOFC cathode

Recently, the perovskite materials $SrCoO_{3-\delta}$ (SCO) have garnered much attention as a class of new high-performance cathode materials for intermediate-temperature (IT)-SOFCs.[51-58] However, the crystal structure of a pure SCO depends exquisitely on its thermal history during synthesis. At ambient air conditions, for example, a slow cooling results in a mixture of spinel Co_3O_4 and 2H-$BaNiO_3$-related $Sr_6Co_5O_{15}$;[59] the latter has CoO_6 octahedra stacked in columns sharing faces instead of corners in the ideal 3C-type cubic perovskite structure.[60] By quenching SCO from temperatures ≥ 1000 °C to room temperature (RT), however, an orthorhombic brownmillerite phase $SrCoO_{2.5}$ can be obtained.[61-62] The crystal structure of $SrCoO_{2.5}$ is a 3C-type perovskite related superstructure, in which half the oxygen vacancies per formula unit are in long-range ordering.[63] Further, oxygen vacancies in the brownmillerite are oxygen-intercalatable, thereby resulting in a series of oxygen-

stoichiometry-dependent crystal structures.[64-66] For example, using an electrochemical oxidation technique, Le Toquin *et al* have shown that the oxygen stoichiometry of $SrCoO_{3-\delta}$ can be varied between 2.5 and 3.0.[64] Hu *et al* showed that $SrCoO_{2.5}$ thin films can be chemically oxidized to $SrCoO_3$ by NaClO and the oxygen intercalation stability and dynamics in $SrCoO_{3-\delta}$ films can be even tuned by epitaxial strains.[66-67] On the other hand, it is interesting to observe that the crystal symmetry of $SrCoO_{3-\delta}$ also varies systematically with 3-δ, *i.e.* from orthorhombic at 3-δ=2.5 to cubic at 3-δ=2.75, and tetragonal at 3-δ=2.75-2.89 and again cubic at 3-δ=3.0.[64] The material with 3-δ=3.0 crystallizes as an ideal 3C-cubic perovskite structure. A higher crystal symmetry in $SrCoO_{3-\delta}$ is favored for use in oxygen electrocatalysis since such materials usually have a higher electronic conductivity and oxygen diffusivity with low activation energies.

However, the 3C-cubic perovskite phase of SCO is not chemically stable below ~900 ^{o}C. The phase stability for an ABO_3 perovskite can be empirically assessed by the Goldschmidt tolerance factor. For $SrCoO_3$, t=1.04,[68] which is larger than the ideal value (t=1.00) for the 3C-cubic structure, suggesting that the 3C-cubic symmetry in $SrCoO_3$ may not be structurally favorable. To reduce the *t*-value, a partial substitution of Sr^{2+} with smaller cations such as La^{3+},[51] Ce^{3+},[52] Sm^{3+}[53] and Y^{3+}[54] or a partial substitution of $Co^{3+/4+}$ with larger cations such as Sb^{5+},[55] Mo^{6+},[56] Ta^{5+}[57] and Nb^{5+}[58, 69] has been experimentally proven as an effective way to stabilize the 3C-type perovskite structure at RT. Jiang et al. report that $Sr_{0.9}Y_{0.1}CoO_{3-\delta}$ has a single cubic structure with a stable polarization resistance of 0.6 Ω cm^2 at 600 ^{o}C.[54] $SrCo_{0.9}Nb_{0.1}O_{3-\delta}$ has been reported with 8 times lower polarization resistance than the state-of-the-art cathode $(La_{0.60}Sr_{0.40})_{0.95}(Co_{0.20}Fe_{0.80})O_{3-\delta}$ (LSCF) at 600 ^{o}C, 0.75 Ω cm^2 *vs* 6.00 Ω cm^2 and improved thermodynamic stability compared to

benchmark cathode $Ba_{0.5}Sr_{0.5}Co_{0.8}Fe_{0.2}O_{3-\delta}$ (BSCF).[58, 68] Li, et al. report $SrCo_{0.9}Ta_{0.2}O_{3-\delta}$ shows an even better ORR activity and stability than $SrCo_{0.9}Nb_{0.2}O_{3-\delta}$.[70] However, the knowledge of structure, oxygen stoichiometry and Co-ion oxidation state in SOFC working temperature range are still missing; a fundamental understanding of the structure-activity relationship are still needed for these doped-SCOs.

Another challenge for SCO-based perovskites to be used as practical cathodes is its much higher thermal expansion coefficient (TEC, >20 ppm K^{-1}) when compared to the electrolyte (~10 ppm K^{-1}). A direct use of SCO-based materials in SOFC as a bulk cathode is, therefore, inadequate. To solve this issue, the ORR-active, but TEC-high SCO-based materials, are usually utilized as a cathode in the form of nanoparticles impregnated into a TEC-compatible scaffold.[71-73] In this design, TEC of the cathode is determined by the scaffold, not the attached nanoparticles.

1.5 Objectives

Since SOFC cathode operates at elevated temperatures, the knowledge of the local structure and oxygen stoichiometry at such temperatures would be more meaningful than that under ambient temperature to interpret the ORR activity. Systematic study on temperature-dependent local crystal structure by *in-situ* neutron diffraction (ND) for Y-doped SCO at Sr-site (A-site) and Nb- or Ta-doped at Co-site (B-site), is one of the primary works in this dissertation. To complement ND results, conventional thermogravimetric analysis (TGA) and iodometric titration for oxygen non-stoichiometry, oxygen permeation for oxide-ion conduction and impedance spectroscopy for polarization resistance are also carried out. With these fundamental data in hand, attempts are made to correlate their crystal structures,

electronic structures and defect states with the ionic conduction, electronic conduction and oxygen reduction reaction (ORR) activity. A reasonable and practical approach to utilize SCO-based materials in SOFC cathode is incorporating them into a TEC-compatible scaffold. Infiltration is an easy and production friendly way to enable the formation of active particles onto the backbone without significantly changing the current SOFC manufacturing process or adding too much cost. Therefore, SCO-based materials infiltrated cathode are prepared and evaluated to examine their suitability for commercial SOFC. Overall, the goals of this dissertation can be summarized as below,

- Obtain detailed local structure information at elevated temperatures for these doped-SCOs,
- Establish the structure-activity relationships,
- Evaluate the cathode performance in an engineering-feasible way in SOFCs.

CHAPTER 2

Y-DOPED $SrCoO_{3-\delta}$ AS CATHODE FOR SOLID OXIDE FUEL CELLS

2.1 Introduction

The oxygen-deficient $SrCoO_{3-\delta}$-based perovskites have been extensively studied in the past for their extraordinary oxygen reduction/evolution (ORR/OER) activities[7, 74-79]. Recently, a new type of ordered perovskite $Sr_{0.7}R_{0.3}CoO_{3-\delta}$ (SRC30, R=Y [80-81], Ho [82-83]) have been proposed as an ORR active material operated on Co^{3+}/Co^{2+} redox couple rather than the common Co^{4+}/Co^{3+} as in $La_{1-x}Sr_xCoO_{3-\delta}$ with high electronic and oxygen-ion conduction above 600 ºC. Goodenough *et al.* reported that the polarization resistance of $Sr_{0.7}Y_{0.3}CoO_{3-\delta}$ (SYC30) in a solid oxide fuel cell (SOFC) is 0.11 Ω cm^2 and the maximum power density reaches 927 mW cm^{-2} with a 300-μm thick LSGM ($La_{0.8}Sr_{0.2}Ga_{0.83}Mg_{0.17}O_{2.815}$)-supported single cell at 800 ºC.[81] The performance of $Sr_{0.7}Ho_{0.3}CoO_{3-\delta}$ (SHC30) as a SOFC cathode is very close to that of SYC30 with a polarization resistance of 0.14 Ω cm^2 and power density of 756 mW cm^{-2} under the same conditions.[83] Resolved by Synchrotron X-ray Diffraction (SXRD) and Neutron Diffraction (ND),[80-82, 84-86] the room temperature (RT) crystal structure of SRC30 is shown in Figure 2.1 (a), consisting of alternate corner-sharing layers of ($Co1O_4$/$Co1O_5$) and $Co2O_6$ polyhedra with a new type ordering of oxygen vacancies ($V_o^{\cdot\cdot}$) and a larger tetragonal unit cell, 2a×2a×4a (a: cell parameter of cubic

perovskite, space group I4/mmm, #139). The four O4-sites in the Co1-layer can only be quarter-occupied because of their close proximity.[80] The structures of SRC30 at high temperatures have also been studied by ND [81-82]. However, the refined structures by these studies contain the O4-site with an occupancy of ~0.4, which is physically impossible. In addition, Y_2O_3 was also found as a minor impurity in SYC30[80-81], but the impact of this second-phase on the parent composition has not been discussed.[80-81]

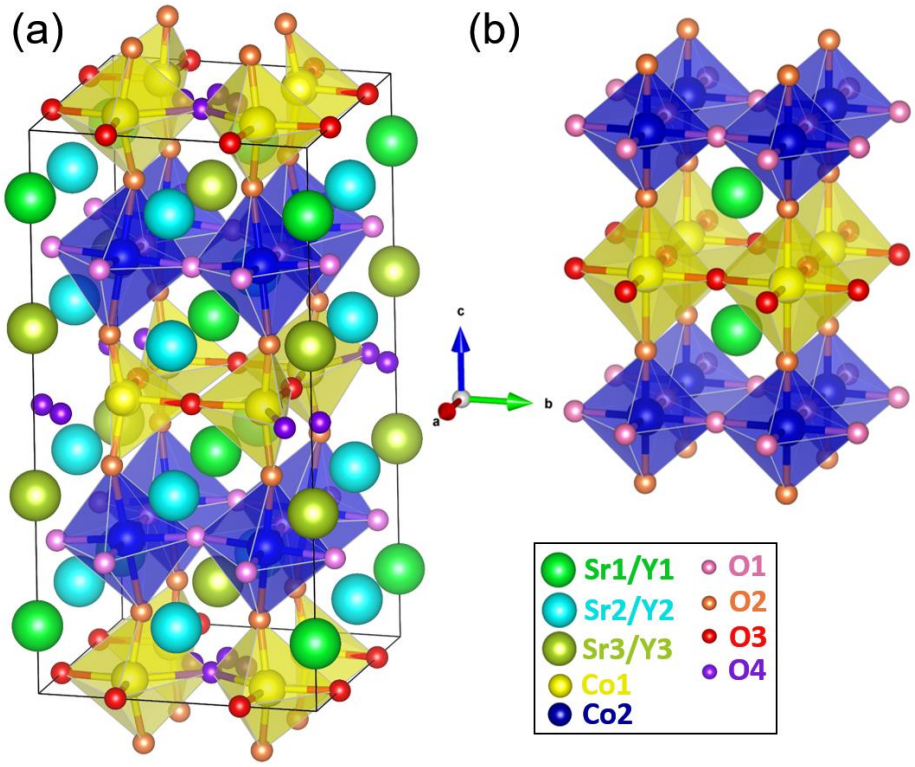

Figure 2.1 Unit cell of RT crystal structure of (a) SYC30 (S.G I4/mmm) and (b) SYC10 (S. G. P4/mmm).

Previously, we have reported a systematic study on temperature-dependent crystal structure, oxygen stoichiometry, and electrical/electrochemical properties of $Sr_{0.7}Y_{0.1}CoO_{3-\delta}$ (SYC10) as an active ORR catalyst by *in situ* ND and electrochemical impedance spectroscopy.[87] The study found that SYC10 as shown in Figure 2.1 (b) also crystalizes

into a tetragonal structure at RT, but with a smaller unit cell a×a×2a and a different space group (P4/mmm, #123). Like SYC30, SYC10 contains corner-sharing polyhedra of oxygen-saturated Co2-layer and oxygen-deficient Co1-layer, alternatively stacked along [001] direction. The difference, however, is that the polyhedra in SYC30 are tilted, while those in SYC10 are not. This structural difference is represented by the new atomic positions of Sr/Y (Sr2/Y2, Sr3/Y3) and O (O4) appeared in SYC30.

The focus of this chapter is to describe acquisition of the important structural properties of SYC30 at high temperatures by ND and Rietveld refinement, and present a deeper understanding of the structure.[88-89] The obtained structural information such as crystal symmetry, local atomic positions, cobalt oxidation states, oxygen occupancies of SYC30 are then closely compared with those of SYC10, from which those key structural differences determining oxide-ion transport as well as ORR activity are identified. The ORR polarization resistance and fuel cell performance of SYC30 are finally characterized and compared with SYC10, by which the structure-activity relationships are established for the SYC-based materials.

2.2 Experimental

- 2.2.1 Sample synthesis

The SYC30 were prepared by solid-state reaction method. Stoichiometry amounts of $SrCO_3$ (≥99.9%, Aldrich), Co_3O_4 (99.7%, Alfa Aesar) and Y_2O_3 (99.9%, Alfa Aesar) were first weighed, mixed, ball-milled in ethanol for 3 h, dried and pelletized. To make the phase as pure as possible, we adopted two calcination steps: 1) 1000 ^oC for 12 h; 2) 1050 ^oC for another 12 h. Between each calcination, the pellets were broken up and ball-milled for 3 h.

The final products were obtained by burying in the same powder and sintering at 1230 ºC for 10 h.

- 2.2.2 *In-situ* Neutron diffraction

In-situ Neutron diffraction (ND) experiments were conducted at VULCAN, the time-of-flight Engineering Diffractometer at the Spallation Neutron Source in Oak Ridge National Laboratory.[90-91] ND was performed from RT to 900 ºC on pellet samples (17 mm in diameter and 10 mm thick) to ensure strong diffraction intensity. A 5×10×5 mm^3 beam gauge volume was determined by the incident slits and receiving collimators. Diffraction data were collected continuously from each sample contained in an MgO crucible inside an air-ambient furnace during heating and cooling. The heating rate was 10 ºC min^{-1} below 300 ºC and 5 ºC min^{-1} between 300 and 900 ºC, while the cooling rate was 10 ºC min^{-1} from 900 ºC to *ca.* 150 ºC. During heating, the sample was held at RT for 1 h, 300 ºC for 3 h, 500 ºC for 2h, 700 ºC for 2h and 900 ºC for 2h. Only the last 1-h data (total neutron counts of 4×10^6) at each isothermal holding stage were used for the Rietveld refinement. The refinement was conducted with GSAS program/EXPGUI interface.[92-93] A refinement typically started with trials and errors using the model-free Le Bail method.[94] The background was fitted with a shifted Chebyshev polynomial function. The Pseudo-Voigt function with Finger-Cox-Jephcoat correction was used for peak profile asymmetry correction. The DIFA (one of the three parameters defining the relationship between measured time-of-flight and d-spacing[92]), unit cell, background and profile parameters obtained from Le Bail fitting were used as the initial inputs in Rietveld refinement and kept fixed at the first stage. Scaling factors, atomic positions, isotropic thermal displacement parameters and absorption coefficients were then refined separately. Following that, all the

fixed parameters were released and refined together. Oxygen occupancies were the outcomes of the final several runs. The oxygen stoichiometries were calculated from occupancies and site multiplicities. The temperature-independent DIFA and absorption coefficients were fixed at a same value for the measured temperature range. All the structural models are drawn with Vesta 3.0.[95]

- 2.2.3 Iodometric titration

The initial oxygen stoichiometry (3-δ) at RT was also determined by iodometric titration in addition to the Rietveld refinement of ND data. A 30-ml diluted HCl solution (1 M) was first purged with pure N_2 to eliminate the dissolved O_2 and Cl_2. A 50-mg powder was then dissolved in above solution under the bubbling N_2, after which 10-ml, 0.2M KI solution was added to reduce $Co^{3+/4+}$ to Co^{2+} and release elementary iodine shown in reaction (2-1). A 0.01-M $Na_2S_2O_3$ solution was then added dropwise to react with elementary iodine produced via reaction (2-2). Several drops of saturated starch solution were used to indicate the titration endpoint by a sudden color change.

$$Co^{(2+n)+} + nI^- = Co^{2+} + \frac{n}{2} I_2 \quad (2\text{-}1)$$

$$I_2 + 2S_2O_3^{2-} = 2I^- + S_4O_6^{2-} \quad (2\text{-}2)$$

The concentration of the $Na_2S_2O_3$ solution was predetermined by dissolving 25 mg $K_2Cr_2O_7$ powder in a diluted HCl solution under N_2. A 10-ml, 0.2 M KI solution was then added into the solution, where $Cr_2O_7^{2-}$ is expected to be fully reduced to Cr^{3+} by KI via reaction (2-3). The produced elementary iodine was titrated with $Na_2S_2O_3$ solution. The concentration of $Na_2S_2O_3$ and the average Co-ion oxidation state of the samples were then calculated based on the charge balance between reaction (2-1), (2-2) and (2-3). The oxygen stoichiometry can be then derived based on the charge neutrality.

$$Cr_2O_7^{2-} + 6I^- + 14H^+ = 2Cr^{3+} + 3I_2 + 7H_2O \quad (2\text{-}3)$$

- 2.2.4 Thermogravimetric analysis

A NETZSCH STA 448 TGA/DSC (Germany) thermal analyzer was used for thermogravimetric analysis (TGA). Approximately 50-mg powder was placed in an alumina crucible under a flow of 60 ml min^{-1} air. The sample was held first at a reference state of 70 ºC for 2 h to remove the absorbed H_2O, followed by ramping the same temperature regime as that used for *ND*. From the weight change, the oxygen stoichiometry as a function of temperature can then be mapped out with the initial oxygen stoichiometry from iodine titration.

- 2.2.5 Polarization resistance measurement

The polarization resistance of SYC30 as a cathode of solid oxide fuel cell was evaluated with symmetrical cell consisting of SYC30/GDC20 ($Gd_{0.2}Ce_{0.8}O_{2-\delta}$, Fuel Cell Materials)/SYC30 from 600 ºC to 800 ºC during heating in a step of 50 ºC and a P_{O_2} range of 0.01 to 0.5 atm by electrochemical impedance spectroscopy (EIS). Cathode paste was obtained by mixing SYC30 powder with V-006A (Heraeus) in weight ratio of 1:3. The paste was then screen-printed on both side of 500 μm GDC20 dense pellet, followed by firing at 1100 ºC for 2 h. The effective electrode area was 0.712 cm^2. Silver paste and silver mesh were used as current collectors. EIS data were collected with 1470/1455B Solartron electrochemical station in a frequency range of 0.01 Hz-1 MHz and AC amplitude of 10 mV. The EIS data were analyzed with equivalent circuit method by ZSimpWin_Demo software.

- 2.2.6 Fuel cell performance evaluation

Anode-supported cells with a GDC10+NiO as the anode, GDC10 as the electrolyte and SYC30 as the cathode. To make the anode support, NiO (J.T. Baker), GDC10 and carbon black (Fisher Chemical) in a weight ratio of 6:4:2 were first ball milled for 3 h with ethanol, followed by drying, pelleting with 5 wt% PVB (Polyvinyl butyral, Sigma Aldrich) and firing at 800 ºC for 2 h. Thus obtained, partially sintered pellets were used as anode substrates, on which a thin-film GDC10 electrolyte was deposited. The deposition of GDC10 thin film was achieved by dip coating of a GDC10 suspension made in the following steps: a 10-g GDC10 powder was first ball milled in 28.5-g ethanol solvent, 0.4-g PVB binder, 0.3-g TEA (Triethanolamine, Alfa Aesar) dispersant, 0.37-g PEG600 (Polyethylene glycol-600, Alfa Aesar) and 0.37-g DBP (Dibutyl phthalate, Acros Organics) plasticizer for 24 h. A 200-µL suspension (corresponding to 40 µm-thickness) was then dropped on top of the anode substrate with a single-channel pipettor (100-1000 µL). The bilayer strcuture was then dried at room temperature for 2 h before sintering at 1500 ºC for 6 h. The cathodes and current collectors were finally coated on top of the sintered electrolyte/anode in the same way as symmetrical cells. The effective cathode surface area was 0.33 cm^2. For fuel cell testing, a mixture of 3 vol% H_2O/97 vol% H_2 was supplied to the anode surface as fuel at a flow rate of 100 mL/min, while cathode was exposed to static air. Current-voltage (IV) as well as current-power (IP) curves were obtained from sweeping the voltage from open circuit voltage (OCV) to 0.3 V at a sweep rate of 20 mV/s. The measurements were taken isothermally at 600 and 700 ºC.

2.3 Results and discussion

- 2.3.1 Structural features of SYC30

The RT structures

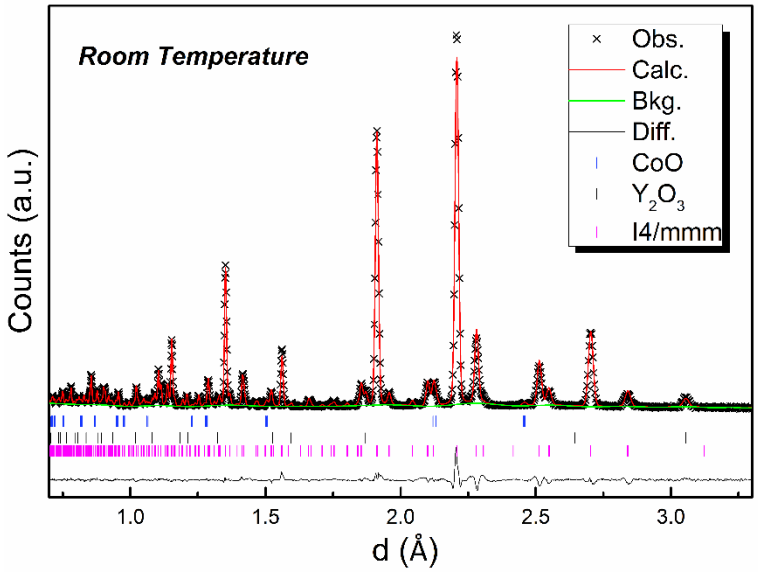

Figure 2.2 The RT Rietveld refinement profile of SYC30.

The initial room-temperature (RT) structure model for the Rietveld refinement was taken the same as Figure 2.1 (a) with S.G. I4/mmm.[80] The refinement profile of ND patterns is presented in Figure 2.2 with all structural parameters listed in Table 2.1. For every O4-site, the structure is found to have four adjacent equivalent positions. Only one of these four positions are physically allowed to be occupied, thus leading to the maximum O4-site occupancy of 0.25. Therefore, the O4-occupany of 0.37 reported in ref.[81] is questionable. The value of 0.236 obtained in this work agrees well with 0.23 reported in ref.[80] and is within a reasonable range from a structural perspective. Since only one of the four adjacent O4 positions is occupied, the polyhedra in the Co1 layer should be represented by two $Co1O_5$ pentahedra and two $Co1O_4$ tetrahedra. Cation ordering has also been reported from

synchrotron XRD and electron diffraction for close compositions to SYC30, where Y^{3+} is determined to have a 9-coordination at Sr3-site.[84-85] However, it is not possible to determine the positions of Sr^{2+} and Y^{3+} with ND due to their close scattering lengths (7.02 fm for Sr^{2+} and 7.75 fm for Y^{3+}).[96] The much shorter Sr3-O shown in Table 2.2 seems to suggest the Sr3-site preference for Y^{3+} as Y^{3+} has a smaller radius. A small amount of CoO and Y_2O_3 as second phases is also found in SYC30 by the refinement.

Table 2.1 Unit cell, atomic positions, occupancies, thermal displacement factors and reliable factors determined from Rietveld refinement of SYC30, S.G. I4/mmm, Z=16.

Parameters	RT	300 ºC	500 ºC	700 ºC	900 ºC
a (Å)	7.6426(3)	7.6721(2)	7.6994(2)	7.7306(2)	7.7723(1)
c (Å)	15.3092(9)	15.4115(7)	15.4750(6)	15.5437(6)	15.6238(5)
V (Å^3)	894.21(9)	907.13(3)	917.38(3)	928.93(4)	943.81(5)
			Sr1/Y1 *4e* (0, 0, ~0.875)		
z	0.8798(4)	0.8785(6)	0.8768(6)	0.8706(5)	0.8688(4)
100×U_{iso} (Å^2)	2.3(1)	2.9(2)	3.5(2)	3.4(2)	3.8(1)
f_{occ}*			0.7/0.3		
			Sr2/Y2 *8g* (0, 1/2, ~0.875)		
z	0.8669(2)	0.8670(3)	0.8674(3)	0.8693(3)	0.8687(2)
100×U_{iso} (Å^2)	1.08(7)	1.25(9)	1.8(1)	2.5(1)	2.48(6)
f_{occ}*			0.7/0.3		
			Sr3/Y3 *4e* (0, 0, ~0.375)		
z	0.3512(3)	0.3520(3)	0.3528(4)	0.3518(4)	0.3508(3)
100×U_{iso} (Å^2)	1.1(1)	1.4(2)	1.5(2)	1.9(1)	2.5(1)
f_{occ}*			0.7/0.3		
			Co1 *8h* (*x*=*y*; ~0.75, ~0.75, 0)		
x	0.7470(6)	0.7474(7)	0.7472(8)	0.7497(7)	0.7535(7)
100×U_{iso} (Å^2)	1.1(2)	1.2(2)	2.0(2)	2.6(3)	2.7(2)
f_{occ}*			1.0		
			Co2 *8f* (1/4, 3/4, 1/4)		
100×U_{iso} (Å^2)	1.1(2)	1.6(2)	1.5(2)	1.8(2)	1.9(2)
f_{occ}*			1.0		
			O1 *16n* (0, ~0.25, ~0.25)		

y	0.2443(3)	0.2443(4)	0.2446(4)	0.2570(5)	0.2567(5)
z	0.2397(2)	0.2393(3)	0.2394(3)	0.2384(3)	0.2381(2)
$100\times U_{iso}$ (Å^2)	1.11(5)	1.10(8)	1.66(7)	2.0(1)	2.25(4)
f_{occ}	0.989(5)	0.979(11)	0.992(12)	1.0*	1.0*
		O2 *16m* (*x*=*y*; ~0.25, ~0.25, ~0.125)			
x	0.2866(3)	0.2878(3)	0.2880(3)	0.2902(3)	0.2908(2)
z	0.1173(2)	0.1168(3)	0.1166(3)	0.1167(3)	0.1161(2)
$100\times U_{iso}$ (Å^2)	2.71(8)	2.9(1)	3.2(2)	3.6(2)	3.9(7)
f_{occ}	0.997(8)	1.0*	0.958(17)	0.985(16)	0.950(6)
		O3 *8i* (0, ~0.75, 0)			
y	0.7212(5)	0.7232(7)	0.7228(8)	0.7521(10)	0.7518(10)
$100\times U_{iso}$ (Å^2)	1.4(1)	1.3(2)	1.5(2)	2.6(2)	3.1(1)
f_{occ}	0.966(9)	0.887(17)	0.874(18)	0.768(19)	0.764(8)
		O4 *8j* (*x*, 1/2, 0)			
x	0.4054(2)	0.4219(23)	0.4242(22)	0.424(4)	0.4273(30)
$100\times U_{iso}$ (Å^2)	2.2(7)	2.0(9)	2.1(4)	2.2(6)	2.4(9)
f_{occ}	0.236(10)	0.225(17)	0.236(14)	0.152(14)	0.137(10)
		O4' *8j* (*x*', 1/2, 0)			
x	-	0.326(5)	0.321(4)	0.3197(35)	0.3211(19)
$100\times U_{iso}$ (Å^2)	-	2.2(5)	2.4(8)	2.4(4)	2.5(5)
f_{occ}	-	0.136(16)	0.150(13)	0.257(13)	0.269(10)
		Reliability factors			
R_{wp} (%)	3.82	3.93	3.47	3.08	3.08
R_p (%)	2.86	2.77	2.50	2.28	2.28
χ^2	7.86	4.61	3.54	2.91	2.90

* Fixed.

Table 2.2 Metal-oxygen lengths from Rietveld refinements for SYC30.

Bonds (Å)	RT	300 ºC	500 ºC	700 ºC	900 ºC
Sr1/Y1-O1(×4)	2.614(6)	2.610(8)	2.604(8)	2.611(7)	2.601(5)
Sr1/Y1-O2(×4)	3.0978(28)	3.1237(35)	3.137(4)	3.179(4)	3.2048(26)
Sr1/Y1-O3(×4)	2.815(5)	2.831(7)	2.862(8)	2.778(8)	2.815(7)
Average	2.842	2.855	2.868	2.856	2.874
Sr2/Y2-O1(×2)	2.545(4)	2.556(4)	2.568(5)	2.516(6)	2.522(4)
Sr2/Y2-O1(×2)	2.7588(34)	2.779(5)	2.791(5)	2.769(5)	2.783(4)
Sr2/Y2-O2(×4)	2.7416(5)	2.7546(7)	2.7645(7)	2.7769(7)	2.7943(6)
Sr2/Y2-O3(×2)	2.648(4)	2.670(5)	2.675(5)	2.815(7)	2.835(6)

Average	2.687	2.703	2.713	2.731	2.746
Sr3/Y3-O1(×4)	2.531(4)	2.556(6)	2.575(6)	2.656(7)	2.661(5)
Sr3/Y3-O2(×4)	2.3564(30)	2.352(4)	2.357(4)	2.345(4)	2.3570(28)
Sr3/Y3-O4(×1)	2.390(6)	2.356(9)	2.360(8)	2.377(11)	2.399(7)
Sr3/Y3-O4'(×1)	-	2.639(28)	2.712(25)	2.693(15)	2.715(8)
Average	2.438	2.463	2.480	2.507	2.519
Co1-O2(×2)	1.8323(33)	1.840(4)	1.844(5)	1.866(5)	1.879(4)
Co1-O3(×2)	1.944(4)	1.947(5)	1.955(5)	1.935(6)	1.916(6)
Co1-O4/O4'(×1)	2.218(9)/-	2.297(12)/ 1.976(14)	2.298(14)/ 1.952(13)	2.352(21)/ 2.004(11)	2.420(16)/ 2.053(8)
Average	1.954	1.943	1.945	1.956	1.965
Co2-O1(×4)	1.9177(3)	1.9256(3)	1.9323(4)	1.9418(4)	1.9527(3)
Co2-O2(×2)	2.0693(33)	2.093(4)	2.106(5)	2.118(5)	2.139(4)
Average	1.968	1.981	1.990	2.001	2.015

High temperature (HT) structures

The evolution of 2-D and 3-D intensity contour plots of ND patterns from 300 to 900 ºC is shown in Figure 2.3 (a) and (b), respectively. Figure 2.4 shows refinement profiles of ND patterns, and Table 2.1 summarizes the detailed structural parameters as a function of temperature. Overall, the structural symmetry remained unchanged (S.G. I4/mmm) throughout the temperature range (RT-900 ºC) studied. The refinement of O4-site occupancy gives values higher than *ca.* 0.35 for all the ND patterns. As mentioned earlier, the short interatomic distance between adjacent O4 only allows an O4-occupancy ≤ 0.25. The higher occupancies at higher temperatures might imply additional nuclear density distribution near the O4-site. To test this hypothesis, we split the O4-site into two positions O4 (~0.375, 0.5, 0) and O4' (~0.25, 0.5, 0) and obtained improved reliability factors (*i.e.* 3.08 *vs* 3.28 for R_{wp}% at 700 ºC), see Table 2.1. Figure 2.5 of Fourier observed nuclear density map further shows that the nuclear densities around O4-site spread over a larger

area toward the unit cell edges along *a* or *b* axis as temperature increases. The temperature-induced shift in nuclear density of O4 with respect to the original position at RT suggests that Co1 prefers a coordination environment with oxygen closer to octahedra $Co1O_6$. Furthermore, the progressive spread-out of O4 (or O4') nuclear density with temperature shown in Figure 2.5 also signals an increased oxygen mobility, which may play an important role in oxygen-ion conduction.

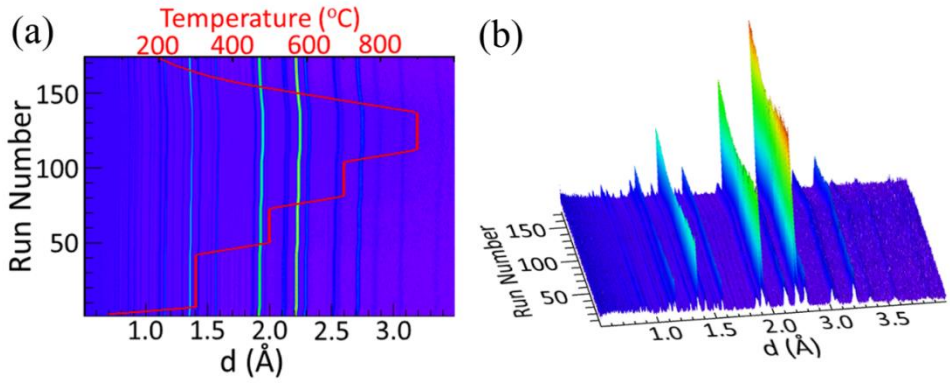

Figure 2.3 The 2D (a) and 3D (b) intensity contour plots of ND during heating and cooling.

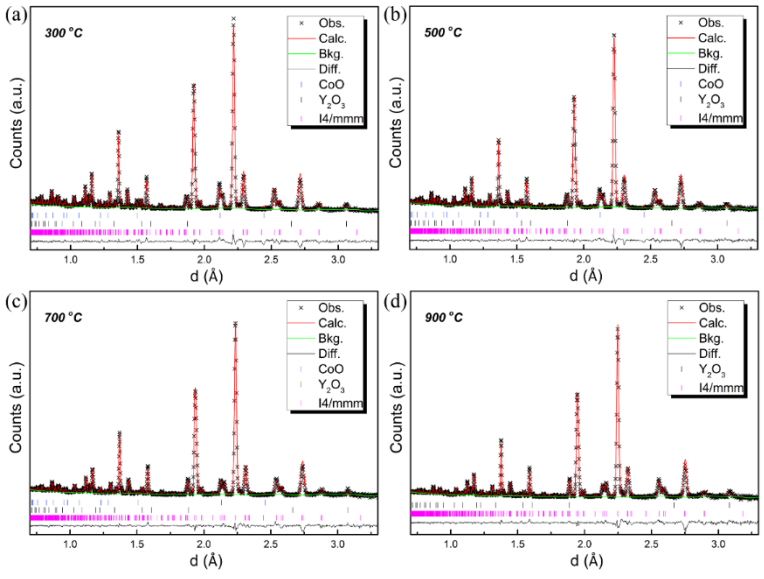

Figure 2.4 Rietveld refinement profiles of ND data at (a) 300, (b) 500, (c) 700 and (d) 900 °C.

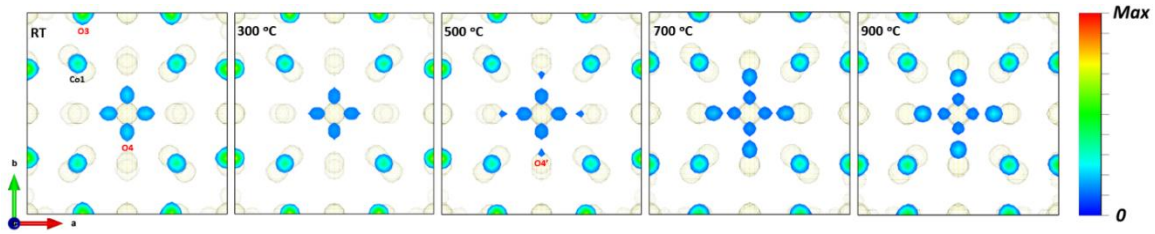

Figure 2.5 Fourier observed nuclear density map for (001) plane at an iso-surface level of 5% maximum.

As listed in Table 2.2 and plotted in Figure 2.6, all the Co-O bond lengths increase with temperature except for Co1-O3, where a decrease is observed above 500 ºC. A possible reason for the decrease is the progressive "migration" of O4 (O4') toward cell edges, which alters the positions of the neighboring Co1 or O3 and thus shortening the Co1-O3 bond length. Those two Co2-O2 bonds are shorter than the four Co2-O1 bonds in *ab* plane of $Co2O_6$ octahedra. This tetragonal distortion is likely the result of an intermediate-spin (IS) state of Co^{3+} at Co2-site induced by a strong repulsion between Co-d_{z^2} electron and O-2p electron.[81, 87, 97]

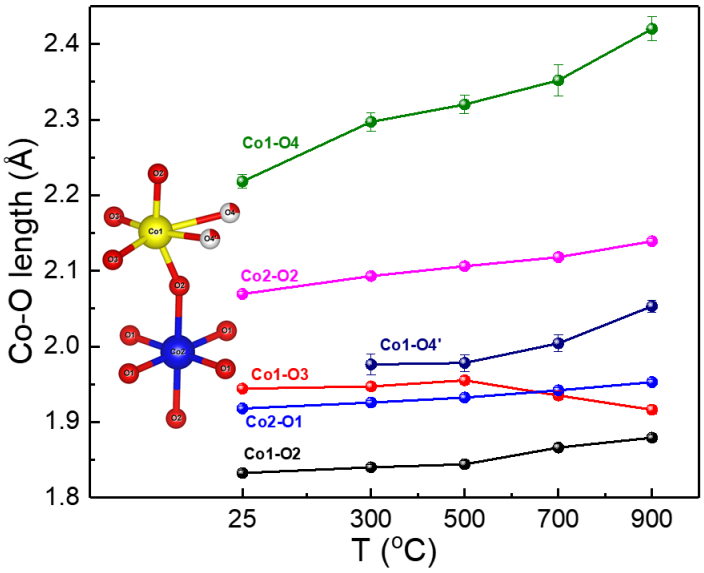

Figure 2.6 Evolution of the Co-O bond lengths with temperature.

Oxygen vacancies ($V_o^{\cdot\cdot}$) distribution and transport pathway

To understand the distribution of oxygen vacancies over O-site and their transport pathways, we plot oxygen occupancy as a function of temperature and create a structural view along *b*-axis of Co-O layer in Figure 2.7. As is seen from Figure 2.7 (a), the O-sites at Co2-ion, *i.e.* O1 and O2, are almost fully occupied from RT to 900 ºC. This suggests the $V_o^{\cdot\cdot}$ transport along *c*-axis is completely blocked since no charge carriers are available in the entire O1-Co2-O1-plane, see Figure 2.7 (b). Most of $V_o^{\cdot\cdot}$ populates on Co1-polyhedra containing O4/O4′- and O3-site. Such a $V_o^{\cdot\cdot}$-distribution pattern infers a likely 2D diffusion pathway for oxygen between O3 and O4/ O4′ in the *ab* plane, which is consistent with the findings in $Sr_{0.7}Ho_{0.3}CoO_{3-\delta}$[82] and $Sr_{0.8}Y_{0.2}CoO_{3-\delta}$ [98]. The delocalization of O4 to O4′ facilitates $V_o^{\cdot\cdot}$-transport in this 2D pathway as the O3-O4′ distance is shorter than O3-O4 (3.15 Å *vs* 3.81 Å at 700 ºC, for example). On the contrary, a molecular dynamics (MD) study on $Sr_{0.75}Y_{0.25}CoO_{3-\delta}$, using a structure model, in which O1, O2, O3 are fixed at a fully occupied state and O4′ is ignored, shows that the exchange between O3 and O4 is very limited even at high temperatures.[99] Instead, the MD model suggests that O2 is increasingly distorted along [111] direction towards the neighboring O4-site with increasing temperatures and substantial exchange between O2 and O4 may take place. Figure 2.8 indeed shows an increasing deviation from the ideal 180º of Co1-O2-Co2 angle with temperature, which brings O2 closer to O4 with a shortened bond length between O2 and O4, *e.g.* O3-O4 (3.81 Å) > O3- O4′ (3.15 Å) > O2-O3 (2.90 Å) > O3-O3 (2.71 Å) > O2-O4 (2.64 Å) > O2-O4′ (2.44 Å) at 700 ºC. However, since O2-site is slightly oxygen deficient as shown in Figure 2.7 (a), the second possible $V_o^{\cdot\cdot}$ transport pathway in the *ab*

plane is O2-O4/O4′-O2. The delocalization of O4 to O4′ also supports this $V_o^{\cdot\cdot}$ migration pathway.

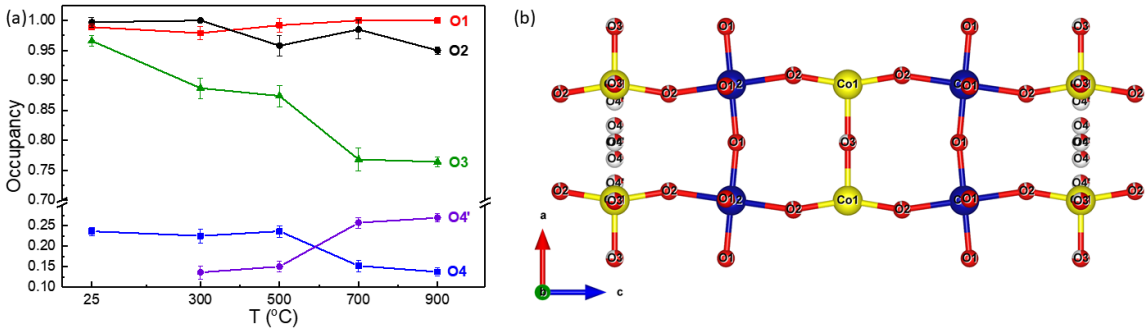

Figure 2.7 (a) Occupancies of various oxygen-sites; (b) unit cell containing only Co-ions and oxygen-ions along the *b*-axis.

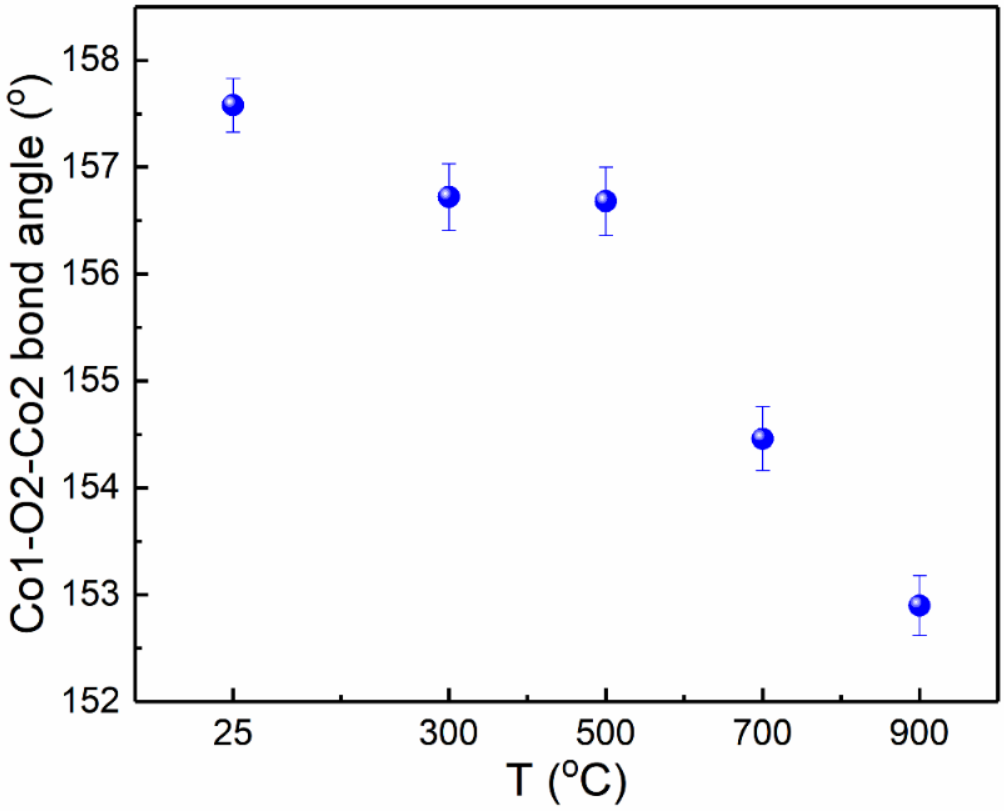

Figure 2.8 Bond angle of Co1-O2-Co2 *vs* temperature. The kink of Co1-O2-Co2 angle at 500 °C is probably caused by the same reason with the decrease of Co1-O3 bond lengths above 500 °C shown in Figure 2.6 as the O4-delocalization affects the position of neighboring Co1.

Oxygen stoichiometry and Co-ion oxidation states

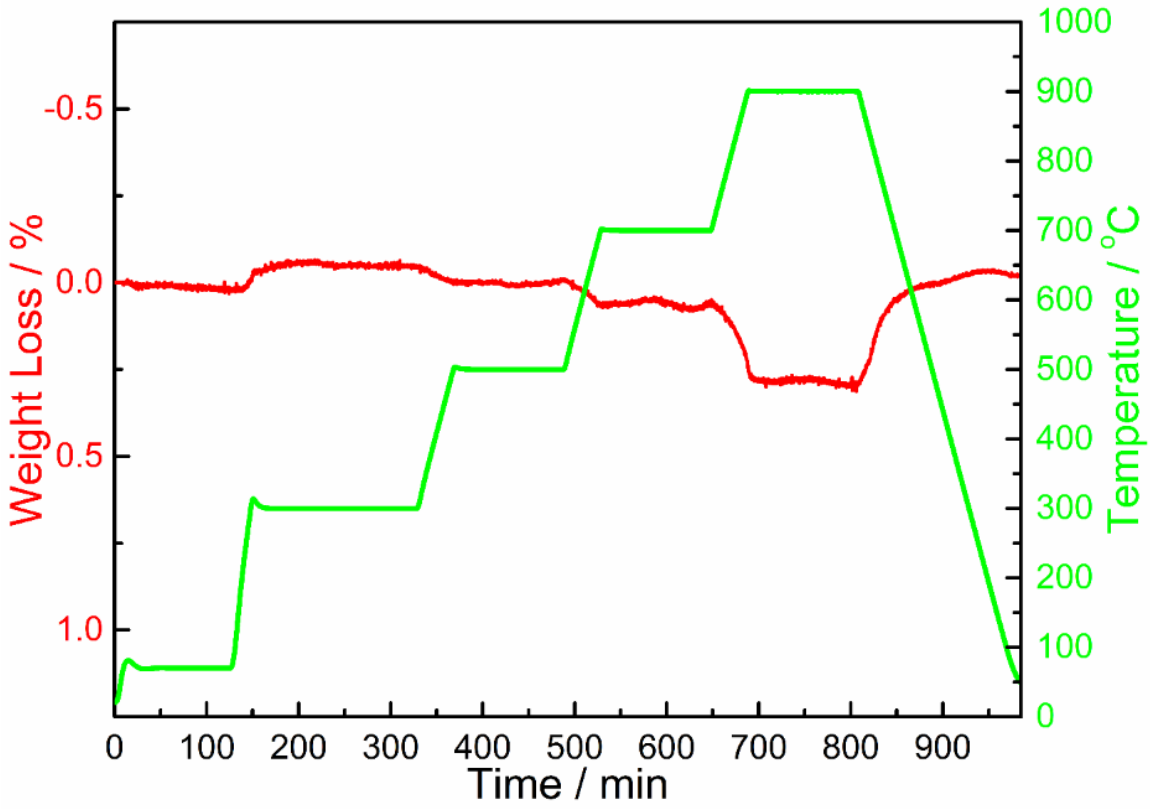

Figure 2.9 TGA curves under air following the same temperature regime with ND.

The original TGA curve of SYC30 is shown in Figure 2.9. The (3-δ) values and oxidation states of Co-ions obtained from both TGA and ND refinement are shown in Figure 2.10 as a function of temperature. The actual values of (3-δ) and Co-ion oxidation states at different temperatures are listed in Table 2.3 for both SYC30 and SYC10 for comparison purpose. There are a few trends observed: 1) A slow oxygen uptake is observed from RT to ca. 300 ºC, consistent with the previous results on Nb-doped SCO.[58, 97] The (3-δ) decreases at higher temperature due to the break of metal-oxygen bonds and the release of oxygen gas into the surrounding atmosphere. 2) (3-δ) determined by TGA is consistent with the reported values of 2.62 [80] or 2.63 [81], and systematically higher than those from

ND, which has also been observed in other studies [100-101]; 3) SYC30 has a higher (3-δ), meaning less oxygen vacancies than SYC10, while the average Co-ion oxidation state of SYC10 is higher at <700 ºC, but becoming very close to those of SYC30 at >700 ºC.

To understand the above trending, the bond valence sums (BVS) were calculated to evaluate the valence state of Co-ions in their local coordination environment and the results are listed in Table 2.4 for both SYC30 and SYC10 for comparison purpose. Due to the positional proximity of O4 in SYC30, we consider the Co-O coordination at RT in either tetrahedra $Co1O_4$ with two O2 and two O3, or pentahedron $Co1O_5$ with two O2, two O3, one O4. At higher temperatures, Co1 is more likely to coordinate in $Co1O_5$ with half O4, half O4′, two O2 and two O3 because of their closer physical proximity and low occupancies. These BVS results confirm that $Co^{2+/3+}$ has a preference at both Co1- and Co2-site. As for SYC10, a mixed oxidation state of $Co^{2+/3+}$ on the Co1-site and $Co^{3+/4+}$ on the Co2-site is apparent as indicated by their BVS values.

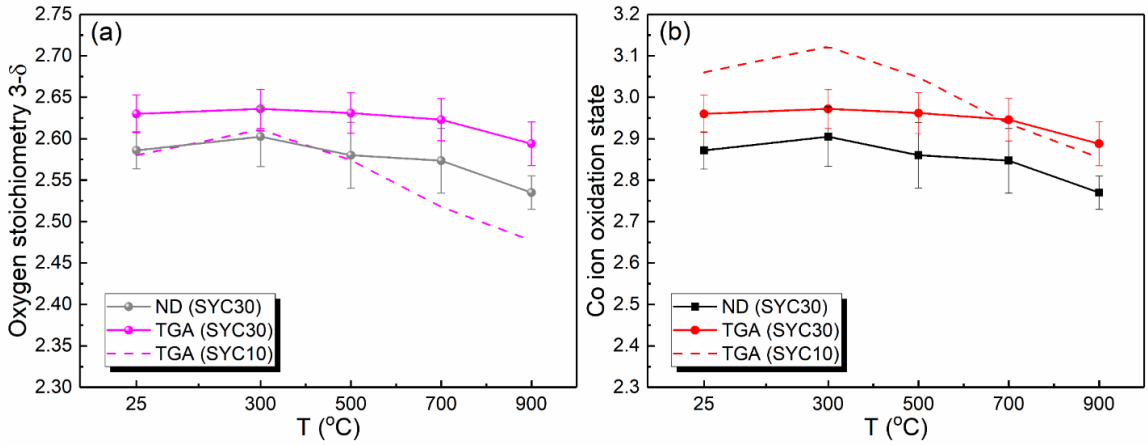

Figure 2.10 (a) Oxygen stoichiometry and (b) Co-ion oxidation states determined from both ND and TGA. The initial RT value is taken from iodine titration for TGA-oxygen stoichiometry curve. The dashed lines in (a) and (b) are taken from ref.[87]

Table 2.3 Co-ion oxidation-state and oxygen stoichiometry (in parenthesis) at different temperatures. Values for SYC10 are taken from ref.[87].

T (ºC)	TGA		*ND*	
	SYC30	SYC10	SYC30	SYC10
RT	+2.96 (2.63)	+3.06 (2.58)	+2.88 (2.59)	+2.98 (2.54)
300	+2.98 (2.64)	+3.12 (2.61)	+2.90 (2.60)	+3.08 (2.59)
500	+2.96 (2.63)	+3.04 (2.57)	+2.86 (2.58)	+3.00 (2.55)
700	+2.94 (2.62)	+2.94 (2.52)	+2.84 (2.57)	+2.82 (2.46)
900	+2.88 (2.59)	+2.86 (2.48)	+2.78 (2.54)	+2.62 (2.36)

Table 2.4 Bond valence sums of Co-ions.

Ions		RT	300 ºC	500 ºC	700 ºC	900 ºC
Co1	SYC30	2.50 ($Co1O_4$) 2.75($Co1O_5$)	2.80	2.79	2.71	2.68
	SYC10	3.00	2.91	2.87	2.76	2.71
Co2	SYC30	3.04	2.94	2.88	2.80	2.70
	SYC10	3.82	3.75	3.62	3.57	3.37

Thermal expansion

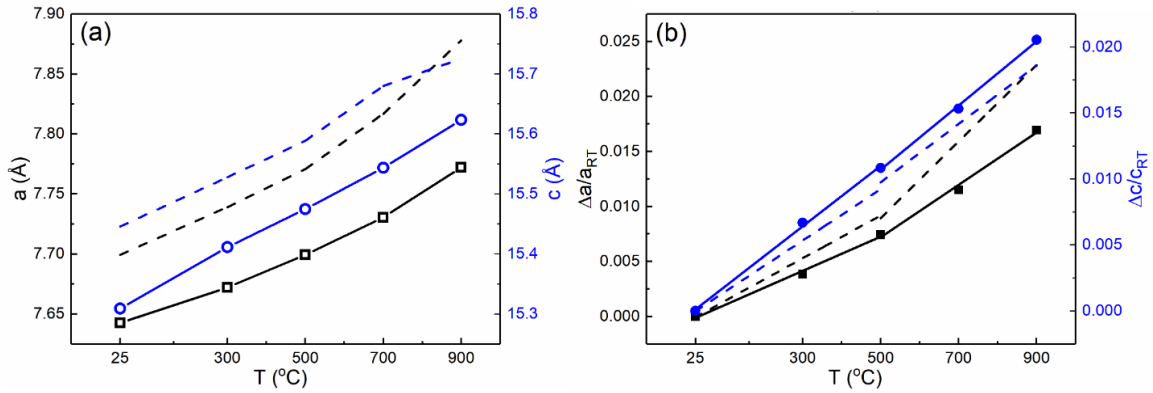

Figure 2.11 (a) Lattice parameters and (b) linear thermal expansion fitting vs temperature. The dash lines correspond to SYC10 taken from ref.[87]

The lattice parameters of SYC30 and SYC10 vs temperature are shown in Figure 2.11 (a), where the former is expectedly smaller than the latter due to smaller Y^{3+} radius than Sr^{2+}. The thermal expansion along the *c*-axis of SYC30 and SYC10 shown in Figure 2.11 (b) is almost linear, while that along *a*-axis is nonlinear with a greater expansion at higher temperatures when additional oxygen loss leads to additional chemical expansion. The linear thermal expansion coefficients (α) for SCY30 along *a*- and *c*-axis are 15.5 and 22.9×10^{-6} K^{-1} (RT to 500 °C) and 23.8 and 24.3×10^{-6} K^{-1} (500 to 900 °C), respectively. The average α from 500 to 900 °C calculated by $\frac{2\alpha_a+\alpha_c}{3}$ is 24.0×10^{-6} K^{-1}; these values are lower than that of $Sr_{0.9}Y_{0.1}CoO_{3-\delta}$ (30.6×10^{-6} K^{-1} in 500-900 °C)[87] shown in Figure 2.11 (b) and other doped $SrCoO_{3-\delta}$, such as $SrCo_{0.9}Nb_{0.1}O_{3-\delta}$ (31.2×10^{-6} K^{-1} in 500-900 °C)[97].

- 2.3.2 Structure vs ORR activity

For mixed ionic and electronic conductors (MIECs) like SYC-series, the ORR activity is determined by the rate of surface oxygen exchange and bulk diffusion, both of which are closely related to the concentration and mobility of oxygen vacancies, the mobile defect in SYC-based MIECs.[102, 33-35, 40] The theoretical first-principles calculations show that the energy gap between O-2p center and Fermi energy is a key descriptor for ORR activity of a perovskite oxide.[48-50] When an oxygen vacancy moves to its adjacent position, the O-2p center at the original position is decreased with respect to the metal-3d band, accompanied by an increase in Fermi energy. The motional enthalpy for such a migration is related to the number of electrons interchanged between the Fermi level and O-2p band level. Crystal structure is the decisive factor for the above energetics. Below we focus on comparing the

structural difference between SYC10 and SYC30 and its implications on the oxide-ion transport.

Structural differences between SYC10 and SYC30

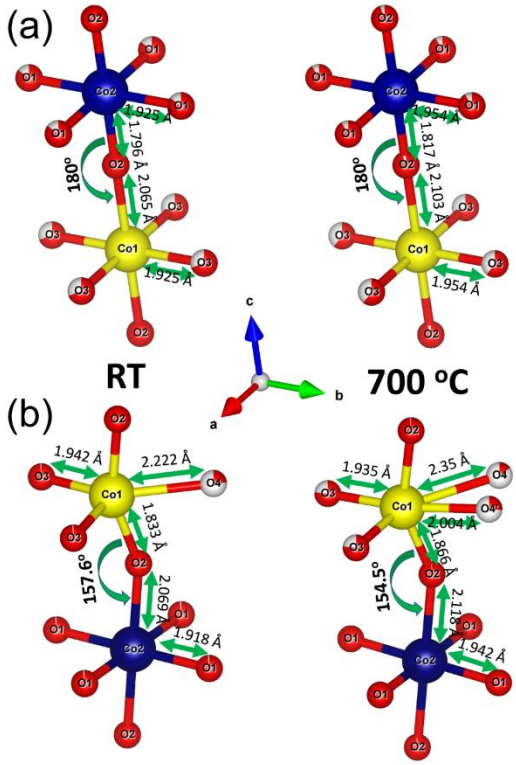

Figure 2.12 Co1- and Co2-polyhedrons in the unit cell of (a) SYC10 and (b) SYC30 (viewed from an arbitrary direction).

As indicated in Figure 2.1, both SYC10 and SYC30 have corner-sharing polyhedra in an arrangement such that oxygen-saturated Co2-polyhedra and oxygen-deficient Co1-polyhedra are alternatively stacked along [001] direction. However, the polyhedra in SYC10 does not tilt, while those in SYC30 are tilted around *a*- and *b*-axis ($a^+a^+c^0$), as shown in Figure 2.12.

Another major structural difference is the oxygen distribution in the oxygen-deficient layer [Co1 layer, (001) plane]. Figure 2.13 (a) shows that oxygens are

symmetrically distributed around Co1 in SYC10, whereas Figure 2.13 (b) shows asymmetrically distributed oxygen atoms around Co1 in SYC30 as indicated by the large deviation from 90° of O3-Co1-O3 angle and O4 being closer to a central area. At a higher temperature, for example 700°C, the oxygen arrangement in SYC30 becomes close to that of SYC10, since more nuclear densities gradually shift from O4 to O4′ while the O3-Co1-O3 angle is decreased to near 90° by thermally activated atomic movements.

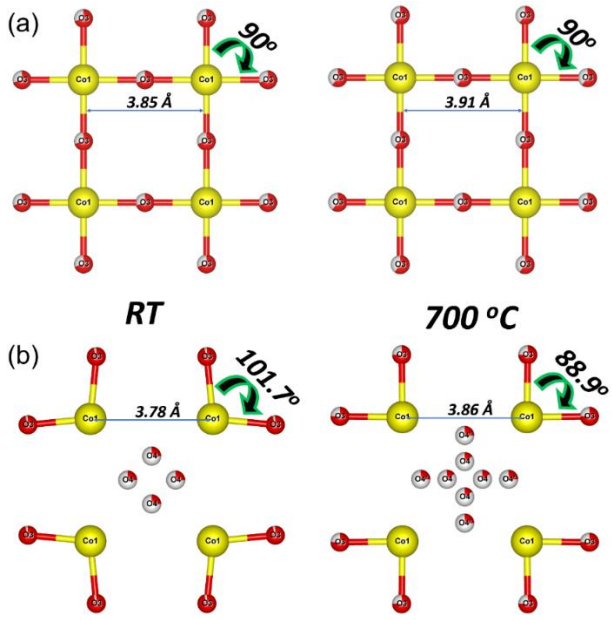

Figure 2.13 (a) oxygen-deficient layer of SYC10 and (b) oxygen-deficient layer of SYC30 at RT and 700 °C viewed along *c*-axis.

As aforementioned, $V_o^{\cdot\cdot}$ are mostly populated around Co1, which is coordinated with O3 in SYC10 but with O3, O4, O4′ in SYC30. It is evident that the more symmetrically arranged O3 would provide SYC10 with a much easier $V_o^{\cdot\cdot}$ migration pathway in Co1-(001) plane. In contrast, $V_o^{\cdot\cdot}$ transport along *c*-axis in SYC30 is fully blocked because O1-site in the neighboring Co2-(001) plane is fully occupied even at 900 °C, which is compared to oxygen occupancy of 0.9 from RT to 900 °C in SYC10.[87] The

presence of $V_o^{\cdot\cdot}$ at O1-site in SYC10 allows for oxide-ion conduction not only in Co1-(001) plane, but also in the direction along *c*-axis through a path of O3-O2-O1-O3. On the other hand, more $V_o^{\cdot\cdot}$ are present in SYC10 than SYC30 according to TGA and ND data. Hence, a higher oxide-ion conduction in SYC10 than SYC30 is expected.

Energy for oxygen migration

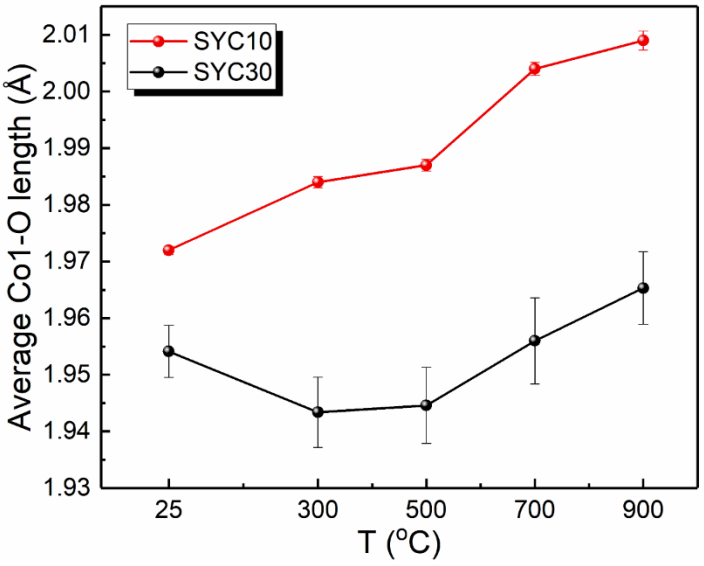

Figure 2.14 Average Co1-O blond length in SYC10[87] and SYC30.

The above structural analysis reveals that oxygen-migration in SYC10 and SYC30 mainly occurs within Co1-polyhedra. The similar BVS values of Co1-ions in Table 2.4 between SYC10 and SYC30 suggest that their oxidation states are close to 2+/3+. On the other hand, Figure 2.14 shows that the average Co1-O bond length in SYC30 is smaller than that of SYC10, suggesting a stronger interaction between Co-3d and O-2p orbitals in SYC30.

With the knowledge of Co1 oxidation state and Co1-O bond length, a qualitative molecular orbital energy diagram (without considering octahedral distortions for simplicity) of Co1O6 in SYC10 and Co1O5 in SYC30 is illustrated in Figure 2.15. The $Co1O_5$ in

SYC30 is viewed as octahedra with one missing ligand on the top. The possible spin-states of Co^{3+} are high-spin ($t_{2g}^4 e_g^2$) or intermediate-spin ($t_{2g}^5 e_g^1$).[81] Co^{2+} is known to be very stable in its high-spin state ($t_{2g}^5 e_g^2$), which is also used in Figure 2.15.[81, 103-104] The energy changes for forming σ and π bonds are greater for SYC30 because of the stronger interactions, resulting in a higher Fermi Level relative to O-2p band center than that of SYC10. Hence, the oxygen migration energies are expected to be higher for SYC30, which implies that the energy barrier for oxygen migration is higher in SYC30 than in SYC10.

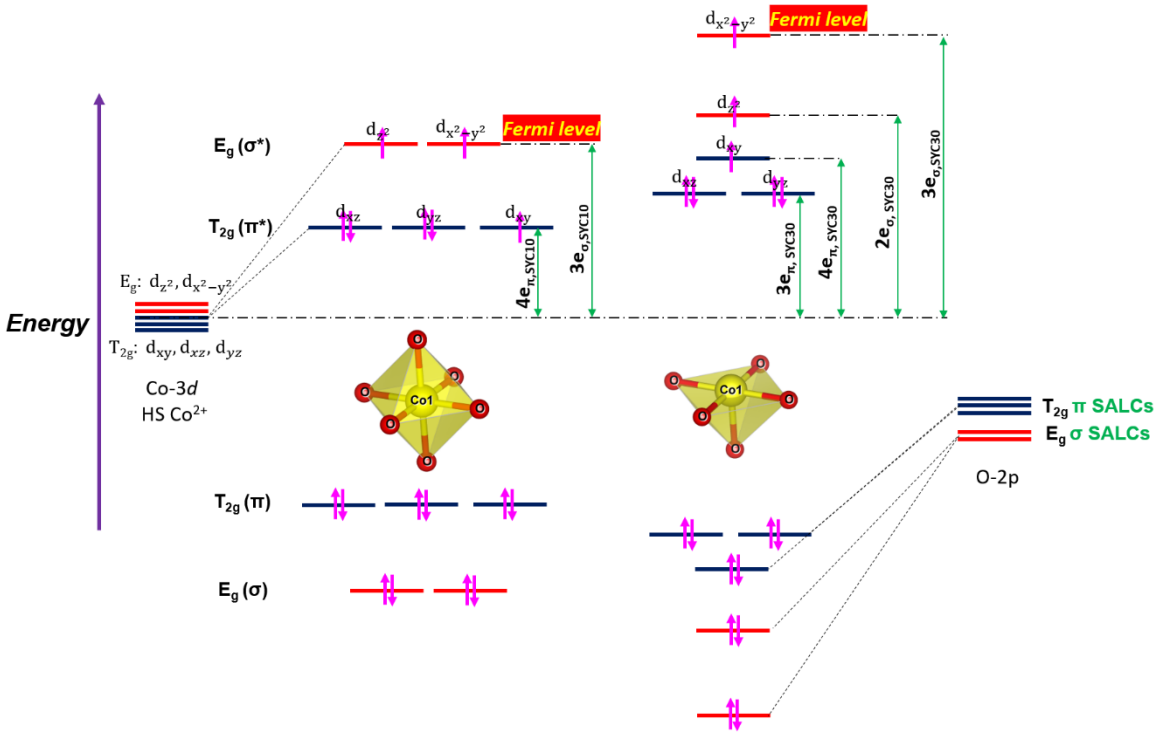

Figure 2.15 Molecular orbital energy diagram for polyhedra in SYC10 and SYC30. e_σ and e_π are the orbital energy changes at maximum overlap for σ and π bonds, respectively.

- 2.3.3 Secondary phase issue

The refinement of ND patterns suggests Y_2O_3 and CoO as two possible second phases in SYC30. The space group of Y_2O_3 is Fm-3m,[105] while it is C2/m and Fm-3m below and

above 305K, respectively, for CoO.[106] Table 2.5 lists the compositions of these phases obtained from Rietveld refinement of ND data, with the detailed structural parameters for Y_2O_3 and CoO listed in Table 2.6. The refined composition of SYC30 is temperature-dependent, but very close to the nominal one, e.g. $Sr_{0.7}Y_{0.27}Co_{0.94}O_{3-\delta}$ (500 ºC), $Sr_{0.7}Y_{0.28}Co_{0.98}O_{3-\delta}$ (700 ºC), and $Sr_{0.7}Y_{0.28}CoO_{3-\delta}$ (900 ºC). The deficiencies in Y and Co indicate Y_2O_3 and CoO precipitating out as a second phase. The less deficiency at higher temperatures suggests that the solubility of Y_2O_3 and CoO in SYC30 becomes higher at higher temperatures. It is interesting to note that the amount of CoO peaks at 300 ºC coincides with the maximum oxygen content observed from the TGA curve shown in Figure 2.9. It seems that the oxygen content in SYC30 is closely related to the precipitation-dissolution of CoO as temperature changes. In addition, Figure 2.16 (a) suggests that the precipitation-dissolution process of CoO is reversible since the CoO (220) peak at 300 ºC is reproducible during the heating and cooling cycle. The precipitation of Y_2O_3 and CoO from SYC30 has also been observed by SEM (BSE mode), as shown in Figure 2.16 (b). The EDS analysis indicates that the bright and dark phases are Y_2O_3 and CoO, respectively.

Table 2.5 Phase compositions (wt. %) from RT to 900 ºC.

Phase	RT	300 ºC	500 ºC	700 ºC	900 ºC
SYC30	95.5	94.2	95.9	98.1	98.7
Y_2O_3	1.8	1.7	1.6	1.3	1.3
CoO	2.7	4.1	2.5	0.6	0

Table 2.6 Structural parameters from Rietveld refinement of ND patterns for Y_2O_3 and CoO.

Parameters	RT	300 ºC	500 ºC	700 ºC	900 ºC
		Y_2O_3			

space group	Fm-3m				
a (Å)	5.2914(7)	5.303(1)	5.316(1)	5.330(1)	5.340(1)
atomic position	Y 4a (0, 0, 0) O 8c (1/4, 1/4, 1/4), three-quarter occupied				
	CoO				
space group	C2/m	Fm-3m			-
Lattice constant (Å or °)	a: 5.198(6) b: 3.015(3) c: 3.017(3) β: 125.30(7)	4.231(1)	4.242(1)	4.255(1)	-
atomic position	Co 2a (0, 0, 0) O 2d (0, 1/2, 1/2)	Co 4a (0, 0, 0) O 4b (0, 1/2, 1/2)			-

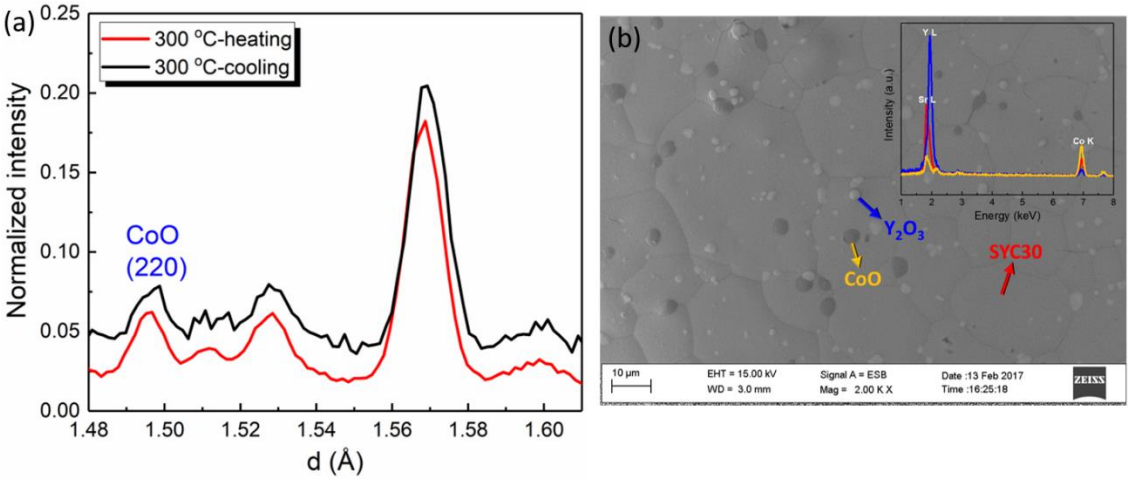

Figure 2.16 (a) The ND patterns over a selected range of *d*-spacing at 300 °C during a heating and cooling cycle; (b) BSE image of SYC30. The insert shows the EDAX spectra of three areas of interest.

- 2.3.4 Electrochemical performance

To establish the structure-activity relationships, electrochemical measurements were carried out to evaluate the ORR activity of SYC30 and compared with SYC10.

Determination of rate limiting steps for ORR

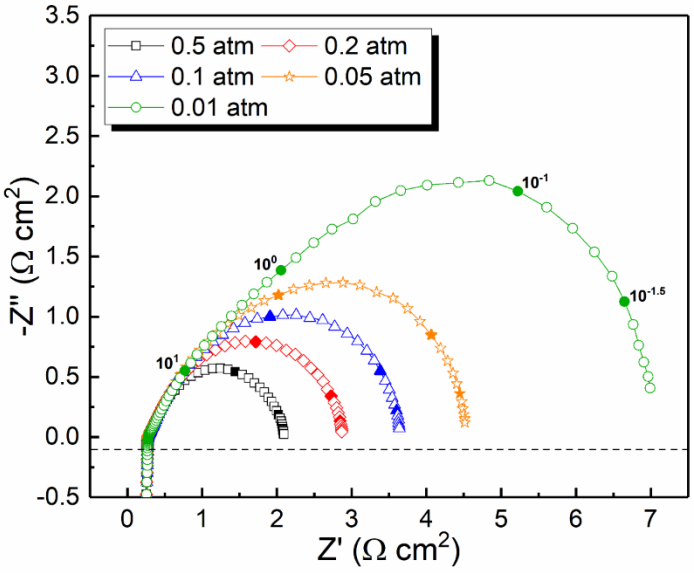

Figure 2.17 Nyquist plots of symmetrical cell from 0.01 to 0.5 atm at 650 ºC.

The P_{O_2} dependence of the area-specific polarization resistance (R_p) of SYC30 was measured from 600 to 800 ºC, aiming to understand the oxygen reduction kinetics. R_p typically follows the power law with P_{O_2} for an oxygen reduction reaction (ORR)[107]:

$$R_p \in (P_{O_2})^{-m} \tag{2-4}$$

The value of m indicates the rate-limiting step:

(1) m=1, $O_2(g) \rightarrow O_{2,ads}$, oxygen molecule adsorbs on the cathode surface.

(2) m=0.5, $O_{2,ads} \rightarrow 2O_{ads}$, adsorbed oxygen species dissociates into oxygen atoms.

(3) m=0.25, $O_{ads} + 2e' + V_o^{\cdot\cdot} \rightarrow O_o^{\times}$, oxygen atoms are reduced by electrons and vacancies to become lattice oxygen, which is also known as charge-transfer process.

(4) m=0, $O_{electrode}^{2-} \rightarrow O_{electrolyte}^{2-}$, oxygen-ion migrates from cathode into electrolyte.

The typical Nyquist plots obtained under different P_{O_2} at 650 ºC are shown in Figure 2.17. The plots consist of a high-frequency semicircle ($R_{p,high}$) and a low-frequency

semicircle ($R_{p,\ low}$), except for >700 °C where no $R_{P,\ low}$ can be observed. A plot of log R_p *vs* log Po_2 is shown in Figure 2.18 (a), where the m values for $R_{p,\ low}$ from 600 to 700 °C are close to 0.5, suggesting oxygen dissociation as the rate-limiting step (Step-2). For $R_{p,\ high,}$ the m values are close to 0.25 from 600 to 800 °C, suggesting charge-transfer process (Step-3) is rate-limiting. A comparison of $R_{p,\ high}$ and $R_{p,\ low}$ in Figure 2.18 (b) indicates that R_P of SYC30 is dominated by $R_{p,\ high}$, which suggests that the ORR kinetics is rate-limited by the charge-transfer process. For SYC10, a different kinetics was observed, in which the ORR kinetics is primarily limited by charge-transfer process at 600-650 °C and oxide-ion migration from cathode to electrolyte at 700-800 °C.[87] The total R_p at 0.2 atm is also compared in Figure 2.18 (b). SYC10 shows a much lower R_p than SYC30, but both are lower than other popular cathodes, such as BSCF[108], SCN10[58]. This experimental observation supports the ORR-activity prediction discussed in Section 3.2 based on structural and transport-pathway analysis.

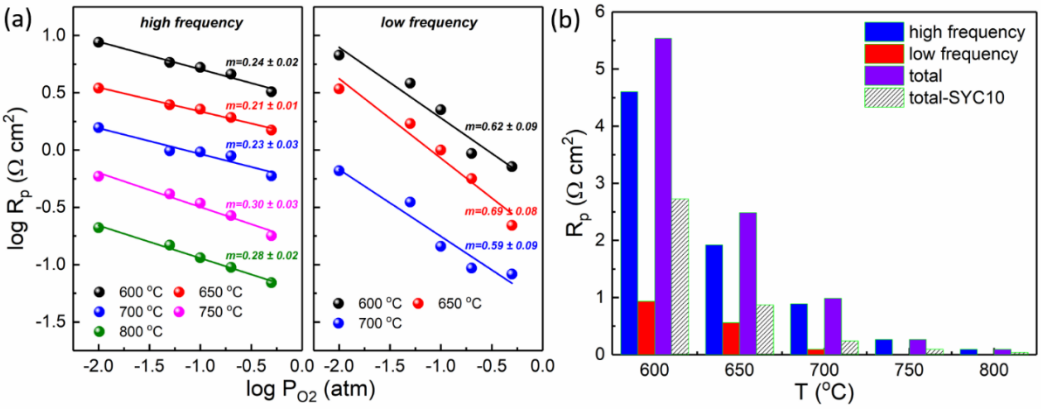

Figure 2.18 (a) P_{O_2}-dependence of polarization resistance; (b) polarization resistance at P_{O_2}=0.2 atm.

Fuel cell performance

The fuel cell performance with SYC30 as the cathode was evaluated in an anode-supported single cell Ni-GDC/GDC/SYC30. Figure 2.19 shows the current-voltage and -power

characteristics at 600 ºC and 700 ºC. The open circuit voltages are 0.84 (600 ºC) and 0.76 V (700 ºC), respectively, typical for ceria-based cells.[109] The cell exhibits a maximum power density of 0.914 and 0.314 W cm^{-2} at 700 and 600 ºC, respectively. On the other hand, the same single cell configuration with SYC10 cathode shows a much better performance with a peak power density of 1.495 and 0.408 W cm^{-2} at 700 and 600 ºC, respectively. Again, this experimental result supports the ORR-activity prediction discussed in Section 2.3.2 based on structural and transport analysis.

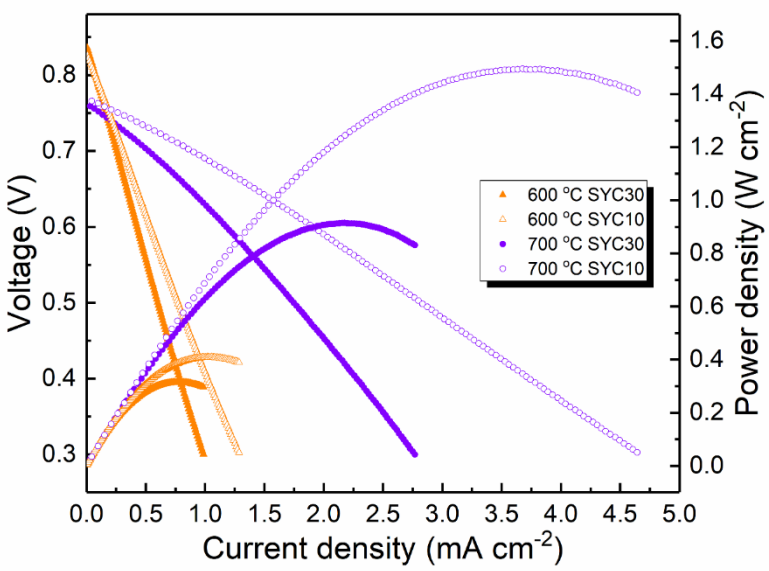

Figure 2.19 Voltage and power density dependence on current density of anode-supported single cell with SYC30 or SYC10 as cathode at 600 ºC and 700 ºC.

2.4 Conclusion

The crystal structure of $Sr_{0.7}Y_{0.3}CoO_{3-\delta}$ (SYC30) determined by *in-situ* neutron diffraction contains alternate, tilted polyhedra of oxygen-deficient Co1-layer and oxygen-saturated Co2-layer in a new ordered perovskite lattice with a large unit cell (2a×2a×4a) and I4/mmm

space group. It is revealed that Co^{2+} and Co^{3+} prefer occupying Co1-site and Co2-site, respectively; $V_O^{\cdot\cdot}$ is mostly populated within Co1-polyhedra coordinating with O4/O4′, O3, and O2. In contrast, Co2-polyhedra (octahedra) contain fully occupied O1 and O2 from RT to 900 ºC. The way how $V_O^{\cdot\cdot}$ is distributed in SYC30 infers a 2D diffusion pathway in *ab* plane around Co1. Fourier observed nuclear density map further suggests that the nuclear density of O4-site expands with temperature in the *ab* plane; such a gradual delocalization of O4 implies an increased oxygen mobility. In comparison, SYC10 has a more symmetrical structure and $V_O^{\cdot\cdot}$ distribution, and higher $V_O^{\cdot\cdot}$ concentration. Molecular orbital energy analysis indicates SYC30 has a higher Fermi level relative to O-2p energy level in the active Co1-polyhedra, and thus a higher motional enthalpy for $V_O^{\cdot\cdot}$ migration. The electrochemical measurements indeed confirm that SYC30 has a higher polarization resistance and worse SOFC performance than SYC10. Overall, this study illustrates how the structural parameters affect the activity of a mixed oxide-ion and electron conductors in electrochemical cells.

CHAPTER 3

Nb-DOPED $SrCoO_{3-\delta}$ AS CATHODE FOR SOLID OXIDE FUEL CELLS

3.1 Introduction

Nb_2O_5 is the most studied dopant for the SCO system (collectively denoted as SCN) to stabilize the ORR-active cubic structure for IT-SOFCs and oxygen separation membranes applications.[58, 110-118] Our previous work indicates that $SrCo_{0.9}Nb_{0.1}O_{3-\delta}$ (denoted as SCN10 hereinafter) has a good thermal stability below 700 ^oC and ~8× lower polarization resistance than the state-of-the-art cathode $(La_{0.60}Sr_{0.40})_{0.95}(Co_{0.20}Fe_{0.80})O_{3-\delta}$ (LSCF) at 600 ^oC, 0.75 Ω cm^2 *vs* 6.00 Ω cm^2.[58] The maximum power density with SCN10 as a cathode on 20-μm thick Sm-doped CeO_2 (SDC) electrolyte supported on a SDC-Ni anode can reach 1,008 mW cm^{-2} at 600 ^oC,[113] indicating the intrinsically high activity of SCN10 for ORR.

Despite the promising results, a thorough understanding of the structure-stoichiometry relationship and transport properties in the SCN system, particularly at elevated temperatures, is still lacking. Yoo, *et al*. studied the crystal structure of SCN10 with room-temperature (RT) Neutron Diffraction (ND) and high-temperature X-ray diffraction (HTXRD);[69] the latter HTXRD revealed that the crystal symmetry transforms from tetragonal (P4/mmm) to 3C-cubic (Pm-3m) at 160 ^oC. Other powder RTXRD studies have also reported similar symmetries in SCN10 *viz.* 3C-cubic (Pm-3m)[68,114,115-116] and

tetragonal (P4/mmm)[58, 69]. However, XRD cannot provide accurate information on the oxygen positions/occupancies because the scattering contribution of oxygen to the total Bragg scattering is much weaker than that of cations. On the other hand, the neutron scattering length (b) of oxygen (b_O=5.803 fm) is comparable to those of cations (b_{Sr}=7.020 fm, b_{Co}=2.490 fm, and b_{Nb}=7.054 fm),[96] making neutron diffraction advantageous in determining oxygen positions, occupancies, coordination and polyhedral distortion. The previously reported ND studies of SCO-based materials were all conducted at RT,[112] which provides limited structural information for high-temperature applications of this class of materials.

Following our previous work on the electrochemical characterization of SCN materials showing excellent ORR/OER performance,[58] in this chapter a systematic study of structure-stoichiometry-temperature relationship using *in-situ* neutron diffraction (ND) combined with thermogravimetric analysis (TGA) is reported. No single cell performance was reported here due to the specific focus of this study on structural evolution with temperature and the fact that large amount of cell performance data using SCN as a cathode are available in the literature.[110, 112-113, 116-117]

3.2 Experimental

- 3.2.1 Sample synthesis

$SrCo_{0.9}Nb_{0.1}O_{3-\delta}$ (denoted as SCN10) was prepared by traditional solid-state reactions. Briefly, stoichiometry amounts of $SrCO_3$ (≥99.9%, Aldrich), Co_3O_4 (99.7%, Alfa Aesar) and Nb_2O_5 (99.9%, Alfa Aesar) were mixed by ball-milling in ethanol for 3 h, dried and pressed into pellets, followed by calcination at 1000 ^oC for 12 h with 3 $^oC\ min^{-1}$ heating

and cooling rates. The pellets were then broken up and ball-milled and calcined again at 1050 ^{o}C for another 12 h. The final pellet was buried in the powders and sintered at 1230 ^{o}C for 10 h to ensure phase purity and homogeneity.

- 3.2.2 X-ray powder diffraction

The phases were first examined at RT using a powder X-ray diffractometer (Rigaku MiniFlex II) with graphite-monochromatized Cu-Kα radiation (λ=1.5418 Å) over a 2θ range of 20–80^{o} in a step size of 5^{o} min^{-1}.

- 3.2.3 *In-situ* neutron diffraction

In-situ neutron diffraction (ND) experiments were conducted on VULCAN, the time-of-flight Engineering Diffractometer at the Spallation Neutron Source in Oak Ridge National Laboratory.[90, 119] Pellet samples (~17 mm in diameter and ~10 mm thick) were used for obtaining strong diffraction intensities. A 5×10×5 mm^3 beam gauge volume was determined by the incident slits and receiving collimators. The ND data were collected continuously during both heating and cooling between RT and 900 ^{o}C with the samples being contained in an MgO crucible inside an air-ambient furnace. The heating rate was 10 ^{o}C min^{-1} below 300 ^{o}C and 5 ^{o}C min^{-1} between 300 and 900 ^{o}C, while the cooling rate was 10 ^{o}C min^{-1}. During heating, the samples were first held at 300 ^{o}C for 3 h, followed by annealing for 2 h at each of the three elevated temperatures, *i.e.*, 500, 700 and 900 ^{o}C. Only the last 1-h data, collected with a total neutron counts of 4×10^6 at each isothermal holding stage, were used for Rietveld refinement, which was implemented in the GSAS program using the EXPGUI interface.[93, 120] Typically, a refinement started with trial and error using the model-free Le Bail method.[94] The background was modeled with shifted Chebyshev polynomial function (type 1 in EXPGUI) with 6 terms. Gaussian width parameters (σ_1, σ_2)

and Lorentzian width parameter (γ_1) were refined for peak profiles using the Pseudo-Voigt function with Finger-Cox-Jephcoat asymmetry correction (type 3). The DIFA (one of the three parameters defining relationship between measured time-of-flight and d-spacing),[120] unit cell, background and profile parameters from Le Bail fitting were used as the initial inputs in Rietveld refinement and kept fixed at the first stage. Scaling factors, atomic positions, thermal displacement parameters and absorption coefficients were then refined separately. Following that, all the fixed parameters were released and refined together. Anisotropic thermal displacement factors and oxygen occupancies were the outcomes of the final run. The temperature-independent DIFA and absorption coefficients were kept fixed for all the measured temperatures for each sample.

- 3.2.4 Thermogravimetric analysis

To determine the absolute oxygen stoichiometry in the samples, we employed a NETZSCH STA 448 TGA/DSC (Germany) thermal analyzer. Approximately 50 mg powder was placed in an alumina crucible under a flow of 60 ml min^{-1} 5%H_2/95%N_2. The sample was held at a reference state of 70 ^oC (oxygen loss could happen at higher temperatures under reducing atmosphere) for 2 h to remove the absorbed H_2O or other species, followed by ramping to 1000 ^oC and holding for 30 hours to allow a full reduction to SrO, Co and $SrNbO_3$.[68] The absolute oxygen stoichiometry was calculated based on the mass difference between the reference state and the reduction products. A separate second TGA measurement was then conducted under the same temperature and conditions as during ND. With the known total initial oxygen stoichiometry determined by the reduction experiment, the oxygen stoichiometry in air as a function of temperature can then be mapped out according to weight changes. There was a 2-h holding at 120 ^oC for the second TGA

measurement to remove absorbed H_2O, which had no influence on the determination of the oxygen stoichiometry by ND.

- 3.2.5 Iodometric titration

In addition to TGA, the initial oxygen stoichiometry (3-δ) at RT was also determined by iodometric titration. A ~50 mg of the powders was first dissolved in 30 ml diluted HCl solution (1 M) under continuous N_2 bubbling to avoid oxidation. A 10 ml 0.2M KI solution was then added to reduce $Co^{3+/4+}$ to Co^{2+}. The Nb oxidation state was assumed to be fixed at 5+. A 0.01 M $Na_2S_2O_3$ was subsequently added dropwise to titrate the released elementary iodine inside the above solution. A few drops of a saturated starch solution were used to indicate the endpoint of titration. To predetermine the concentration of the $Na_2S_2O_3$ solution, ~25 mg $K_2Cr_2O_7$ powders were dissolved in the diluted HCl solution with excessive 0.2 M KI solution. The $Cr_2O_7^{2-}$ is expected to be fully reduced to Cr^{3+} by KI. Following the same procedure described, the produced elementary iodine was titrated using the $Na_2S_2O_3$ solution. The concentration of $Na_2S_2O_3$ and the average Co-ion oxidation state of the samples were then calculated based on the charge balance between the following reactions. The oxygen stoichiometry can be then derived based on the charge neutrality.

$$Co^{(2+n)+} + nI^- = Co^{2+} + \frac{n}{2} I_2 \tag{3-1}$$

$$I_2 + 2S_2O_3^{2-} = 2I^- + S_4O_6^{2-} \tag{3-2}$$

$$O_7^{2-} + 6I^- + 14H^+ = 2Cr^{3+} + 3I_2 + 7H_2O \tag{3-3}$$

3.3 Results and discussions

- 3.3.1 Phase evolution with temperature

The RT-XRD patterns for SCN10 are shown in Figure 3.1 and can be indexed by an a×a×2a tetragonal superlattice ("a" denotes the lattice constant of a 3C-cubic perovskite unit cell) using CMPR, a diffraction peak fitting/indexing software.[121]

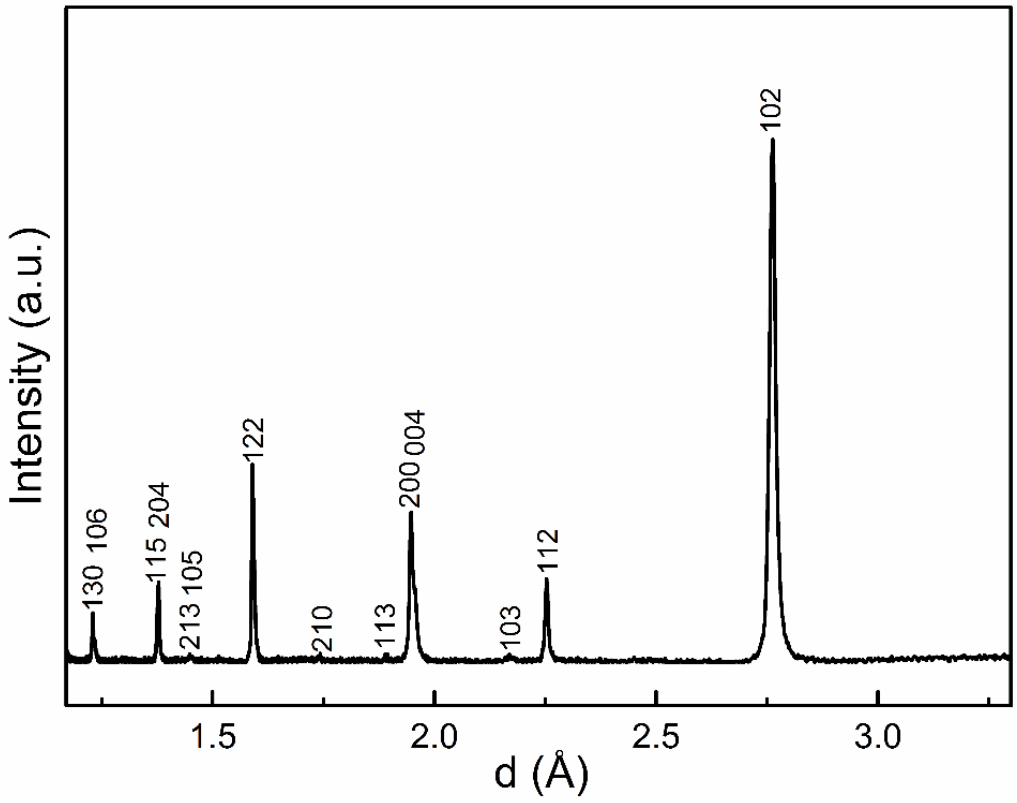

Figure 3.1 Room temperature XRD pattern for SCN10.

The ND patterns measured in the range of RT-900 ^{o}C are shown in Figure 3.2. The real-time phase evolution can be clearly visualized from the intensity contour plots. The RT-ND patterns can be indexed in space group P4/mmm (No. 123) using the same unit cell as determined by RT-XRD except for two peaks at d=2.34 and 1.78 Å, respectively. These

two peaks disappear above 75 °C in Figure 3.2, which excludes the possibility of impurities. It is unlikely that these two peaks belong to nuclear crystallographic Bragg reflections resulting from a new superlattice since more diffraction peaks would be expected in such a case. The brownmillerite phase $SrCoO_{2.5}$ has been reported to exhibit a G-type magnetically ordered structure from its Néel temperature (T_N = 537K) down to 10 K.[122] The later Rietveld refinements confirm that these two peaks are due to magnetic Bragg scattering. The literature also suggests that Neel temperature SCO-based materials strongly depends on oxygen stoichiometry and even strain level in thin film samples.[66, 123]

The accuracy of Néel temperature for the magnetic ordering could be influenced by the faster temperature ramps below 300 °C (10 °C min^{-1}). The second phase transformation is observed at 412 °C, where the structural symmetry changes from tetragonal P4/mmm (No. 123) to a simple 3C-type cubic perovskite with Pm-3m symmetry (No. 221). Again, these two transition temperatures were determined under dynamic temperature conditions. The cubic structure remains present all the way to 900 °C. Subsequent cooling reveals the reappearance of the tetragonal P4/mmm structure at their original (or very close to) onset temperatures, indicating that the phase transformation between P4/mmm and Pm-3m is reversible. The sample demonstrates good thermal stability up to 900 °C under the dynamic and atmospheric conditions specified. Our early high-temperature XRD (HTXRD) data shows that a secondary phase $Sr_6Co_5O_{15}$ emerges at >700 °C for SCN10 after being tempered for an extended period (>5 h).[58] The shorter holding time during the ND (2 h) experiments could be responsible for not observing this phase. The time-dependent phase composition has also been reported elsewhere, *e.g.* 1.3 wt% $Sr_6Co_5O_{15}$ and 2 wt% Co_3O_4 were observed to segregate from a SCN10 matrix after annealing at 750 °C for 4 days.[68]

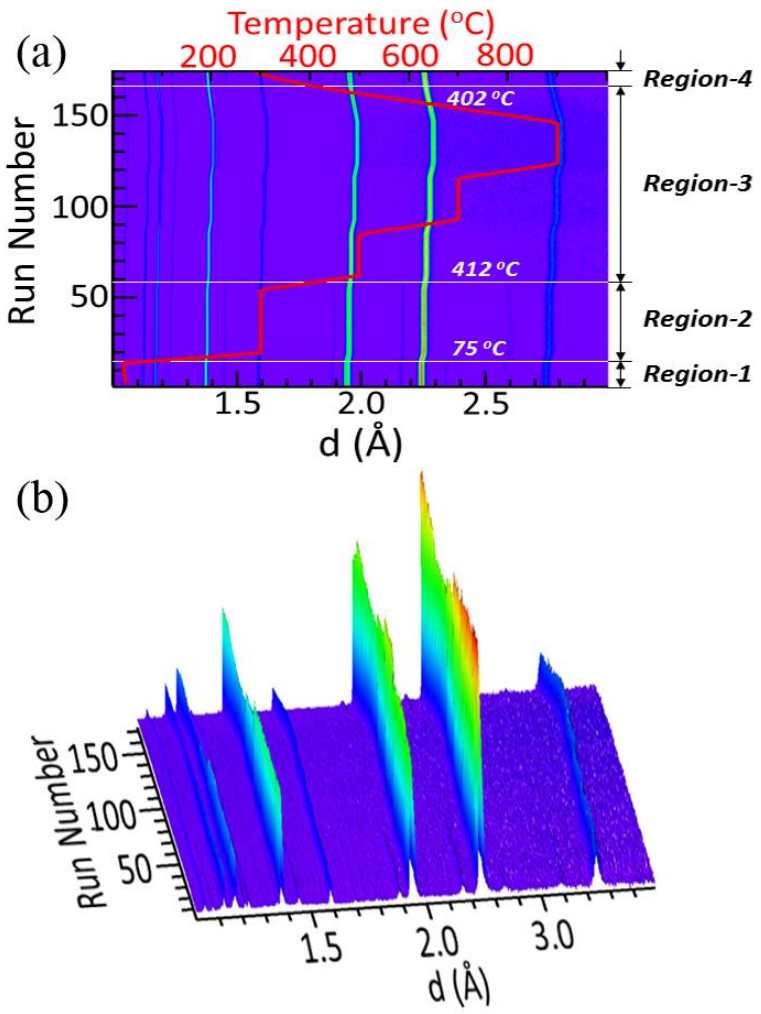

Figure 3.2 The 2D (a) and 3D (b) intensity contour plots of ND during heating and cooling. Region-1: Magnetic ordering P4/mmm; Region-2: P4/mmm; Region-3: Pm-3m; Region-4: P4/mmm. Each run represents a beam time of 5 minutes.

- 3.3.2 Rietveld refinement results

The Rietveld refinement plots of the RTND data is shown in Figure 3.3. Note that it is necessary to model both nuclear and magnetic Bragg scattering when refining the RTND patterns. The crystallographic space group P4/mmm with a×a×2a unit cell is used to describe the nuclear structure with Sr at 2h (1/2, 1/2, z), Co1/Nb1 at 1a (0, 0, 1/2), Co2/Nb2

at 1b (0, 0, 0), and O1, O2, O3 at 2f (1/2, 0, 0), 2g (0, 0, z) and 2e (1/2, 0, 1/2), respectively. The refinements must also consider the magnetic structure in which the Co-ions are magnetically ordered in a G-type structure with a propagation vector k = (1/2, 1/2, 0). The two types of Co-ions in the P4/mmm unit cell are antiferromagnetically coupled along the c-axis. The 2a×2a×2a unit cell has to be used for the magnetic lattice refinement given the ordered spin direction. The Shubnikov space group Cm′m′m is adopted to describe the magnetic structure while constraining the lattice constants with respect to those of the nuclear structure in P4/mmm symmetry, *i.e.* $a_{cmmm}=b_{cmmm}=2a_{p4/mmm}$, $c_{cmmm}=c_{p4/mmm}$. The 1a Co-site in the nuclear lattice transforms to 2a (0, 0, 0) and 2b (1/2, 0, 0) in the magnetic lattice, while the 1b Co-site in the nuclear lattice transforms to 2c (1/2, 0, 1/2) and 2d (0, 0, 1/2) in the magnetic lattice. The phase ratio and thermal displacement factors are coupled accordingly during the refinement based on the relation between the nuclear and magnetic structure. Both nuclear and magnetic structures derived from RTND are displayed in Figure 3.4, while Table 3.1 lists the fractional coordinates and magnetic moments for all magnetic atoms in the 2a×2a×2a unit cell. The refined magnetic moments M_z is 1.14 μ_B.

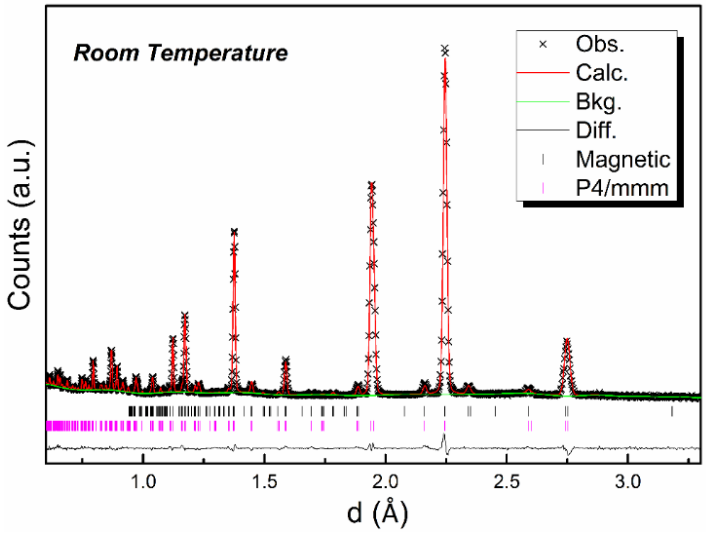

Figure 3.3 Rietveld refinement profiles for RTND data.

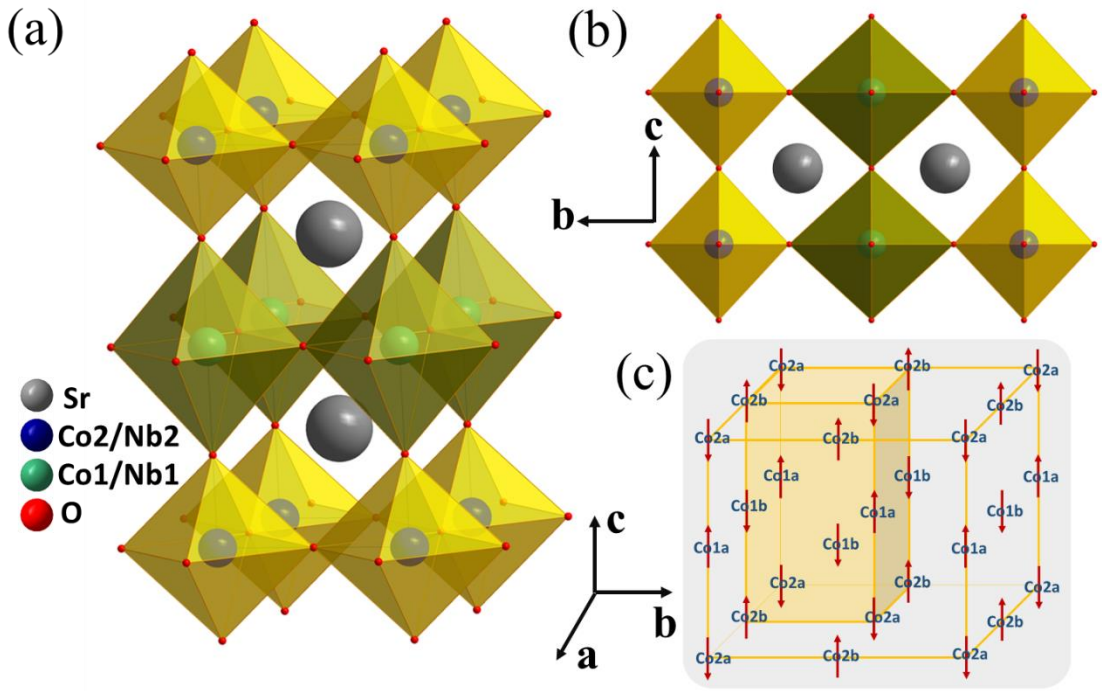

Figure 3.4 The refined P4/mmm structure at RT. (a) and (b) crystal structure projected from different direction; (c) magnetic unit cell.

Table 3.1 Atomic position and magnetic moment for Co ion in the magnetic unit.

Label	x	y	z	Moment (μ_B)
Co1a	1/2	0	1/2	1.11(4)
Co1b	0	0	1/2	-1.11(4)
Co2a	0	0	0	1.11(4)
Co2b	1/2	0	0	-1.11(4)

The ND patterns (above the magnetic ordering temperature) can be refined in either a P4/mmm or Pm-3m structure. Typical refinement profiles for P4/mmm and Pm-3m are shown in Figure 3.5. At T<412 ^{o}C, SCN10 exhibits a tetragonal P4/mmm structure where

there are two distinct Co-sites at 1a (0, 0, 0) and 1b (0, 0, 1/2) and three distinct O-sites at 2f (1/2, 0, 0), 2g (0, 0, z) and 2e (1/2, 0, 1/2), respectively. At T≥412 ºC, the P4/mmm structure transforms into the Pm-3m cubic structure, where the two distinct Co-sites merge into one site at 1a (0, 0, 0) and the three distinct O-sites become one at 3d (1/2, 0, 0). The phase transition temperature found in this work is higher than that reported in ref.[69], which reflects the difference of sensitivity in using ND and XRD to detect the structural change of a material. Clearly, the Pm-3m unit cell is only half of the P4/mmm unit cell. Figure 3.6 illustrates the model of this high-temperature Pm-3m cubic perovskite structure and Table 3.2 list the final structural parameters and reliable factors.

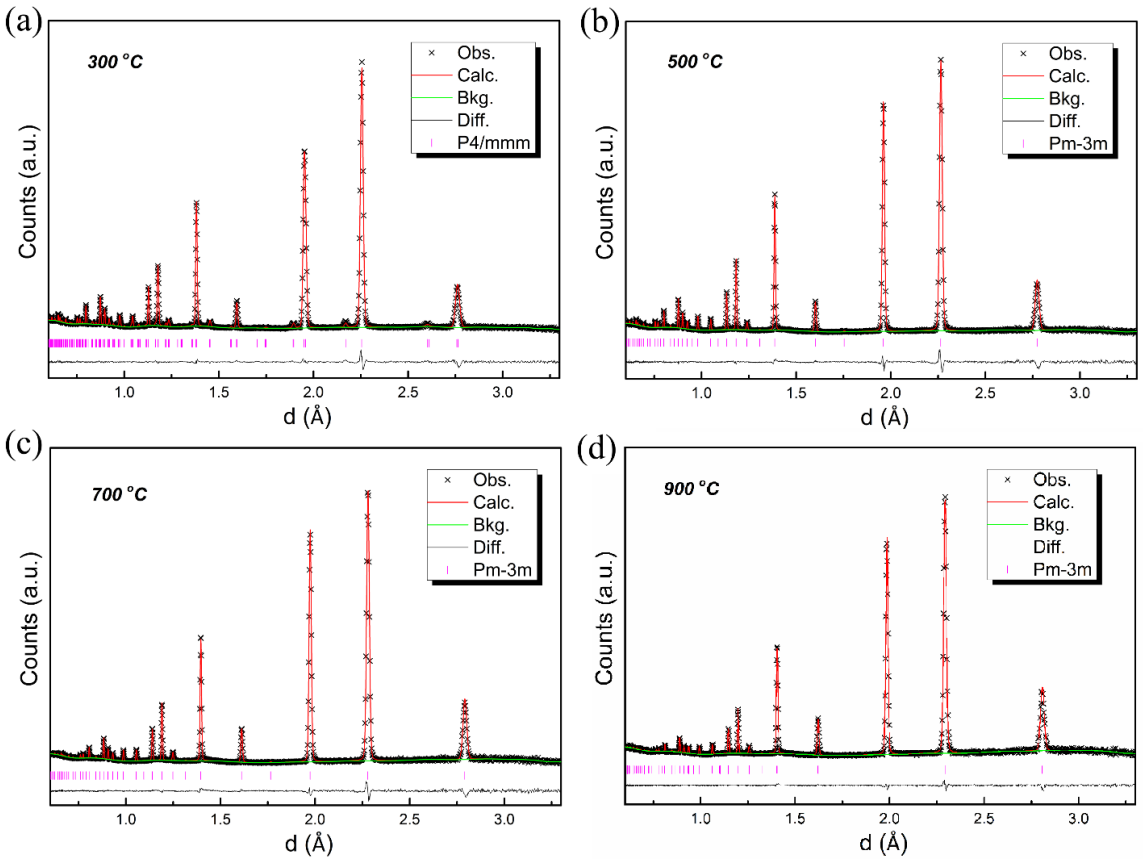

Figure 3.5 Exemplary Rietveld refinement profile with ND collected at elevated temperatures in air. (a) P4/mmm (300 ºC); (b) Pm-3m (500 ºC); (c) Pm-3m (700 ºC); (d) Pm-3m (900 ºC)

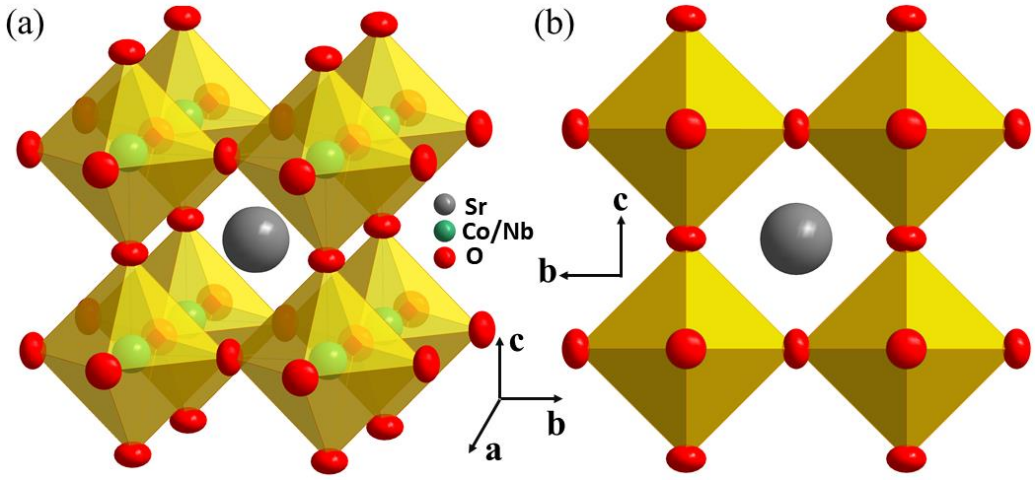

Figure 3.6 The high-temperature cubic structure model of Pm-3m obtained from ND. (a) View from an arbitrary direction; (b) view along the a-axis.

Table 3.2 Unit cell, atomic positions, occupancies, thermal displacement factors and reliable factors in P4/mmm, Z=2 and Pm-3m, Z=1.

Parameters	RT	300	500	700	900
Space Group	P4/mmm	P4/mmm	Pm-3m	Pm-3m	Pm-3m
a (Å)	3.88128(15)	3.89955(4)	3.92184(3)	3.94712(3)	3.97074(6)
c (Å)	7.80668(36)	7.83410(13)			
V (Å^3)	117.603(12)	119.129(3)	60.321(1)	61.495(1)	62.606(3)
	Sr 2*h* (1/2, 1/2, ~0.25)		Sr 1*b* (1/2, 1/2, 1/2)		
z	0.25902(23)	0.25729(15)			
100×U_{iso} (Å^2)	1.46(4)	2.03(1)	2.53(2)	3.27(2)	3.97(3)
f_{occ}*	1.0	1.0	1.0	1.0	1.0
	Co1/Nb1 *1b* (0, 0, 1/2)				
100×U_{iso} (Å^2)	1.46(14)	1.85(6)	1.75(6)	2.25(6)	2.85(12)
f_{occ}*	0.9/0.1	0.9/0.1	0.9/0.1	0.9/0.1	0.9/0.1
	Co2/Nb2 *1a* (0, 0, 0)				
100×U_{iso} (Å^2)	0.57(11)	0.88(5)			
f_{occ}*	0.9/0.1	0.9/0.1			
	O1 2*e* (1/2, 0, 0)				
100×U_{iso} (Å^2)	0.87(6)	1.71(2)			
f_{occ}	0.953(9)	0.955(3)			
	O2 2*g* (0, 0, ~0.75)				
z	0.76915(34)	0.76632(20)			

$100\times U_{eqv}$ (Å^2)[a]	3.49	4.11			
$100\times U_{11}=U_{22}$ (Å^2)	4.98(18)	5.57(6)			
$100\times U_{33}$ (Å^2)	0.50(11)	1.20(7)			
f_{occ}	1.0*	0.997(4)			
	O3 2*f* (1/2, 0, 1/2)			O 3*d* (1/2, 0, 0)	
$100\times U_{eqv}$ (Å^2)[a]	5.36	4.69	3.67	4.69	5.79
$100\times U_{11}$ (Å^2)	3.25(26)	2.09(10)	2.15(4)	2.93(4)	3.43(6)
$100\times U_{22}$ (Å^2)	8.11(56)	6.99(15)	4.44(2)	5.57(3)	6.98(5)
$100\times U_{33}$ (Å^2)	4.72(36)	5.00(13)	$U_{22}=U_{33}$	$U_{22}=U_{33}$	$U_{22}=U_{33}$
f_{occ}	0.723(14)	0.734(4)	0.868(2)	0.838(2)	0.821(3)
	Reliability factors				
R_{wp} (%)	4.25	2.73	2.58	2.40	2.20
R_p (%)	3.14	2.00	1.99	1.85	1.70
R_{bragg} (%)	7.22	4.86	5.03	5.14	3.65
χ^2	5.712	2.265	2.026	1.771	1.484

* Fixed; [a] Anisotropic thermal displacement factors *U12* = *U13* = *U23* = 0.

It is noted that both the profile R values (R_p) and the weighted-profile R values (R_{wp}) are very low, especially for T ≥ 300 ºC, indicating a good fit of the structural models to the pattern.[124] The reliability factors are slightly higher, but still generally acceptable for RT data (*e.g.*, R_p=4.25%, R_{wp}=3.14%) and comparable to a ND study of isostructural Sb-doped SCO (R_p=5.66%, R_{wp}=7.29%).[55] The changes of the unit cell constants and volume with temperature are plotted in Figure 3.7. For comparison purpose, the unit cell constants and volume of the P4/mmm phase are normalized to those of Pm-3m by a factor of (a×2+c)/4 and 1/2, respectively. Both unit cell constants and volume expansion vary linearly with temperature and display a discontinuity at the phase transition temperature. The average linear thermal expansion coefficients are 15.7×10^{-6} K^{-1} and 31.2×10^{-6} K^{-1} before and after phase transition, respectively. The oxygen loss with temperature, which will be shown in later TGA results, accounts for the greater slopes observed above the phase transition temperature.

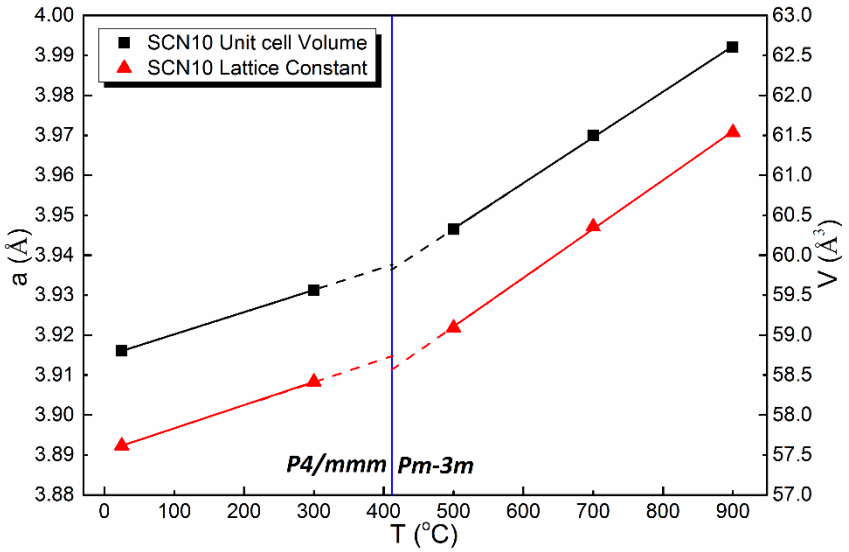

Figure 3.7 Unit cell constant and volume of SCN10 vs temperature. The blue line represents phase transition temperature. The error bars are much smaller than the size of symbols.

The neutron scattering length of Nb (7.054 fm) is almost 3× the one of Co (2.490 fm). Therefore, it should be easily determined by ND if Nb atoms prefer for a specific Co-site in the P4/mmm structure. In contrast to Mo-[56] or Sb-[125] doped SCO, where dopant atoms are determined to preferentially occupy the Co1-site, we find that Nb atoms show no preference over the two Co-sites. For example, at RT, the refinement of SCN10 patterns reveals an equal distribution of Nb on the two Co-sites: Co1/Nb1=0.89/0.11 and Co2/Nb2=0.91/0.09, respectively. The proximity of the Co/Nb ratio to the doping concentration on these two Co-sites suggests that Nb has no preference for a Co-site in the cation lattice. On the other hand, the occupancy at O2 (0, 0, z) site converges to a value slightly higher than unity, which suggests that O2-site is fully occupied by oxygen at RT and was therefore fixed at 1.0 in the refinement.

- 3.3.3 Oxygen stoichiometry and Co-ion oxidation state vs temperature

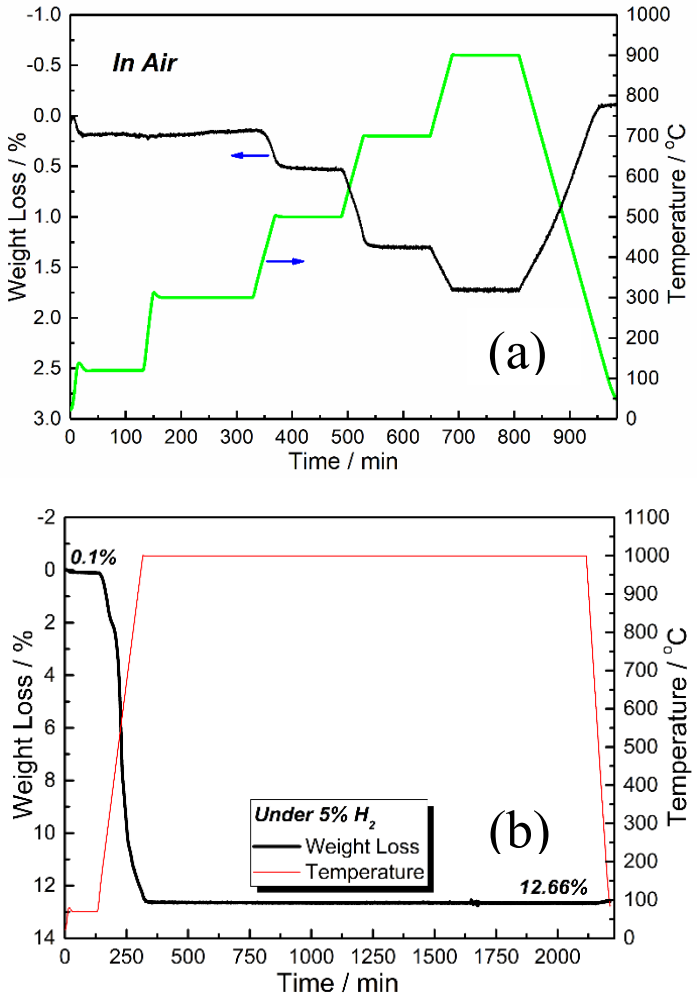

Figure 3.8 TGA profiles under air; (b) TGA profiles under 5% H_2.

The variation of the oxygen stoichiometry (3-δ) *vs* temperature was also derived from the weight changes measured by TGA and is compared to the results obtained from ND. Figure 3.8 (a) and (b) show the TGA curves measured in air and 5% H_2-N_2, respectively. Figure 3.9 compares the calculated oxygen stoichiometry and Co-ion oxidation-state at different temperatures, from both TGA and ND. The oxygen stoichiometry *vs* temperature obtained from ND has a similar trend to those by TGA, *i.e.* a peaking (3-δ) in low-temperature

regime, but the absolute value from ND is systematically ~0.1 lower, which has also been observed in other SCO systems.[100-101] The TGA results indicate a slow oxygen uptake from RT to *ca.*350 °C before they begin to lose oxygen; these observations are consistent with our previous results on Nb-doped SCO[58] and Y-doped SCO.[126] The initial total oxygen stoichiometry determined from the full reduction TGA method, Figure 3.8 (b), is 2.72, which is in excellent agreement with those determined by iodometric titration (2.72). This value is lower than 2.85 reported by Zhang, et al,[114] which is likely resulted from the different thermal history (such as cooling rate etc.) of sample preparation. The compositions for SCN10 at RT should, therefore, be represented by $SrCo_{0.9}Nb_{0.1}O_{2.72}$, respectively.

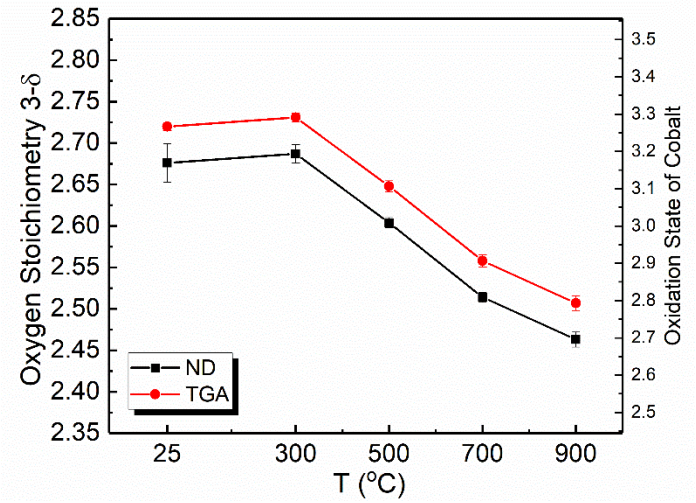

Figure 3.9 The calculated oxygen stoichiometry and Co-ion oxidation-state as a function of temperature.

The oxidation states of Co-ions and oxygen stoichiometry are summarized in Table 3.3 at selected temperatures. The average Co-ion oxidation state first increases from +3.27 to +3.29 from RT to 300 °C followed by decreasing to +3.11 at 500 °C, +2.91 at 700 °C

and +2.79 at 900 ºC, suggesting the growing dominance of the Co^{3+}/Co^{2+} over the Co^{4+}/Co^{3+} redox couple at elevated temperatures.

Table 3.3 Co-ion oxidation-state and oxygen stoichiometry (in parenthesis) at different temperatures calculated from TGA and ND.

T (ºC)	TGA	ND	Structure
RT	+3.27 (2.720)	+3.17 (2.676)	P4/mmm
300	+3.29 (2.731)	+3.19 (2.687)	P4/mmm
500	+3.11 (2.648)	+3.01 (2.604)	Pm-3m
700	+2.91 (2.558)	+2.81 (2.514)	Pm-3m
900	+2.79 (2.507)	+2.70 (2.463)	Pm-3m

It is worth mentioning that the oxygen stoichiometry and Co-ion oxidation state closely follow our previously observed conductivity trends,[58] which exhibits a "semiconductor-to-metal" transition behavior at an onset temperature (~400 ºC), below and above which hole conduction is observed with a lower activation energy E_a (*c.a.* 0.05 eV) and higher E_a (*c.a.* 0.10 eV), respectively. Typically, E_a for an electronic conductor with a small-polaron conduction mechanism is > 0.10 eV, whereas it is ≤ 0.10 eV for the case of a large-polaron conduction.[127] For the SCN system, we have established a defect chemistry model showing that at a high oxygen stoichiometry (and/or low temperature) where the redox couple $Co^{4+/3+}$ dominates, the Co-3d orbitals hybridize strongly with the O-2p orbitals, leading to a broadening of the conduction band and the formation of delocalized large-polarons.[128] In comparison, at low oxygen stoichiometry (and/or high temperature) when the redox couple $Co^{3+/2+}$ dominates, the hybridization between Co-3d

and O-2p becomes weaker and Co^{2+} (viewed as a negatively charged free electron) can be trapped at positively charged Nb-dopant sites ($Nb_{Co}^{\cdot\cdot}$), forming a relatively narrow band and producing localized small-polarons.[52] Hence, the electronic conduction in SCN system transitions from a delocalized large-polaron behavior to a localized small-polaron behavior with increasing temperature or decreasing oxygen stoichiometry.

- 3.3.4 Local Co-O bond length and coordination number

As listed in Table 3.2, the main oxygen deficiencies are populated at the O3-site in the low-temperature P4/mmm structure, suggesting that Co1 are surrounded by a large amount of oxygen vacancies. The long-range ordering of oxygen vacancies in P4/mmm, which couples with two different Co-ion sites, is, therefore, the origin of the tetragonal structure. A careful examination on the Co-O bond length given in Table 3.4 further reveals that the Co-O bonding differs in the two Co-ion sites. For example, along the c-axis, the Co2-O2 bonds are remarkably shorter than Co1-O2, *e.g.* 1.80 Å (Co2-O2) *vs* 2.10 Å (Co1-O2) at RT, suggesting a higher oxidation-state of Co1-ion.

Table 3.4 Refined Co-O bond length for tetragonal P4/mmm and cubic Pm-3m at RT, 300, 500, 700, and 900 ºC.

Bonds (Å)	RT	300 ºC
Co1/Nb1-O1 (×4)	2.1012(27)	2.0864(15)
Co1/Nb1-O2 (×2)	1.94064(8)	1.94977(2)
Average	1.994	1.995
Co2/Nb2-O2 (×2)	1.94064(8)	1.94977(2)
Co2/Nb2-O3 (×4)	1.8022(27)	1.8307(15)
Average	1.894	1.910
Total Average	1.944	1.952
500 ºC	700 ºC	900 ºC
Co/Nb-O (×6)		

1.96092(2)	1.97356(2)	1.98537(3)

Bond valence sums (BVS) can be used to further evaluate the average valence of an individual ion within its local coordinating environment. The BVS of a cation *i* is the sum of the individual bond valence v_{ij}, where j is the surrounding cation, defined by:[129]

$$v_{ij} = exp\left(\frac{r_o - r_{ij}}{b}\right) \tag{3-4}$$

here r_{ij} is the observed bond distances between ions *i* and *j*; r_o is the ideal bond distances and *b* is an empirical constant (0.37 Å). The r_o values for Co^{3+}-O and Nb^{5+}-O are 1.70 Å and 1.911 Å, respectively.[129] The weighted r_o used for BVS calculation is given by:[130]

$$r_{o(weighted)} = r_{o(Co)} \times Occupancy_{Co} + r_{o(Nb)} \times Occupancy_{Nb} \tag{3-5}$$

At RT, the calculated BVS are 3.80 and 2.92 for Co2-site and Co1-site, respectively. The remarkable difference in BVS between Co1-site and Co2-site strongly suggest a charge ordering at these two Co-sites assuming that the Nb-ions have a fixed oxidation state of +5. In fact, it has been previously proposed that the charge ordering occurs in the tetragonal structure where a mixed oxidation state of $Co^{3+/4+}$ at Co2 site and Co^{3+} at Co1 site follows a full charge disproportionation.[9,46] The intermediate-spin state Co^{3+} ($3d^6$) in CoO_6 octahedra with a *d*-electron configuration $t_{2g}^5e_g^1$ is the fundamental reason for the elongation along the c-axis in the $Co1O_6$ octahedra and shortening in the $Co2O_6$ octahedra in order to accommodate the charge ordering. This behavior is known as Jahn-Teller distortion.[131]

The oxygen occupancy and cation-coordination also change with temperature. The O3-occupancy in the tetragonal P4/mmm structure increases with temperature before

transforming to the cubic Pm-3m structure as listed in Table 3.2. This increase in O3-occupancy correlates well with the oxygen uptake behavior observed in the TGA profile shown in Fig. 2.8. The Rietveld refinements results in Table 3.2 show that this increased oxygen-ion at O3 site comes from the neighboring O2-site, which can be attributed to the enhanced thermal diffusion at this temperature.

The oxygen-coordination number (CN) of Co1 and Co2 are shown in Figure 3.10 (a) as a function of temperature. It is evident that more oxygen vacancies are populated at O3-site around the Co1-site, leading to a lower CN in the P4/mmm structure. As the temperature increases, the CNs for Co1 and Co2 sites converge towards that of the cubic structure. On the other hand, Figure 2.10 (b) suggest that the Jahn-Teller distortion becomes weaker at higher temperatures, where all the Co-O bond lengths converge to become identical in the cubic structure. Based on the above observation, it can be concluded that the local structural change in $SrCoO_{3-\delta}$-based materials is mainly due to O-site rearrangements.

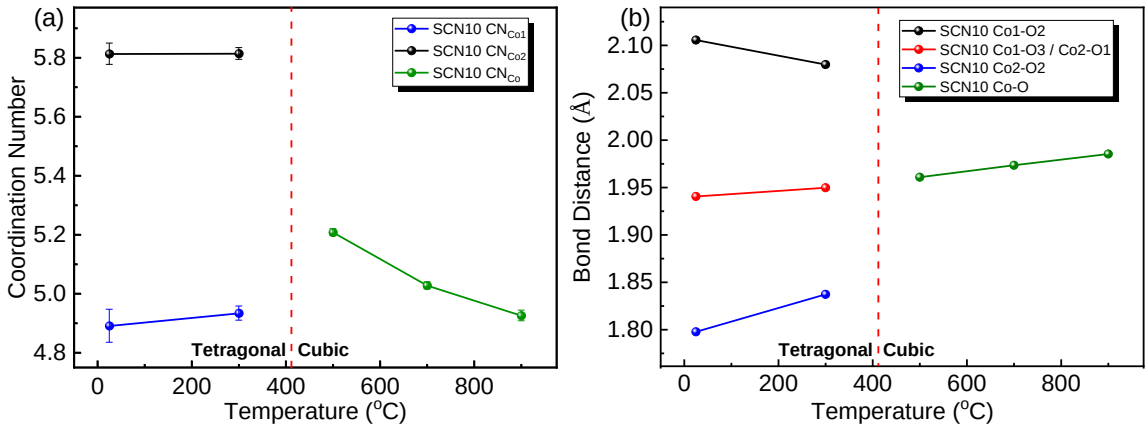

Figure 3.10 Local structural changes vs temperature. (a) CN of Co-ions; (b) Co-O distances. The red line represents the phase transition temperature. Some error bars are smaller than the size of the symbols in (a) and (b).

It is worth pointing out that, since the magnetic structure is not fully developed at RT, no diffraction peaks related to the different magnetic moments of the two Co-ions can be observed even though charge ordering at the Co1 and Co2 sites is suggested by the CN and Co-O distances from the refinement results. This explains the smaller refined moments of 1.14 μ_B compared to the theoretical value 2.83 μ_B of intermediate spin Co^{3+}.

- 3.3.5 Thermal displacement factor of oxide-ions

The thermal displacement factors *U* are refined and examined as a proxy for the thermal motions of O^{2-}; the results are given in Table 3.2. The anisotropic refinement of the O1-site yields negative U_{11} values. Hence only U_{iso} are refined for the O1-site. The anisotropic U refinement for O2-site shows a large thermal motion perpendicular to the c-axis in the P4/mmm structure. For the O3-site, it shows large values of U in all the three directions with the largest one also being perpendicular to the c-axis. The equivalent isotropic thermal factors U_{eqv} for O3 is 0.0536 $Å^2$ at RT, significantly larger than that for a metal oxide in which metal cation and O^{2-} are tightly bounded (a typical value is *ca.* 0.006 $Å^2$).[80]

For the Pm-3m cubic structure, a larger equivalent thermal motion of O^{2-} is also observed, *i. e.* U_{eqv} = 0.0469 $Å^2$ at 700 ^oC. A larger U value suggests a greater mobility of O^{2-} for SCN-series materials, implying that SCN is a good candidate as a mixed oxide-ion and hole conductor. Figure 3.11 illustrates the reconstructed oxygen sub-lattices depicting the thermal displacement ellipsoids at RT and 700 ^oC. The largest thermal motion of O^{2-} in P4/mmm occurs along the (002) plane, on which O3-site oxygen vacancies are mostly concentrated. These results are consistent with the diffusional pathways calculated from bond valence method (BVM) that indicates a hindered O^{2-} conduction paths along [001].[69] In the isotropic cubic Pm-3m structure, the thermal O^{2-} motion directions and amplitude

ratios of all face planes are similar to those of (002) plane in the P4/mmm structure. The most likely diffusion path follows a curved rather than a straight-line along the edge of a CoO_6 octahedron as illustrated in Figure 3.11. Similar oxygen conduction pathways were also proposed for the isostructural $La_{0.6}Sr_{0.4}CoO_{3-\delta}$ and $(La_{0.8}Sr_{0.2})(Ga_{0.8}Mg_{0.15}Co_{0.05})O_{2.8}$.[132-133]

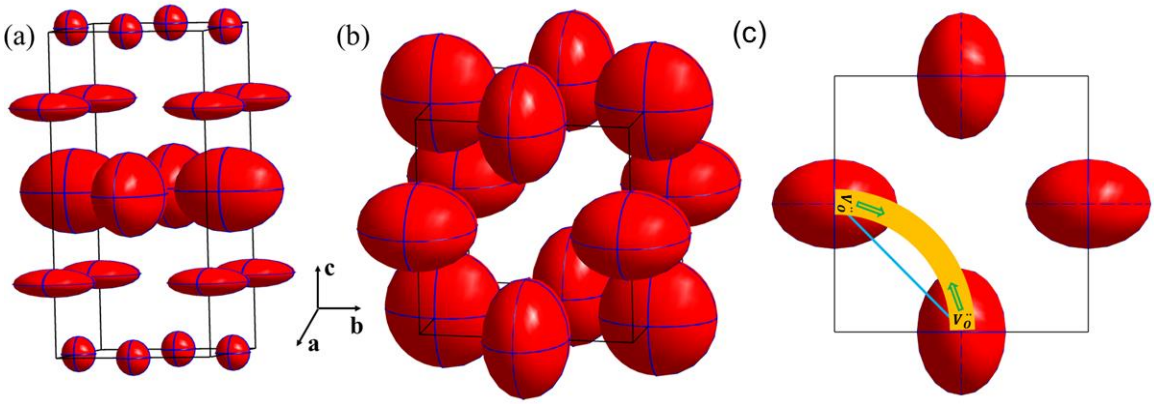

Figure 3.11 Oxygen sub-lattices showing the thermal displacement orientation and magnitude for SCN10 at (a) RT and (b) an arbitrary direction at 700 °C; (c) (200) plane of P4/mmm at RT.

3.4 Conclusions

In summary, the crystal structures and oxygen stoichiometry of $SrCo_{0.9}Nb_{0.1}O_{2.72}$ (SCN10) have been systematically characterized by *in-situ* neutron diffraction and thermogravimetric analysis as a function of temperature. SCN10 exhibits a tetragonal lattice (P4/mmm) with G-type antiferromagnetically ordered magnetic structure between RT and 75 °C, above which the magnetic ordering disappears. A phase transition from tetragonal (P4/mmm) to primitive cubic (Pm-3m) occurs at 412 °C.

For the intermediate-temperature tetragonal phase (P4/mmm), oxygen vacancies are mainly populated at the O3-site and distributed around the Co1-site. The calculated Co coordination number from the refined oxygen occupancies suggests a charge disproportionation with mixed Co^{3+}/Co^{4+} at the Co2 sites and Co^{3+} at the Co1 sites. The induced expansion along the c-axis by the intermediate-spin state of Co^{3+} distorts two types of CoO_6 octahedra in the P4/mmm structure. Before transforming into the cubic phase (Pm-3m), oxygen vacancies are distributed more evenly across the three O-sites and the tetragonal structure becomes increasingly symmetrical with increasing temperature. Overall, the oxygen vacancies (or stoichiometry) could be viewed as an indicator of the local structural distortions and symmetry transformations. SCN10 shows large thermal displacement factors, suggesting a good ionic mobility of O^{2-}. Combined with the high concentration of oxygen vacancies per unit cell, an enhanced oxide-ion conduction is expected.

CHAPTER 4

Ta-DOPED $SrCoO_{3-\delta}$ AS CATHODE FOR SOLID OXIDE FUEL CELL

4.1 Introduction

For SCO-based materials, it has been shown that the oxygen stoichiometry plays a crucial role in thermal stability, electronic conductivity, and electrochemical activity. Losing too much lattice oxygen in the SCO structure would result in the formation of less conductive and poorly active $Sr_2Co_2O_5$ or $Sr_6Co_5O_{15}$. On the other hand, maintaining a higher oxygen stoichiometry in SCO can promote a larger hybridization between O-2p and Co-3d orbitals, thus giving rise to a higher oxidation state of Co-ions and electronic hole-conductivity. To retain a higher oxygen stoichiometry at elevated temperatures, the bonding of the dopant with oxygen needs to be stronger than the host Co-O. For example, the bond of Nb-O is stronger than that of Co-O, thus improving the thermal stability of SCO to <700 ºC.[58]

In this chapter, the crystal structure of Ta-doped SCO is examined, and particularly compared with its analogous system Nb-doped SCO. The comparison may yield critical insights into what is the key differentiator of the properties between Ta-SCO and Nb-SCO because Ta^{5+} (VI coordination) has an identical ionic radius (0.64 Å) to that of Nb^{5+}, which avoids the cation-size effect on properties and in turn allows a more accurate evaluation of thermal stability based on Average Bonding Energy (ABE) theory.[134-136] In a prior work[70],

some properties of Ta-SCO were compared with Nb-SCO and interpreted by Pauling's electronegativity theory. However, the authors mistakenly concluded that a better electrochemical performance observed in Ta-SCO than Nb-SCO was due to a lower electronegativity value of Ta^{5+} (1.8) *vs* Nb^{5+} (1.87), which results in a weaker Ta-O bonding; the latter was not only contradictory to Pauling's electronegativity theory[137-138] in that a smaller electronegativity difference between cation and anion results in a weaker bonding, but also their own thermogravimetric analysis (TGA) results showing less weight loss for the Ta-doped SCO system.[70] Our results show that Ta-O bonding is stronger than that of Nb-O in doped SCO system, which is also the fundamental reason for the Ta-SCO system to maintain a higher oxygen stoichiometry and oxidation state of Co-ions.

4.2 Experimental Procedure

- 4.2.1 Sample Preparation

Two compositions of $SrCo_{1-x}Ta_xO_{3-\delta}$ (x=0.05, 0.10, denoted as SCT5 and SCT10, respectively, or collectively SCT hereinafter) were synthesized by standard solid-state reaction. First, high-purity starting materials of $SrCO_3$ (≥99.9%, Aldrich), Co_3O_4 (99.7%, Alfa Aesar) and Ta_2O_5 (99.9%, Alfa Aesar) in stoichiometric amounts were intimately mixed in an agate mortar with ethanol alcohol, followed by drying, pelletizing and calcining at 1000 °C in air for 10 h. Second, the as-calcined pellets were broken up and ball-milled into submicron powders before pelletizing and sintering at 1200 °C for 10 hours. To obtain a pure single phase, step-2 was repeated 2 times. Finally, after confirming the phase purity, the powders were mixed with a 1-wt% PVB binder and pressed into rectangular bars (45mm×6mm×4mm) by static uniaxial pressing. The bar samples were

finally sintered in air at 1200 ºC for 10 hours to achieve a dense microstructure for conductivity measurement as well as other characterization.

- 4.2.2 Structural characterization

The phase composition of SCT samples were first examined with an X-ray diffractometer (MiniFlex II, Rigaku, Japan) equipped with Cu Kα radiation (□=1.5418 Å) over a 2□=10-90 º range in a step size of 0.02º at a scanning rate of 1º min^{-1}. Their phase evolution with temperature in the range of RT-800 ºC was studied in air by a high-temperature (HT) X-ray diffractometer (X1 Theta-Theta, Scintag, USA) equipped with graphite-monochromatized Cu Kα radiation (λ = 1.5418 Å) over a 2□=10 - 110 º range in a step size of 0.02 º at a scanning rate of 1º min^{-1}. During HT-XRD measurement, approximately 1-h equilibrium time was given at each temperature before data collection.

In-situ Neutron diffraction (ND) was conducted in air as a function of temperature on POWGEN,[139] a time-of-flight diffractometer, at the Spallation Neutron Source in Oak Ridge National Laboratory. A neutron beam in 1.333 Å wavelength was used for diffraction in a *d*-space range of 0.5-4.0 Å. An approximately 10 g sample with *ca*. 10-μm particle size was loaded inside a 40-mm long and 10-mm diameter quartz basket with a fritted bottom. A vacuum vanadium foil element furnace enclosing a fused silica quartz sample chamber was used to heat the sample. Diffraction patterns were collected under a 200 sccm flow of 20%O_2-N_2 at 300, 500, 700 and 850 ºC, respectively. The data collection time was 3 h at 300 ºC, while 2 h for all other temperatures. The last 40-min data for each temperature were used for refinement, which corresponds to a total accelerator charge of 3 coulombs. Diffraction pattern for an empty quartz basket at each temperature was subtracted from the sample scans before performing further analysis. The room-temperature ND was collected

from the same beamline with ~5 g sample sealed in vanadium cans under a helium atmosphere.

- 4.2.3 Determination of oxygen stoichiometry

The oxygen stoichiometry (3-δ) of SCT10 in air as a function of temperature was determined by thermogravimetric analysis (TGA, NETZSCH STA 448 TGA/DSC, Germany) and ND methods. For the TGA method, the initial oxygen stoichiometry ($3-\delta_o$) needs to be determined first. Two approaches were experimented for this purpose: iodometric titration and full reduction TGA. For the iodometric titration method, a 30 mg powder was first dissolved in a 6 M HCl solution with excessive KI. The original oxidation state of the Co ions in the dissolved sample is expected to be fully reduced to 2+ by KI. By titrating $Na_2S_2O_3$ into the solution and assuming that Ta has a fixed oxidation state (5+), the average oxidation state of Co-ions can be determined. From the charge neutrality, the original oxygen stoichiometry at room temperature can be calculated out.

For the full reduction TGA method, a 5%H_2-95%N_2 mixture was used as the reducing gas to fully reduce the sample (~50 mg) into SrO, Co and $SrTaO_3$. The sample was first kept at 70 ºC for 2 h to remove the absorbed H_2O on the particles surface, followed by heating up to 1000 ºC at 10 º/min and holding for 30 hours.

The final oxygen stoichiometry in air *vs* temperature was obtained from the initial oxygen stoichiometry determined by iodometric titration or full reduction TGA and TGA profile measured in air with holding temperatures at 300, 500, 700 and 900 ºC. The obtained results were also compared with those obtained from ND.

- 4.2.4 Thermal expansion characterization

The Thermal expansion coefficients (TECs) of SCT samples were also measured using a NETZSCH DIL 402PC/4 dilatometer. The measurement was carried out in a temperature range from RT to 900 ºC at a ramp rate of 5 ºC·min^{-1} with air flow at 50 ml·min^{-1}.

4.3 Results and Discussion

- 4.3.1 Phase composition at room temperature

The room-temperature (RT) XRD patterns of the synthesized SCT05 and SCT10 samples are shown and compared in Figure 4.1 (a) with the undoped SCO. At elevated temperatures, pure SCO is known to thermally decompose into $Sr_2Co_2O_5$, which absorbs oxygen from air during cooling process to form hexagonal $Sr_6Co_5O_{15}$ and Co_3O_4. The two reactions can be expressed by:

$$SrCoO_{3-\delta} = SrCoO_{2.5} + \frac{0.5-\delta}{2}O_2 \uparrow \quad (4\text{-}1)$$

$$6SrCoO_{2.5} + \frac{2}{3}O_2 = Sr_6Co_5O_{15} + \frac{1}{3}Co_3O_4 \quad (4\text{-}2)$$

Figure 4.1 (a) of RT-XRD confirms that the pure undoped SCO is indeed decomposed to $Sr_2Co_2O_5$, $Sr_6Co_5O_{15}$ and Co_3O_4. In comparison, the doped samples show a major primitive cubic structure with two exceptional peaks at 42º and 48.5º (see the inset). As pointed out in our previous work on Nb-doped SCO,[58] these two peaks are indicative of oxygen-ordered superlattice crystalized in tetragonal (SG: P4/mmm) with a unit cell dimension of $a_t=b_t\approx a_0$, $c_t= 2a_0$, where a_0 is the lattice parameter of a perovskite cubic cell. As the Ta-content increases, the intensities of these two superlattice peaks become weaker, suggesting that the Ta-dopant inhibits formation of the oxygen-ordered superstructure. Figure 4.1 (b)

further shows a shift of the major perovskite peak (100) towards lower 2θ with increasing Ta-content, implying that the lattice has been expanded by the substitution of larger Ta^{5+} on $Co^{3+/4+}$.

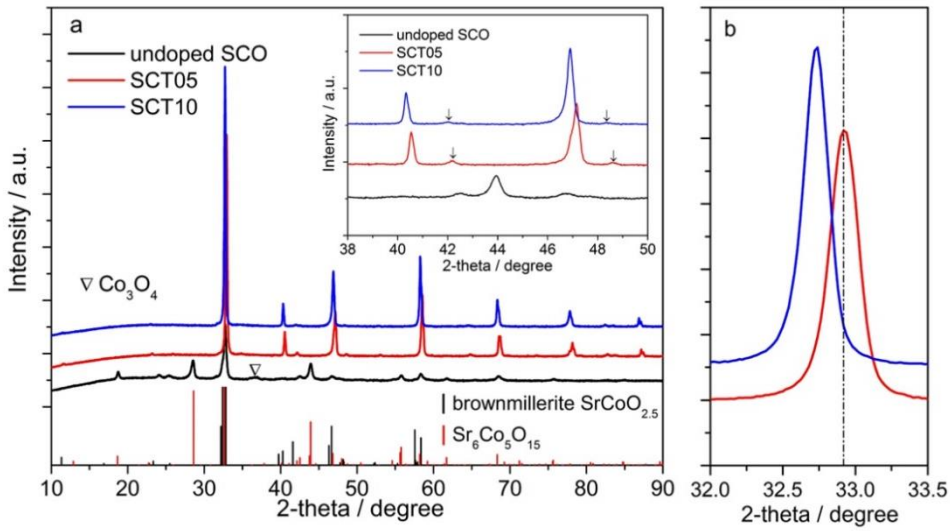

Figure 4.1 XRD patterns of SCT05 and SCT10 samples. (a) Overall patterns in comparison with the undoped SCO; (b) expanded view of the main peak of the perovskite phase.

The above crystal structures of SCT05 and SCT10 at RT are further confirmed by room temperature ND. Figure 4.2 (a) and (b) show reasonable goodness of the fit to diffraction data with reasonably low Bragg-intensity R value (R_p) and weighted-profile R value (R_{wp}) when both tetragonal P4/mmm and cubic Pm-3m structures are considered. The refinement suggests that SCT05 contains more tetragonal P4/mmm than cubic Pm-3m phase (11.3% Pm-3m *vs* 88.7% P4/mmm), whereas the SCT10 holds more cubic Pm-3m than tetragonal P4/mmm phase (96.2% Pm-3m *vs* 3.8% P4/mmm). This finding is consistent with that of XRD, where higher Ta-doping is observed to have less tetragonal

superlattice. Table 4.1 lists all the crystallographic positions refined based on P4/mmm and Pm-3m structures.

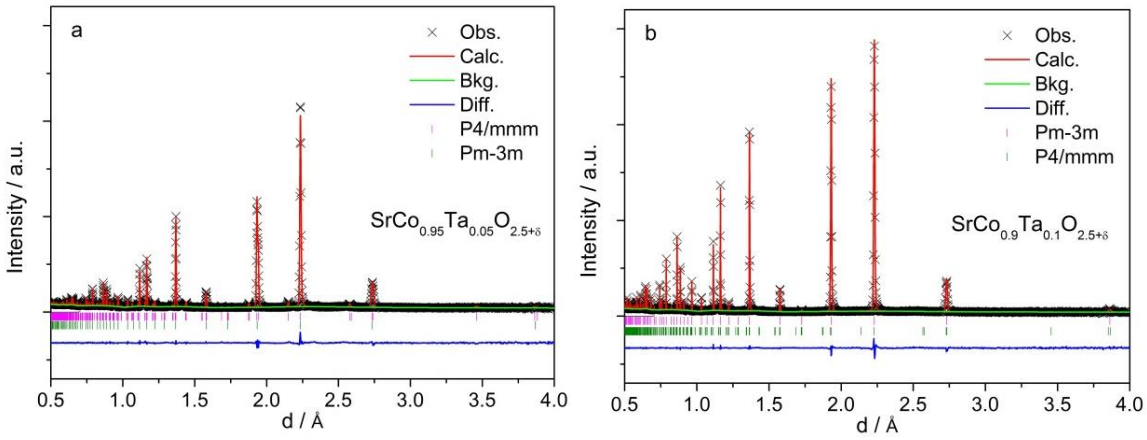

Figure 4.2 Rietveld refinement profiles of (a) SCT05 and (b) SCT10 with ND collected at RT.

Table 4.1 ND-derived unit cell, atomic positions, occupancies, thermal displacement factors and reliable factors for P4/mmm and Pm-3m structures in SCT05 and SCT10.

Space Group	P4/mmm	Pm-3m
a (Å)	3.86481(2)	3.86161(1)
c (Å)	7.76578(9)	
V (Å^3)	115.995(2)	57.585
	Sr 2*h* (1/2, 1/2, z)	Sr 1*b* (1/2, 1/2, 1/2)
z	0.26348(12)	
100×U_{iso} (Å^2)	1.08(1)	1.13(1)
f_{occ}*	1	1
	Co1/Ta1 *1b* (0, 0, 1/2)	Co/Ta 1*a* (0, 0, 0)
100×U_{iso} (Å^2)	0.95(5)	0.69(1)
f_{occ}*	0.95/0.05	0.9/0.1
	Co2/Nb2 *1a* (0, 0, 0)	-
100×U_{iso} (Å^2)	0.85(5)	
f_{occ}*	0.95/0.05	
	O1 2*e* (1/2, 0, 0)	-
100×U_{iso} (Å^2)	3.72(4)	
f_{occ}	0.668(5)	
	O2 2*g* (0, 0, z)	-
z	0.76397(20)	

$100\times U_{eqv}$ (Å^2)[a]	3.46	
$100\times U_{11}=U_{22}$ (Å^2)	4.64(5)	
$100\times U_{33}$ (Å^2)	1.11(6)	
f_{occ}	0.989(5)	
	O3 2*f* (1/2, 0, 1/2)	O 3*d* (1/2, 0, 0)
$100\times U_{eqv}$ (Å^2)[a]	0.79	1.76
$100\times U_{11}$ (Å^2)	0.47(3)	1.04(1)
$100\times U_{22}$ (Å^2)	0.43(3)	2.11(1)
$100\times U_{33}$ (Å^2)	1.47(4)	2.11(1)
f_{occ}	0.984(3)	0.927(1)
	Reliability factors	
R_{wp} (%)	5.30	3.91
R_p (%)	6.21	5.15
χ^2	25.10	13.91

[*] Fixed; [a] Anisotropic thermal displacement factors *U12* = *U13* = *U23* = 0.

- 4.3.2 Phase evolution with temperature

The phase evolution of SCT05 and SCT10 with temperatures was investigated by high-temperature XRD (HT-XRD) and ND. Figure 4.3 (a) of HT-XRD shows that SCT05 undergoes a partial phase decomposition into $SrCO_3$ and Co_3O_4/CoO above 500 ºC in ambient air containing CO_2, even though RT-XRD pattern shown in Figure 4.1 did not reveal these impurity phases. The partially decomposed SrO immediately reacts with CO_2 in the ambient air, forming $SrCO_3$ as indicated in the pattern. In comparison, Figure 4.3 (b) shows that SCT10 maintains a primitive cubic structure over the entire temperature range of RT-800 ºC without any impurity phase. In addition, the two superlattice-related peaks at 42º and 48.5º become weakened for both samples as the temperature increases, and completely disappeared at ≥400 ºC for SCT05 and ≥200 ºC for SCT10, suggesting that the dissolution of oxygen-ordered superlattice into oxygen-disordered primitive cubic structure has taken place at higher temperatures.

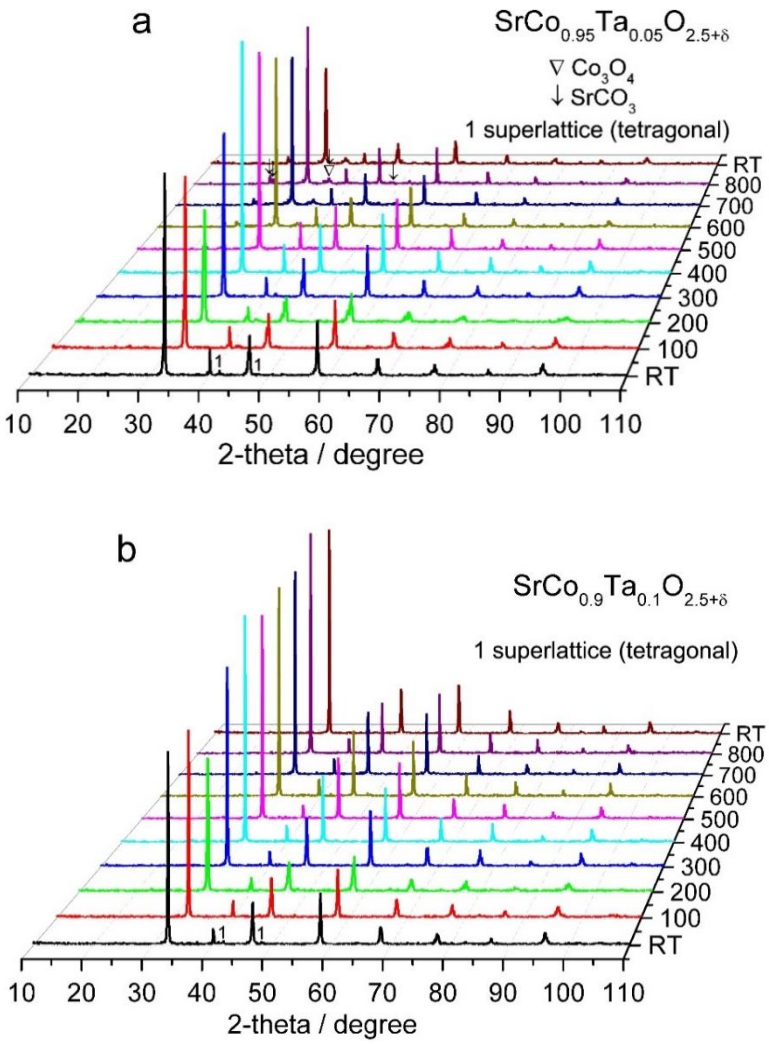

Figure 4.3 HT-XRD patterns of (a) SCT05 and (b) SCT10.

The above findings are also confirmed by *in-situ* ND. Figure 4.4 shows the ND Rietveld refinement profiles of SCT10 (note: SCT05 was not measured due to lack of interest) as a function of temperature; the corresponding structural parameters refined as well as reliable factors are given in Table 4.2. The results show that all ND patterns can be well indexed by a simple primitive cubic structure (SG: Pm-3m) with reasonable R_{wp} and R_p values; this observation is consistent with the HT-XRD results. In addition, with increasing temperature the oxygen lattice experiences a decrease in occupancy, inferring

loss of oxygen occurred as also confirmed by later TGA results. Based on the HT-XRD and ND data, the primitive cubic-structured SCT10 was selected for further electrical and electrochemical evaluations to explore its potential as a competent bifunctional oxygen electrode.

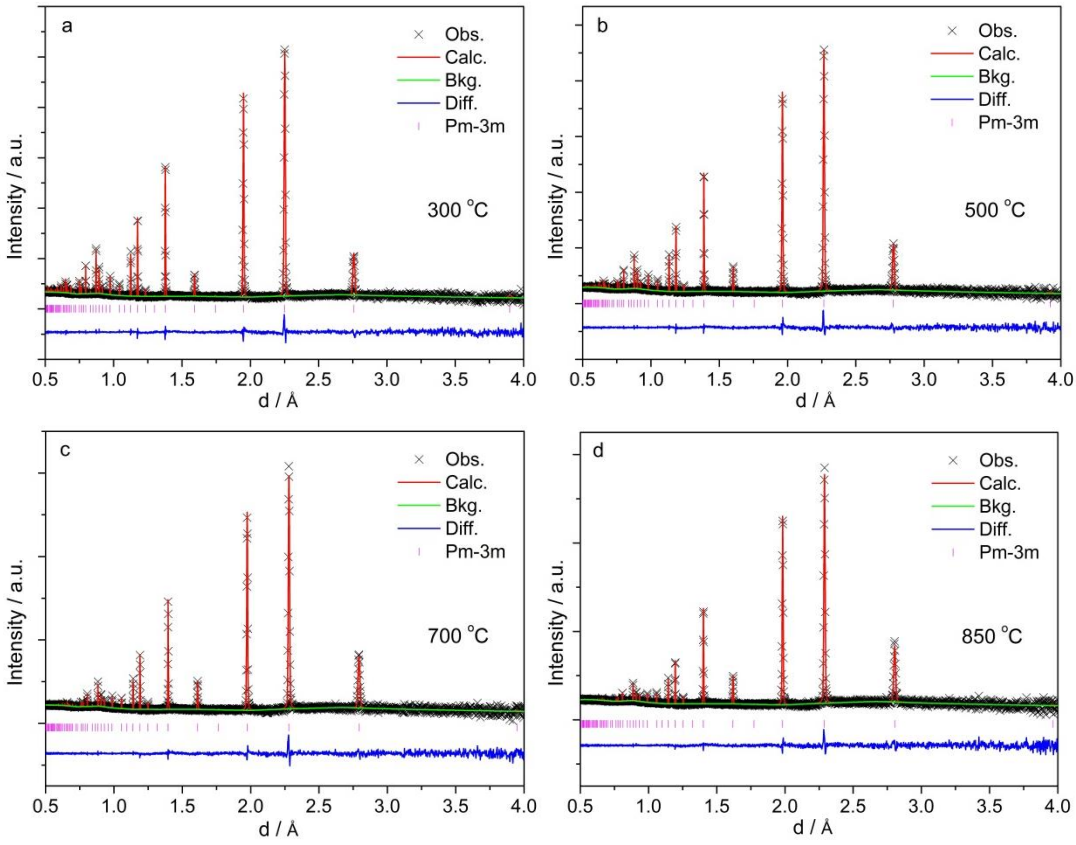

Figure 4.4 ND Rietveld refinement profiles of SCT10 at elevated temperatures in air.

Table 4.2 Unit-cell parameters and reliability factors of SCT10 derived from ND.

Parameters	**300 °C**	**500 °C**	**700 °C**	**850 °C**
Space Group	Pm-3m	Pm-3m	Pm-3m	Pm-3m
a (Å)	3.89852(3)	3.92387(4)	3.94822(7)	3.96506(6)
V (Å^3)	59.252(1)	60.415(2)	61.546(3)	62.337(3)
	Sr 1*b* (1/2, 1/2, 1/2)			
100×U_{iso} (Å^2)	1.55(3)	2.19(4)	2.91(5)	3.55(6)

f_{occ}*	1	1	1	1
	Co/Ta 1*a* (0, 0, 0)			
$100\times U_{iso}$ (Å^2)	0.84(4)	1.37(5)	2.00(7)	2.47(8)
f_{occ}*	0.9/0.1	0.9/0.1	0.9/0.1	0.9/0.1
	O 3*d* (1/2, 0, 0)			
$100\times U_{eqv}$ (Å^2)[a]	2.30	3.23	4.40	5.26
$100\times U_{11}$ (Å^2)	1.24(6)	1.77(7)	2.66(9)	3.48(12)
$100\times U_{22}=U_{33}$ (Å^2)	2.83(4)	3.95(5)	5.26(6)	6.15(8)
f_{occ}	0.895(5)	0.873(5)	0.852(6)	0.838(6)
	Reliability factors			
R_{wp} (%)	3.21	3.28	3.11	2.91
R_p (%)	6.31	6.75	6.88	6.49
χ^2	2.415	1.874	1.641	1.549

* Fixed; [a] Anisotropic thermal displacement factors *U12* = *U13* = *U23* = 0.

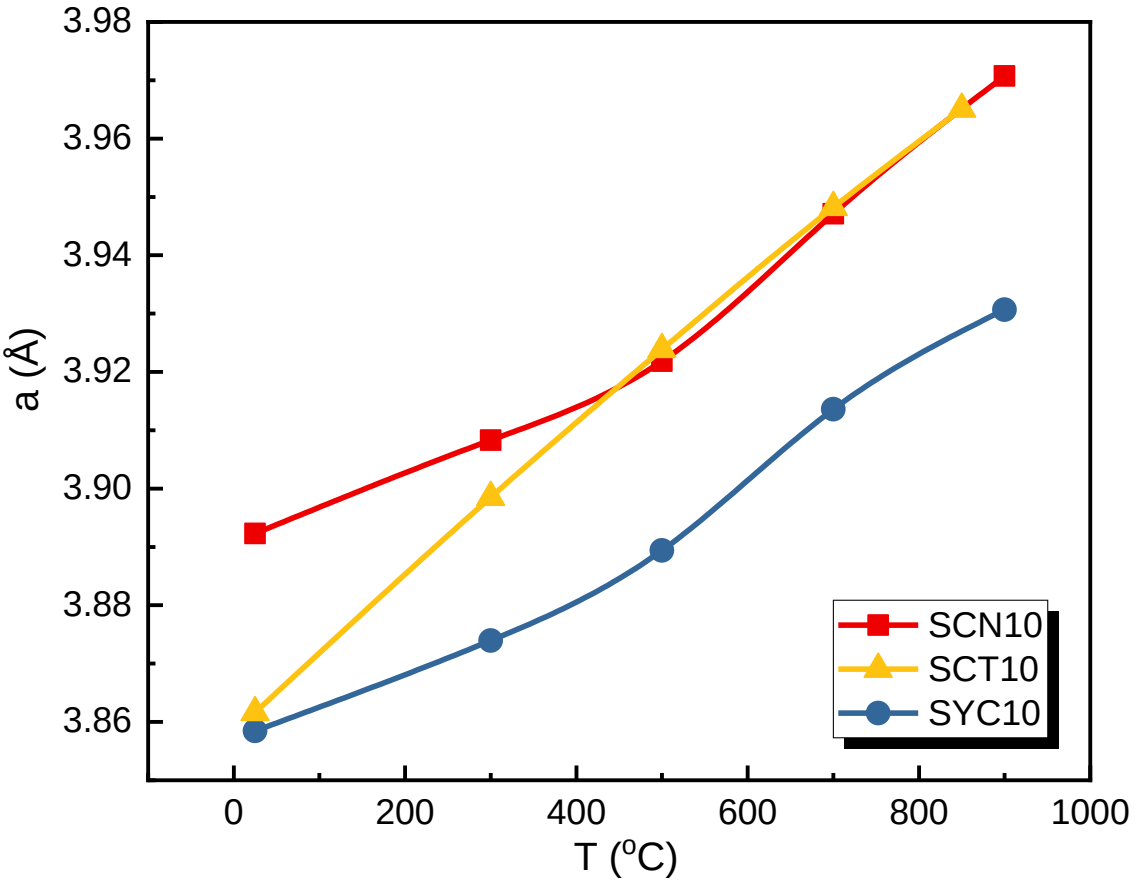

Figure 4.5 Lattice parameters of SCN10, SCT10 and SYC10 from ND.

The lattice parameters of SCT10 are also compared with SYC10 in chapter 2 and SCN10 in chapter 3. The lattice parameters of SCN10 at RT and 300 ºC (tetragonal), and SYC10 are normalized to the cubic structure for easier comparison. As seen from Figure 4.5, SCN10 has almost identical lattice sizes with SCT10 in the temperature region of cubic structure, which is consistent with the identical radius of Nb^{5+} and Ta^{5+}. At RT and 300 ºC, the lattice sizes of SCN10 are larger than SCT10, arising from its tetragonal distortion. The lattice parameters of SYC10 are much smaller than those of SCN10 or SCT10, consistent with the radius (R) of those doping and host ions ($R_{Y3+} > R_{Sr2+}$, R_{Nb5+}, $R_{Ta5+} > R_{Co3+}$)

- 4.3.3 Thermal stability

The thermal stability of SCT samples in air was also investigated by TGA, the results of which are shown in Figure 4.6. Both SCT05 and SCT10 samples exhibit similar trending, *i.e.* 1) a gradual weight loss below 250 ºC; 2) a weight gain within 250 - 400 ºC and 3) a weight loss at > 400 ºC. The initial weight loss is likely associated with the removal of adsorbed species such as H_2O and CO_2 from ambient atmosphere after synthesis. The weight gain started at ~250 ºC is related to O_2 incorporation into oxygen vacancies accompanied by oxidizing Co ions to produce electron holes. As the temperature increases further to >400 ºC, the Co-O bonds start to break, releasing oxygen (including gained and the original lattice oxygen). It is interesting to note that there is a steeper weight loss at ≥600 ºC for SCT05 than SCT10. Combining with HT-XRD data shown in Figure 4.3, it is reasonable to postulate that this accelerated weight loss is associated with the phase decomposition into SrO and Co_3O_4 via

$$SrCo_{0.95}Ta_{0.05}O_{3-\delta} = Sr_{1-x}Co_{0.95-y}Ta_{0.05}O_{3-\delta'} + xSrO + \frac{y}{3}Co_3O_4 + zO_2 \uparrow \qquad (4\text{-}3)$$

The slowdown of weight loss above 700 °C could be associated with a further loss of lattice oxygen in $Sr_{1-x}Co_{0.95-y}Ta_{0.05}O_{3-\delta'}$, ultimately leading to the formation of $Sr_2Co_2O_5$. Note that no $SrCO_3$ could form under the TGA condition since a CO_2-free zero-grade air was used for the measurement. The net weight loss after SCT05 was cooled down to RT is also an indicative of the permanent loss of oxygen due to phase decomposition. In comparison, the SCT10 sample shows a smooth monotonic weight loss from 400 to 900 °C, reflecting a gradual loss of lattice oxygen without new phase formation. Upon cooling, the sample can absorb extra oxygen to yield a net weight gain at RT. This behavior indicates a good reversibility of the oxygen intake/loss process for the SCT10 sample.

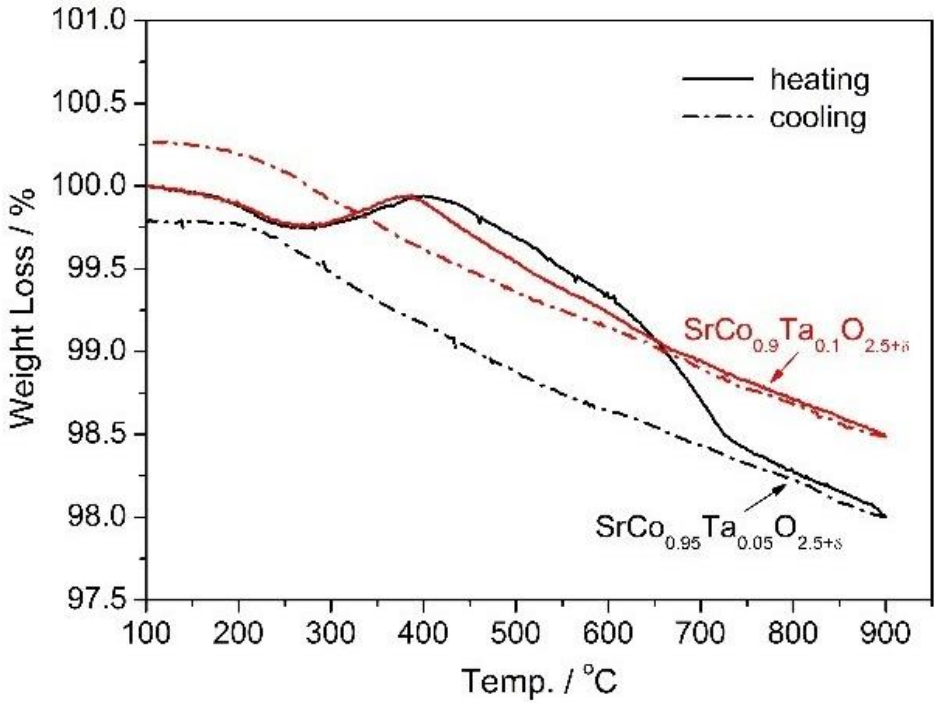

Figure 4.6 TGA profiles of SCT05 and SCT10 measured in air.

- 4.3.4 Oxygen stoichiometry (3-δ) and oxidation state (z) of Co-ions vs temperature

To determine the oxygen stoichiometry (3-δ) and oxidation state (z) of Co-ions as a function of temperature in single-phase SCT10, two methods have been used: TGA and ND. To do so, the initial oxygen stoichiometry (3-δ_o) should be first determined. We, therefore, ran a separate TGA experiment with full reduction of SCT10 by 5%H_2-N_2, the results of which are shown in Figure 4.7 (a). A total weight loss of 12.09% was found, which is equivalent to the initial oxygen content 3-δ_o=2.73 calculated by the following reduction reaction:

$$SrCo_{0.9}Ta_{0.1}O_{3-\delta} + (1.8-\delta)H_2 \rightarrow 0.9SrO + 0.9Co + 0.1SrTaO_3 + (1.8-\delta)H_2O \quad (4\text{-}4)$$

This value is close to 2.70 determined by iodine titration. By combining this initial oxygen stoichiometry (3-δ_o) with the TGA profiles shown in Figure 4.7 (b) yields the variation of 3-δ and z with T; the results are shown in Figure 4.8, where the ND-derived 3-δ and z are also plotted for comparison. Overall, the ND-derived 3-δ and z are very close to those derived from TGA. Within the margin of errors, the results generated by the two independent methods are consistent and thus deemed reliable.

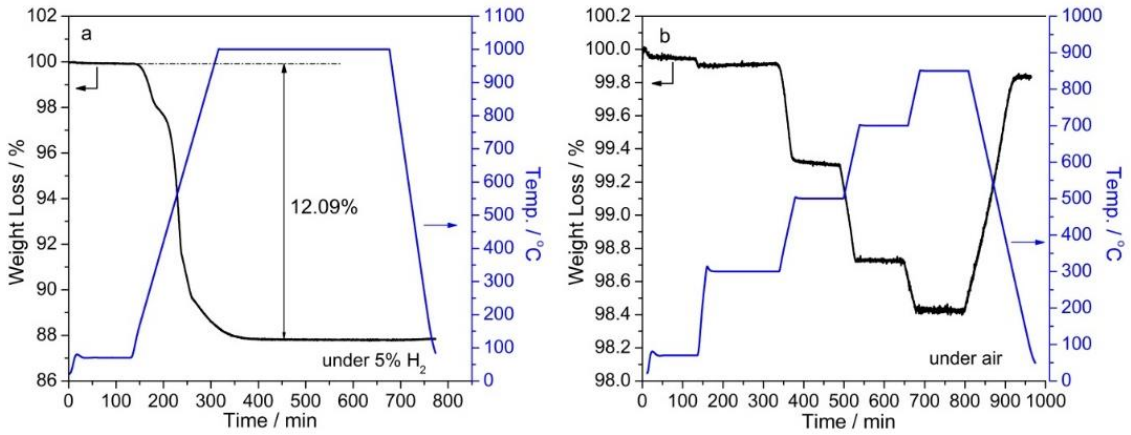

Figure 4.7 TGA profiles measured in (a) 5% H_2-N_2; (b) air.

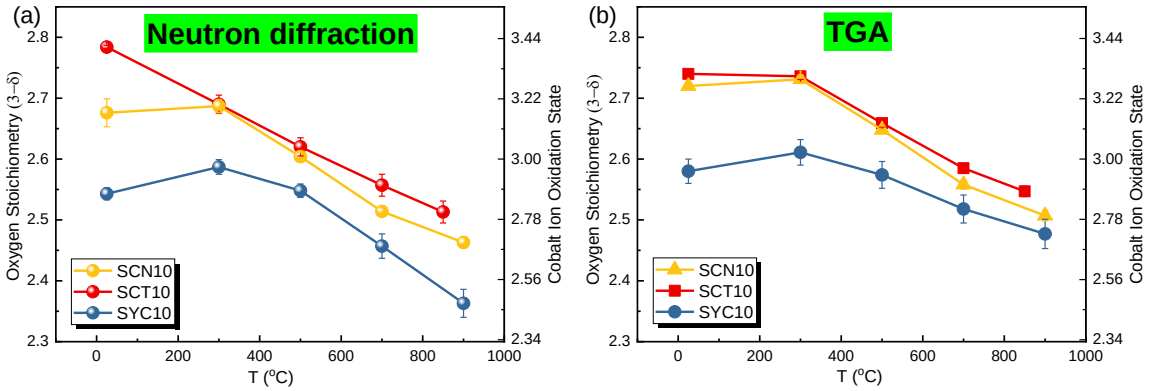

Figure 4.8 Comparison of oxygen stoichiometry and Co-ion oxidation-state *vs* temperatures determined by (a) ND and (b) TGA, for SCN10 and SCT10.

The values of SYC10 and SCN10 are also plotted in figure 4.8. The values of SCN10 are found slightly lower than SCT10, while those for SYC10 are much lower than the other two at the same temperature. To evaluate the bonding strengths of Nb-O, Ta-O and Y-O in the SCO structure, we applied the Average Bonding Energy (ABE) theory to calculate the A-O and B-O bonding energies in perovskite ABO_3 using the following equations[136, 140]:

$$\mathrm{ABE}(\mathrm{A-O}) = \frac{1}{12m}\left(\Delta_f H^o_{A_mO_n} - m\Delta H^o_A - \frac{n}{2}D_{O_2}\right) \tag{4-5}$$

$$\mathrm{ABE}(\mathrm{B-O}) = \frac{1}{6m'}\left(\Delta_f H^o_{B_{m'}O_{n'}} - m'\Delta H^o_B - \frac{n'}{2}D_{O_2}\right) \tag{4-6}$$

where $\Delta_f H^o_{A_mO_n}$ and $\Delta_f H^o_{B_{m'}O_{n'}}$ are the standard heats of formation for A_mO_n and $B_{m'}O_{n'}$ oxides, respectively; ΔH^o_A and ΔH^o_B are the standard sublimation heats for A and B metals, respectively; D_{O_2} is the dissociation energy of oxygen (500.2 kJ mol^{-1})[136]. The ABEs of Sr-O and Co-O were also calculated; the results are shown in Table 4.3. The ABE of Ta-O is the most negative, followed by Nb-O and Y-O. Hence, the fundamental reason of SCT10's

higher oxygen stoichiometry is the stronger Ta-O bond than Nb-O bond or Y-O bond as listed in Table 4.3.

Table 4.3 Average Bonding Energy of Metal-Oxygen in the SCO structure

Cation	ΔH_B^o/ kJ·mol^{-1}	Oxide	$\Delta_f H^o_{B_{m'}O_{n'}}$/ kJ·mol^{-1}	ABE (B-O)/ kJ·mol^{-1}
Co^{2+}	424.7	CoO	-237.9	-152.1
$Co^{2+/3+}$	-	Co_3O_4	-891.0	-175.9
Sr^{2+}	164.4	SrO	-592	-69.6
Nb^{5+}	725.9	Nb_2O_5	-1899.5	-383.5
Ta^{5+}	782.0	Ta_2O_5	-2046.0	-405.0
Y^{3+}	421.3	Y_2O_3	-1905.3	-145.8

Thermal expansion coefficient

The thermal expansions of SCT05 and SCT10 *vs* temperature are shown in Figure 4.9 over a temperature range of 50-900 ºC. Both samples show a distinctive increase in slope at ~500 ºC. It is reasonable to believe that the increased slope above 500 ºC is associated with the loss of lattice oxygen. A close look into the SCT05 curve reveals that it has a slightly higher thermal expansion coefficient (TEC) than SCT10, which makes sense given the fact that SCT05 loses more oxygen than SCT10 due to its lower thermal stability. The measured TEC values are similar to the reported ones for other B-site doped $SrCoO_{3-\delta}$ samples.[56, 141] It needs to be pointed out that both SCT samples have a much higher TEC than the electrolyte in a SOFC. Therefore, to use SCT as an oxygen electrode in practical SOFCs, it must be utilized in the form of nanoparticles supported on a TEC-compatible scaffold. This is also the reason this study did not attempt to use screen-printed bulk SCT as a cathode in real SOFC testing because of its impracticality.

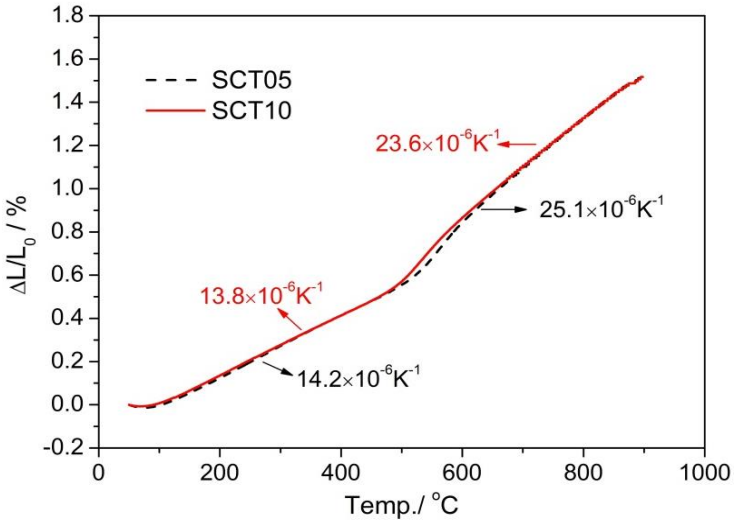

Figure 4.9 Thermal expansions of SCT05 and SCT10 *vs* temperature.

4.4 Conclusions

In summary, SCT10 exhibits a pure primitive cubic structure at T≥200 ºC and better thermal stability than SCT05. SCT10 maintains a primitive cubic structure up to 800 ºC without any impurity phase. Compared with the values of SCN10 in chapter 3, SCT10 has almost identical lattice sizes in SOFC working temperature range. The stronger Ta-O bond than Nb-O bond renders SCT10 higher oxygen stoichiometry and Co-ion oxidation states. Both SCT samples have a much higher TECs than the electrolytes, which make them impractical to use in a bulk form in SOFC.

CHAPTER 5

ELECTROCHEMICAL AND TRANSPORT PROPERTIES OF SCN10 AND SCT10

5.1 Introduction

Mixed ionic and electronic conductors (MIECs) are an important class of functional materials for oxygen separation and electrocatalysis. The current MIECs research is focused on searching for new materials with high oxygen flux and chemical stability, [142-147] few examples of which are $Sr(CoFe)O_{3-\delta}$ [148], $(LaSr)(CoFe)O_{3-\delta}$ [149-150], $(BaSr)(CoFe)O_{3-\delta}$ [145, 151], etc. These perovskite-structured MIECs generally have a high oxygen flux, but poor chemical stability, particularly in CO_2- and H_2O-contaning atmospheres.[152-154] Gaining the chemical stability of an MIEC is always at the cost of its oxygen flux, as demonstrated in the development of dual-phase MIECs.[155-156]

On the other hand, fundamental understanding of oxygen transport processes in MIECs through mathematical modeling have also drawn interests.[157-161] A straightforward and generalized transport model for oxygen permeation through a MIEC consists of surface gas/oxygen-lattice exchange and bulk oxide-ion diffusion. For the bulk diffusion, oxygen vacancies ($V_O^{\cdot\cdot}$) and holes moving in the opposite direction are considered the mobile charge carriers.[162-163] The driving force for the oxygen transport is the gradient of electrochemical

potential of oxygen across the MIEC.[164-165] The permeated oxygen flux J_{O_2} via bulk diffusion is quantified by the classical Wagner equation: [165]

$$J_{O_2} = -\frac{RT}{4^2F^2L}\int_{lnP_{O_2}^f}^{lnP_{O_2}^s}\frac{\sigma_e\sigma_i}{\sigma_e+\sigma_i}dlnP_{O_2} \quad (5\text{-}1)$$

where R is the gas constant; T is the temperature; F is the Faraday constant; L is the membrane thickness; σ_e and σ_i are electronic and ionic conductivity, respectively; $P_{O_2}^s$ and $P_{O_2}^f$ are partial pressures of oxygen at sweeping and feeding surfaces, respectively.

For an electron-conduction predominated MIEC ($\sigma_e >> \sigma_i$), which is true for most MIECs, eq. (5-1) can be simplified into

$$J_{O_2} = -\frac{RT}{4^2F^2L}\int_{lnP_{O_2}^f}^{lnP_{O_2}^s}\sigma_i dlnP_{O_2} \quad (5\text{-}2)$$

Therefore, to theoretically assess the oxygen flux of an MIEC, the knowledge of σ_i-P_{O_2} relationship is needed. Hassel and Bouwmeester, et al. indirectly obtained the σ_i-P_{O_2} relationship of (LaSr)$BO_{3-\delta}$ (B=Cr, Fe, Co or Mn) from oxygen nonstoichiometric (3-δ) vs P_{O_2} dependence and a point defect model, [157] from which an analytical expression of J_{O_2} vs P_{O_2} was obtained. However, the surface oxygen exchange was not considered in their model. Lin et al. developed a permeation model for MIECs in 1994 which considered both the bulk diffusion and surface oxygen exchange for the first time.[166] They treated the surface gas/oxygen-lattice exchange process as

$$\frac{1}{2}O_2 + V_O^{\cdot\cdot} \underset{k_2}{\overset{k_1}{\rightleftarrows}} O_O^{\times} + 2h^{\cdot} \quad (5\text{-}3)$$

where $O_O^{\times}$ represents regular lattice oxygen; $h^{\cdot}$ denotes electron holes; k_1 and k_2 are rate constants of forward and backward reactions, respectively. The forward and backward reactions are assumed to take place at the feeding and sweeping surfaces, respectively. The bulk diffusion was modeled by one-dimensional Fick's first law. Xu and Thomson further simplified Lin's model and applied it to $(La_{0.6}Sr_{0.4})(Co_{0.2}Fe_{0.8})O_{3-\delta}$.[158] The final analytical expression for J_{O_2} vs P_{O_2} contains both chemical diffusion coefficient of $V_O^{\cdot\cdot}$ ($\widetilde{D}_{V_O^{\cdot\cdot}}$) and surface exchange reaction rate constants (k_1 and k_2) as the fitting parameters. In another phenomenological model, Zhu *et al.* described the oxygen permeation process consisting of two interfacial oxygen-exchange zones at the feeding and sweeping surfaces and one bulk-diffusion zone.[161, 167-168] Area-specific resistances (ASRs) were separately introduced for each zone and obtained by fitting both $P_{O_2}^f$ - J_{O_2} dependence at a fixed $P_{O_2}^s$ and $P_{O_2}^s$- J_{O_2} relationship at a fixed $P_{O_2}^f$. The surface exchange coefficients and self-diffusion coefficient of $V_O^{\cdot\cdot}$ were then calculated from ASRs.[167]

Recently, $SrCo_{0.9}Nb_{0.1}O_{3-\delta}$ (SCN10) and $SrCo_{0.9}Ta_{0.1}O_{3-\delta}$ (SCT10) have been reported with high oxygen permeability and good chemical stability for > 200 days, demonstrating the potential for practical applications.[57, 114] Jin *et al.* developed a defect chemistry model simulating the transport of mixed conduction in SCN10 and SCT10 and derived an analytic expression for $\sigma = \sigma(T, P_{O_2})$.[169-170] With the experimentally determined $\sigma = \sigma(T, P_{O_2})$, the equilibrium constants of defect reactions, concentrations of charge carriers and thermodynamic factor were obtained.

In this chapter, a combined experimental J_{O_2} vs P_{O_2} data measured by oxygen permeation and a diffusion model is presented to obtain transport properties such as ionic conductivity, chemical diffusivity and surface exchange rate constant of oxygen in mixed conducting SCN10 and SCT10. The oxygen permeation methodology is adopted to derive oxygen transport properties of MIECs because it provides the best accuracy and reliability among all methods explored (such as blocking electrode and electrical conductivity relaxation methods).[171] Several key performances of SYC10, SCN10 and SCT10 are also compared and correlated with their structural properties through molecular orbital energy analysis. The stability tests show that the SCT10 is the best catalyst among these three materials, consistent with the average bonding energy analysis in chapter 4.

5.2 Oxygen permeation model

The SCN10 and SCT10 have been known to be a *p*-type electronic conductor with oxygen vacancies as a minor charge carrier.[58, 172] Within the P_{O_2} range studied, free electron (e^-) conduction is negligible.[169-170] Figure 5.1 shows the oxygen permeation processes for a *p*-type MIEC membrane. At the feeding side (high P_{O_2}), the net effects of surface exchange reaction are O_2 incorporation into the membrane by reacting with $V_O^{\cdot\cdot}$ and producing $h^{\cdot}$ and $O_O^{\times}$:

$$\frac{1}{2}O_2 + V_O^{\cdot\cdot} \rightarrow O_O^{\times} + 2h^{\cdot} \tag{5-4}$$

The surface exchange process at the sweeping side (low P_{O_2}) consumes $h^{\cdot}$ and release $V_O^{\cdot\cdot}$, which is the opposite to that at the feeding side:

$$O_O^{\times} + 2h^{\cdot} \rightarrow \frac{1}{2}O_2 + V_O^{\cdot\cdot} \tag{5-5}$$

To maintain local charge neutrality, the transport of $V_O^{\cdot\cdot}$ is in the opposite direction of concomitant flux of $h^{\cdot}$ as shown by

$$V_O^{\cdot\cdot}\left(sweeping\right) \rightarrow V_O^{\cdot\cdot}\left(feeding\right) \tag{5-6}$$

$$2h^{\cdot}\left(feeding\right) \rightarrow 2h^{\cdot}\left(sweeping\right) \tag{5-7}$$

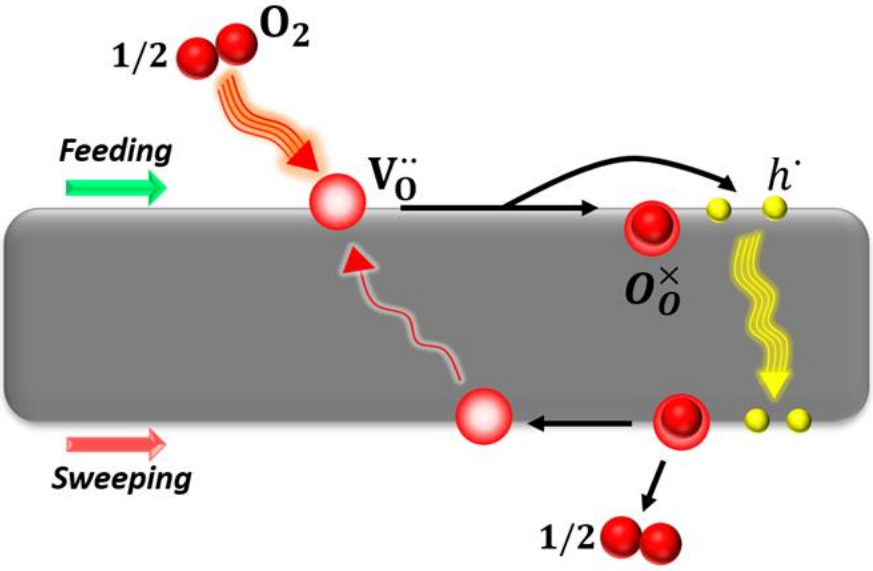

Figure 5.1 Schematic of oxygen permeation through a *p*-type MIEC membrane.

Since the electron hole conductivity is much higher than that of $V_O^{\cdot\cdot}$ in the bulk, the oxygen permeation flux $J_{V_O^{\cdot\cdot}}$ through the bulk is mainly limited by the $V_O^{\cdot\cdot}$ diffusion driven by electrochemical potential gradient ($\nabla \eta_{V_O^{\cdot\cdot}}$):

$$J_{V_O^{\cdot\cdot}}\left[mol\,cm^{-2}\,s^{-1}\right] = -\frac{\sigma_{V_O^{\cdot\cdot}}}{z_{V_O^{\cdot\cdot}}^2 F^2}\nabla \eta_{V_O^{\cdot\cdot}} \tag{5-8}$$

where $z_{V_O^{\cdot\cdot}}$ is the charge of $V_O^{\cdot\cdot}$; $\sigma_{V_O^{\cdot\cdot}}$ [$S\ cm^{-1}$] is the conductivity of $V_O^{\cdot\cdot}$, which is represented by σ_i since $V_O^{\cdot\cdot}$ is the only ionic charge carrier; F [$C\ mol^{-1}$] is Faraday constant. The electrochemical potential gradient of oxygen $\nabla \eta_{V_O^{\cdot\cdot}}$ [$V\ cm^{-1}$] consist of chemical potential gradient ($\nabla \mu_{V_O^{\cdot\cdot}}$) and electrostatic potential gradient ($\nabla \phi, V\ cm^{-1}$)

$$\nabla \eta_{V_O^{\cdot\cdot}} = \nabla \mu_{V_O^{\cdot\cdot}} + z_{V_O^{\cdot\cdot}} F \nabla \phi \tag{5-9}$$

The concentration of $h^{\cdot}$ is assumed to be uniform across the membrane due to the high electronic conductivity. Hence, no $\nabla \phi$ is established across the membrane. Eq. (5-8) is then simplified into

$$J_{V_O^{\cdot\cdot}} = -\frac{\sigma_{V_O^{\cdot\cdot}}}{z_{V_O^{\cdot\cdot}}^2 F^2} \nabla \mu_{V_O^{\cdot\cdot}} \tag{5-10}$$

$$\mu_{V_O^{\cdot\cdot}} = \mu_{V_O^{\cdot\cdot}}^o + RTlna_{V_O^{\cdot\cdot}} \tag{5-11}$$

$a_{V_O^{\cdot\cdot}}$ is the activity of $V_O^{\cdot\cdot}$ (equal to its concentration).

According to Nernst-Einstein equation[165],

$$\sigma_{V_O^{\cdot\cdot}} = \frac{z_{V_O^{\cdot\cdot}}^2 F^2 c_{V_O^{\cdot\cdot}} D_{V_O^{\cdot\cdot}}}{RT} \tag{5-12}$$

where $D_{V_O^{\cdot\cdot}}$ [$cm^2\ s^{-1}$] is the diffusion coefficient of $V_O^{\cdot\cdot}$. $c_{V_O^{\cdot\cdot}}$ [$mol\ cm^{-3}$] is the concentration of $V_O^{\cdot\cdot}$. Combining eq. (5-10), (5-11) and (5-12),

$$J_{V_O^{\cdot\cdot}} = -\tilde{D}_{V_O^{\cdot\cdot}} \frac{dc_{V_O^{\cdot\cdot}}}{dx} \tag{5-13}$$

$\widetilde{D}_{V_O^{\cdot\cdot}}$ [$cm^2\ s^{-1}$] is the chemical diffusion coefficient of $V_O^{\cdot\cdot}$. A detailed derivation is given below.

$$J_{V_O^{\cdot\cdot}} = -\frac{\sigma_{V_O^{\cdot\cdot}}}{z_{V_O^{\cdot\cdot}}^2 F^2}\nabla\mu_{V_O^{\cdot\cdot}}$$

$$= -\frac{\sigma_{V_O^{\cdot\cdot}}}{z_{V_O^{\cdot\cdot}}^2 F^2} RT\nabla ln a_{V_O^{\cdot\cdot}} \quad [\text{Note: } \mu_{V_O^{\cdot\cdot}} = \mu_{V_O^{\cdot\cdot}}^o + RTln a_{V_O^{\cdot\cdot}}]$$

$$= -\frac{\frac{z_{V_O^{\cdot\cdot}}^2 F^2 c_{V_O^{\cdot\cdot}} D_{V_O^{\cdot\cdot}}}{RT}}{z_{V_O^{\cdot\cdot}}^2 F^2} RT\nabla a_{V_O^{\cdot\cdot}} \quad [\text{Note: } \sigma_{V_O^{\cdot\cdot}} = \frac{z_{V_O^{\cdot\cdot}}^2 F^2 c_{V_O^{\cdot\cdot}} D_{V_O^{\cdot\cdot}}}{RT}]$$

$$= -c_{V_O^{\cdot\cdot}} D_{V_O^{\cdot\cdot}} \frac{\partial ln a_{V_O^{\cdot\cdot}}}{\partial ln c_{V_O^{\cdot\cdot}}} \nabla ln c_{V_O^{\cdot\cdot}}$$

$$= -c_{V_O^{\cdot\cdot}} D_{V_O^{\cdot\cdot}} \frac{\partial ln a_{V_O^{\cdot\cdot}}}{\partial ln c_{V_O^{\cdot\cdot}}} \left(\frac{\partial ln c_{V_O^{\cdot\cdot}}}{\partial x}\boldsymbol{i} + \frac{\partial ln c_{V_O^{\cdot\cdot}}}{\partial y}\boldsymbol{j} + \frac{\partial ln c_{V_O^{\cdot\cdot}}}{\partial z}\boldsymbol{k} \right)$$ [Note: $\boldsymbol{i}$, $\boldsymbol{j}$ and $\boldsymbol{k}$ are standard unit vector in the direction of the x, y and z coordinates, respectively.]

$$= -c_{V_O^{\cdot\cdot}} D_{V_O^{\cdot\cdot}} \frac{\partial ln a_{V_O^{\cdot\cdot}}}{\partial ln c_{V_O^{\cdot\cdot}}} \frac{\partial ln c_{V_O^{\cdot\cdot}}}{\partial x}\boldsymbol{i}$$ [Note: x coordinate corresponds to the pellet thickness direction. The diffusion along other directions is omitted because the thickness is very small compared to the diameters, making it one dimensional.]

$$= -c_{V_O^{\cdot\cdot}} D_{V_O^{\cdot\cdot}} \frac{\partial ln a_{V_O^{\cdot\cdot}}}{\partial ln c_{V_O^{\cdot\cdot}}} \frac{\frac{1}{c_{V_O^{\cdot\cdot}}}\partial c_{V_O^{\cdot\cdot}}}{\partial x}\boldsymbol{i}$$

$$= -D_{V_O^{\cdot\cdot}} \frac{\partial ln a_{V_O^{\cdot\cdot}}}{\partial ln c_{V_O^{\cdot\cdot}}} \frac{\partial c_{V_O^{\cdot\cdot}}}{\partial x}$$ [Note: the unit vector $\boldsymbol{i}$ is ignored.]

$$= -\tilde{D}_{V_O^{\cdot\cdot}} \frac{\partial c_{V_O^{\cdot\cdot}}}{\partial x} \text{ [Note: } \tilde{D}_{V_O^{\cdot\cdot}} = D_{V_O^{\cdot\cdot}} \frac{\partial ln a_{V_O^{\cdot\cdot}}}{\partial ln c_{V_O^{\cdot\cdot}}} \text{]}$$

As shown in eq. (5-13), the oxygen permeation through a MIEC membrane bulk follows the one-dimension Fick's first law.

The boundary conditions for solving eq. (13) are provided by the oxygen flux at both feeding and sweeping sides [157, 173-174]

At the feeding surface: $$J_{V_O^{\cdot\cdot}} = k_{s,f}\left(c_{V_O^{\cdot\cdot},f} - c^{eq}_{V_O^{\cdot\cdot},f}\right) \quad (5\text{-}14)$$

At the sweeping surface: $$J_{V_O^{\cdot\cdot}} = k_{s,s}\left(c^{eq}_{V_O^{\cdot\cdot},s} - c_{V_O^{\cdot\cdot},s}\right) \quad (5\text{-}15)$$

where k_s [cm s^{-1}] is the intrinsic rate constant of surface gas/oxygen-lattice exchange; the subscriptions *f* and *s* denote feeding and sweeping, respectively.; *eq* denotes equilibrium. Solving eq. (5-13) with the boundary conditions of (5-14) and (5-15) yields

$$J_{V_O^{\cdot\cdot}} = \frac{k_{s,f}k_{s,s}\tilde{D}_{V_O^{\cdot\cdot}}\left(c^{eq}_{V_O^{\cdot\cdot},s} - c^{eq}_{V_O^{\cdot\cdot},f}\right)}{k_{s,f}k_{s,s}L + k_{s,f}D_{V_O^{\cdot\cdot}} + k_{s,s}\tilde{D}_{V_O^{\cdot\cdot}}} \quad (5\text{-}16)$$

where L [cm] is the membrane thickness; $c^{eq}_{V_O^{\cdot\cdot}}$ is the equilibrium molar concentration of $V_O^{\cdot\cdot}$ in the bulk, which can be calculated from oxygen non-stoichiometry (δ, numerical value) for cubic structured SCN and SCT systems by

$$c^{eq}_{V_O^{\cdot\cdot}} = \frac{\delta}{N_A V_m} \quad (5\text{-}17)$$

where N_A [mol^{-1}] is Avogadro constant; V_m [cm^3] is the unit cell volume.

The oxygen non-stoichiometry (δ) are available from our previous work[169-170],

$$\delta_{SCN10} = 0.7966 - 0.00836 lnP_{O_2} - 0.52127\frac{1000}{T} - 4.60926\times10^{-4}\left(lnP_{O_2}\right)^2 + 0.09848\left(\frac{1000}{T}\right)^2 - 0.00629\frac{1000}{T}lnP_{O_2} \quad (5\text{-}18)$$

$$\delta_{SCT10} = 0.58141 - 0.02155 lnP_{O_2} - 0.14465\frac{1000}{T} - 4.20455\times10^{-4}\left(lnP_{O_2}\right)^2 - 0.07021\left(\frac{1000}{T}\right)^2 + 0.00528\frac{1000}{T}lnP_{O_2} \quad (5\text{-}19)$$

Combining eq. (5-16) & (5-17) and considering $J_{V_O^{\cdot\cdot}} = \frac{1}{2}J_{O_2}$ lead to

$$J_{O_2} = \frac{k_{s,f}k_{s,s}\tilde{D}_{V_O^{\cdot\cdot}}\left(\delta\left(\mathrm{T},P_{O_2}\right)_s - \delta\left(\mathrm{T},P_{O_2}\right)_f\right)}{2\left(k_{s,f}k_{s,s}L + k_{s,f}\tilde{D}_{V_O^{\cdot\cdot}} + k_{s,s}\tilde{D}_{V_O^{\cdot\cdot}}\right)N_A V_m} \quad (5\text{-}20)$$

With isothermal experimental J_{O_2} *vs* $P_{O_2}^s$ or $P_{O_2}^f$, the surface exchange and bulk diffusion parameters such as $k_{s,f}$, $k_{s,s}$ and $\widetilde{D}_{V_O^{\cdot\cdot}}$ can be obtained by nonlinear fitting. For materials with a much higher $k_{s,s}$ than $k_{s,f}$, $k_{s,s}$ can be omitted from eq. (5-20), yields

$$J_{O_2} = \frac{k_{s,f}\tilde{D}_{V_O^{\cdot\cdot}}\left(\delta\left(\mathrm{T},P_{O_2}\right)_s - \delta\left(\mathrm{T},P_{O_2}\right)_f\right)}{2\left(k_{s,f}L + \tilde{D}_{V_O^{\cdot\cdot}}\right)N_A V_m} \quad (5\text{-}21)$$

with only two fitting parameters $k_{s,f}$ and $\widetilde{D}_{V_O^{\cdot\cdot}}$.

5.3 Experimental and simulation methods

• 5.3.1 Membrane synthesis

The SCN10 and SCT10 were prepared by solid-state reaction method. Stoichiometry amounts of $SrCO_3$ (≥99.9%, Aldrich), Co_3O_4 (99.7%, Alfa Aesar), Nb_2O_5 (99.9%, Alfa Aesar) or Ta_2O_5 (99.85%, Alfa Aesar) were ball-milled in ethanol for 3 h. The powder was then dried and pressed into pellets. The pellets were first calcinated at 1000 ^oC and 1050 ^oC for 12 h with 3 $^oC\ min^{-1}$ heating and cooling rates, respectively, for SCN10 and SCT10. The sample was then broken up, ball-milled and dried. Buried in the same powder to ensure phase purity and homogeneity, the final membranes were sintered at 1230 ^oC for 10 h. The two surfaces of membranes were then polished with SiC sandpaper from 200 to 1000 mesh. A 10 μm surface layer with coarser SCN10 or SCT10 particles were also screen printed on the feeding side surface of each membrane to enhance the surface oxygen exchange so that J_{O_2} is high enough to be accurately measured at lower temperatures.

• 5.3.2 Oxygen permeation

A home-made system was used to evaluate the oxygen permeation flux in SCN10 and SCT10 membranes. A dense membrane was first sealed between two alumina tubes by an Ag-paste (DAD-87, Shanghai Research Institute of Synthetic Resins). The permeation cell was then heated up to 850 ^oC (at a rate of 1 $^oC\ min^{-1}$) and held for 1 h to allow proper sealing to take place. The measurement proceeded in a cooling sequence from 850-650 ^oC in a 25 ^oC interval. The equilibration time varied with temperature from 2 h at higher temperatures to 12 h at lower temperatures. The feeding gas was air with a fixed flow rate of 100 sccm (standard cubic centimeter per minute), while the sweeping gas at permeate side was an ultra-pure Ar. The $P_{O_2}^{s}$ was varied by changing the flow rate of sweeping gas

(from 10 to 100 sccm). Any detectable nitrogen was regarded as leakage from air and used to correct oxygen content measured. The concentrations of O_2 and N_2 in the permeate side were analyzed by a gas chromatographer (Agilent 490). Mass controllers (Smart-Trak 50 series) specifically calibrated for each gas under use were employed to control the gas flow rates. The final flux densities of oxygen (J_{O_2}) are calculated by:

$$J_{O_2} = \frac{C_{O_2} - C_{N_2} \times \frac{21}{79} \times (\frac{28}{32})^{0.5}}{1 - C_{O_2} - C_{N_2}} \times \frac{F_s}{A} \tag{5-22}$$

where C_{O_2} and C_{N_2} are the measured concentrations of O_2 and N_2, respectively; F_s is the flow rate of sweeping Ar gas; A is the effective area of the sample (=0.745 cm^2). Any detectable N_2 is corrected in eq. (5-22). The corrections are less than 1% of the C_{O_2} in the effluent gas.

- 5.3.3 Non-linear regression

The nonlinear regression using eq. (5-21) was carried out by Matlab LSQNONLIN with J_{O_2} at various $P_{O_2}^S$ as input data. To ensure high fidelity of the modeling results, the following sum of squares is used to ensure the best fitting with a threshold of 10^{-20}:

$$\text{Obj} = \sum_{i=0}^{n} \left(J_{O_2}^{model} - J_{O_2}^{exprimental} \right)^2 \tag{5-23}$$

where n is the number of J_{O_2} data points collected at various $P_{O_2}^S$.

- 5.3.4 Electrical conductivity measurement

The electrical conductivity (σ) of SCT samples were evaluated as a function of temperature (T) and time (t). The σ=σ(T) data were measured in air with T varying from RT to 800 ºC

in a step of 50 ºC, while σ=σ(t) were measured in air at different temperatures (500-800 ºC) for a given length of time. The phase composition of the samples after testing was also examined with XRD.

- 5.3.5 Preparation of symmetrical impedance cells

A symmetrical impedance cell under study was comprised of two identical porous SCT10 electrodes and a dense $Ge_{0.8}Gd_{0.2}O_{2-\delta}$ (GDC: 300 μm in thickness) electrolyte. To make the porous SCT10 cathode, SCT10 powders were first mixed with V-006A (Heraeus) to form a uniform ink, followed by screen-printing it on both sides of the GDC electrolyte. Then, the symmetrical cell was calcined at 1000 °C for 2 h to remove organic binder and bond SCT10 cathode to GDC. Silver paste/mesh was finally applied as a current collector to the surface of SCT cathode, followed by curing at 600 °C for 1 hour.

- 5.3.6 Electrochemical impedance spectroscopy measurement

Electrochemical impedance spectroscopy (EIS) measurements of the above symmetrical cells were performed with a Solartron 1260 Frequency Response Analyzer coupled with 1287 Electrochemical Interface. The frequency was swept from 0.01 Hz to 1 MHz.

5.4 Results and discussion

- 5.4.1 $k_{s,f}$ vs $k_{s,s}$

The surface oxygen exchange process at the feeding side is O_2 incorporation into the membrane bulk, while at the sweeping side it is O_2 evolution into the gas phase from the bulk, see Figure 5.1. The reactions happened at the surfaces of feeding or sweeping sides are equivalent to the oxygen reduction reaction (ORR) and oxygen evolution reaction (OER) at the air electrode of a solid oxide fuel cell (SOFC) and a solid oxide electrolysis

cell (SOEC), respectively. A much faster kinetics for OER have been previously reported for $SrCo_{0.9}Mo_{0.1}O_{3-\delta}$ [56] and SCT10 [172], which suggests that $k_{s,f}$ is smaller than $k_{s,s}$ for SCN10 and SCT10 membranes.

The importance of surface modification in oxygen permeation flux is first studied on a 1.35 mm thick SCN10 membrane. The J_{O_2} in this work is comparable with those reported values. [69, 114, 175] The surface morphology of the modification layer is shown in Figure 5.2 (a). The coarsened SCN10 particles are expected to increase specific surface area for oxygen exchange, thus enhancing the overall oxygen flux. However, Figure 5.2 (b) shows a very small difference in J_{O_2} at 850 °C between the pristine and surface-modified membranes, implying that surface oxygen exchange at the feeding side is not rate limiting at this temperature. This is consistent with the report by Zhang *et al*, where the oxygen bulk diffusion was found a rate limiting step at the same temperature for even a thinner SCN10 membrane (1.0 mm).[114] However, the later J_{O_2}results surface modified 2.35mm-SCN10 show that the it is not completely controlled by the bulk diffusion process. The K value of $\frac{J_1 L_1}{J_2 L_2}$ equals 0.76, less than 1. In contrast, Figure 5.2 (b) shows a more pronounced enhancement of J_{O_2} by the surface modification layer at the feeding side at 750 and 650 °C, suggesting that surface exchange at the feeding side becomes rate-limiting (smaller $k_{s,f}$ than $k_{s,s}$) at lower temperatures, which has also been observed in $La_{0.7}Sr_{0.3}CoO_{3-\delta}$ [161] or $Ba_{0.5}Sr_{0.5}Co_{0.8}Fe_{0.2}O_{3-\delta}$ [160]. In this case, eq. (5-21) is a better expression than eq. (5-20) to derive $k_{s,f}$ with improved accuracy and reliability.

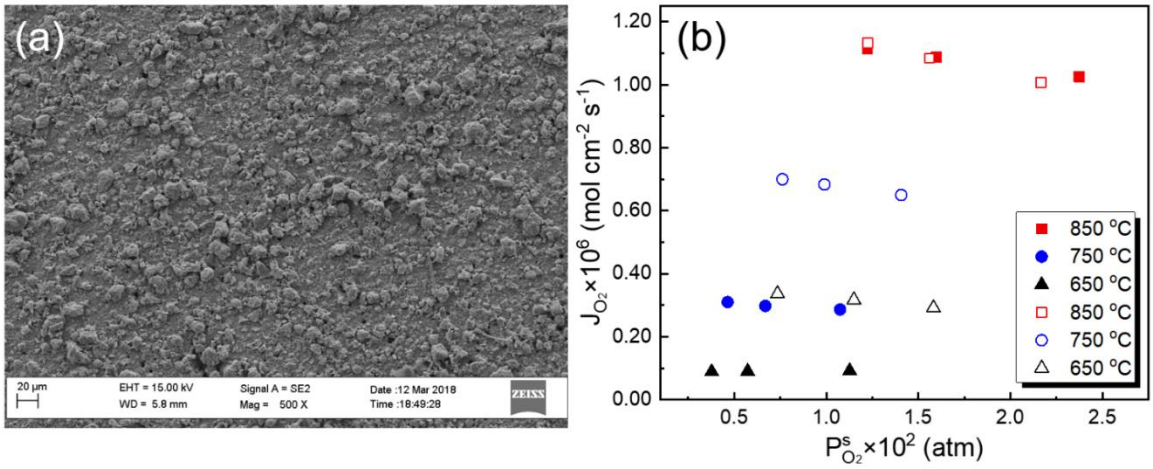

Figure 5.2 (a) Surface morphology of the surface modification layer on SCN10 membrane; (b) J_{O_2} of a 1.35mm-thick SCN10 membrane with (hollow) or without (solid) surface modification layer at the feeding side surface.

- 5.4.2 Calculated $\widetilde{D}_{V_O^{\cdot\cdot}}$ and $k_{s,f}$ vs T

Figure 5.3 (a) and (b) show the modeled and experimental $P_{O_2}^S$ vs J_{O_2} data from 650 to 850 ^oC for both 1.35 and 2.35 mm thick SCN10 membranes; a good agreement is clearly observed. The extracted $\widetilde{D}_{V_O^{\cdot\cdot}}$ and $k_{s,f}$ are further plotted in Figure 5.4 (a) and (b), respectively, as a function of temperature. Note that both intensive properties $\widetilde{D}_{V_O^{\cdot\cdot}}$ and $k_{s,f}$ obtained are nearly independent of the thickness, indirectly indicating a good fidelity of the model. The Arrhenius plot of $\log\widetilde{D}_{V_O^{\cdot\cdot}}$ and $\log k_{s,f}$ *vs* $\frac{1}{T}$ shows a linear relationship, confirming that both surface exchange and bulk diffusion of oxygen are a thermally activated process. Our previous studies of SCN10 indeed revealed the same crystal structure and constant activation energy (E_a) for ORR process within the same temperature range.[58, 97]

For comparison, J_{O_2} vs $P_{O_2}^{S}$ data obtained from a surface modified 2.35 mm-SCT10 membrane were also modeled. Again, a good agreement between the modeled and experimental J_{O_2} vs $P_{O_2}^{S}$ is also observed in Figure 5.3 (c). The obtained $\widetilde{D}_{V_O^{\cdot\cdot}}$ and $k_{s,f}$ shown in Figure 5.4 and Table 5.1 are both lower than those of SCN10, while E_a of $\widetilde{D}_{V_O^{\cdot\cdot}}$ is higher than SCN10, 0.85 vs 0.79 eV; this implies that the migration of $V_O^{\cdot\cdot}$ is more difficult in SCT10 than in SCN10.

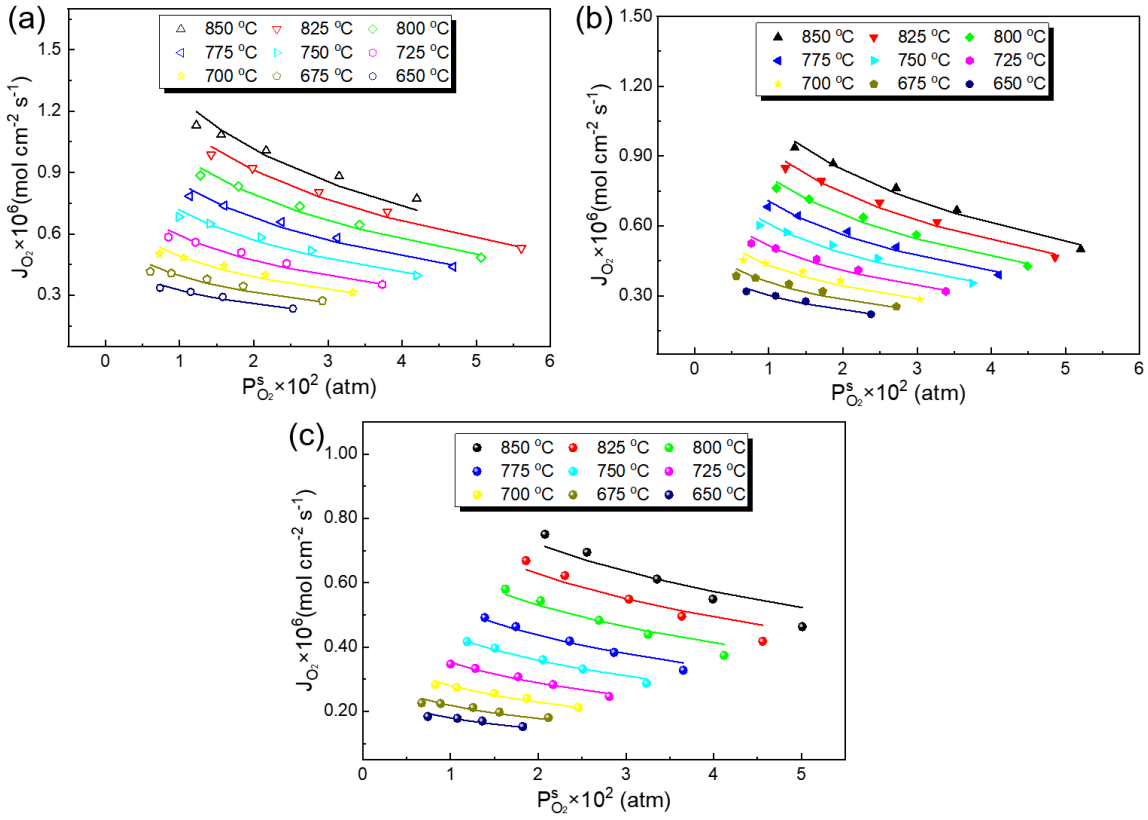

Figure 5.3 Modeling (solid lines) and experimental (dots) J_{O_2} vs $P_{O_2}^{S}$. (a) 1.35 mm-SCN10; (b) 2.35 mm-SCN10 and (c) 2.35 mm-SCT10 in thickness.

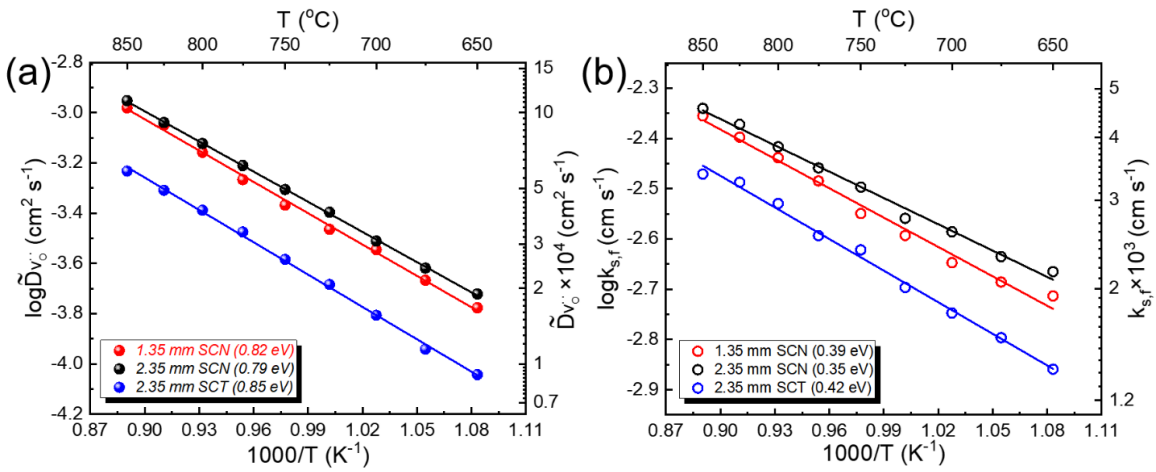

Figure 5.4 The calculated (a) $\widetilde{D}_{V_O^{\cdot\cdot}}$ and (b) $k_{s,f}$ for SCN10 and SCT10 from 650 to 850 °C.

Table 5.1 The obtained T-dependent $\widetilde{D}_{V_O^{\cdot\cdot}}$ and $k_{s,f}$ for SCN10 and SCT10.

Parameter	**Sample**	**Analytical Expression**
$\widetilde{D}_{V_O^{\cdot\cdot}}$	SCN10	$(4.06 \pm 0.39) \times exp(-\frac{0.79 \pm 0.005\ eV}{RT})$
	SCT10	$(4.01 \pm 0.67) \times exp(-\frac{0.85 \pm 0.013\ eV}{RT})$
$k_{s,f}$	SCN10	$(0.16 \pm 0.02) \times exp(-\frac{0.35 \pm 0.011\ eV}{RT})$
	SCT10	$(0.26 \pm 0.04) \times exp(-\frac{0.42 \pm 0.012\ eV}{RT})$

Our previous works have shown that SCN10 and SCT10 have the same cubic perovskite structure (#221, Pm-3m) with almost identical lattice sizes as shown in Figure 5.3a.[97, 172] When $V_O^{\cdot\cdot}$ migrates to an adjacent position, the O-2p band energy at the original position is decreased with respect to the metal-3d states along with an increase of Fermi energy level. Hence, the motional energies correlate with the number of electrons interchanged between the Fermi level and O-2p band level.[48-50] A qualitative molecular

orbital (MO) energy analysis of the $(CoNb)O_6$ and $(CoTa)O_6$ octahedra is schematically shown in Figure 5.5.

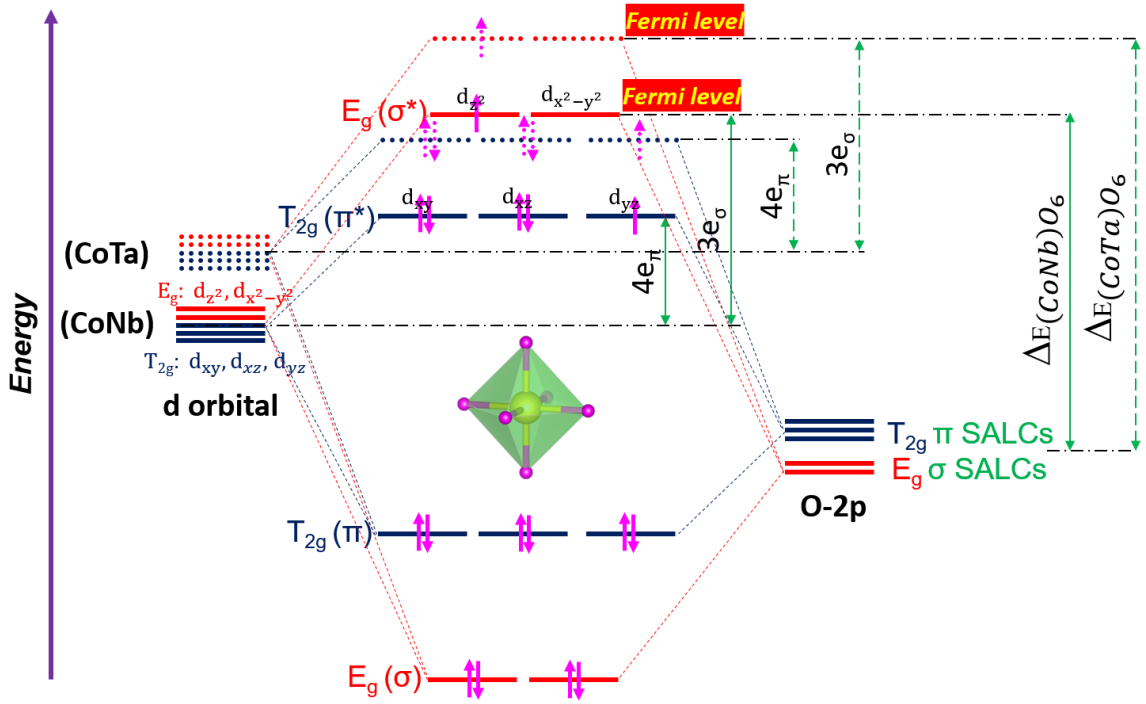

Figure 5.5 Molecular orbital energy diagram for octahedra in SCN10 and SCT10. e_σ and e_π are the orbital energy changes at maximum overlap for σ and π bonds, respectively. Intermediate-spin $(t_{2g}^5 e_g^1)$ Co^{3+} are used when filling electrons into the molecular orbitals.

Due to the almost identical size of $(CoNb)O_6$ and $(CoTa)O_6$ (Figure 4.5), the interaction between atomic orbitals (AO) of metals and oxygen $(2p^4)$ is similar. Hence, the energy change resulted from the AOs-to-MOs formation can be viewed the same for $(CoNb)O_6$ and $(CoTa)O_6$.[176-177] Since the AOs of Ta $(5d^3 6s^2)$ lie higher than that of Nb $(4d^4 5s^1)$, those anti-bonding MOs ($T_{2g}(\pi^*)$ and $E_g(\sigma^*)$) in $(CoTa)O_6$ is located higher than $(CoNb)O_6$. On the other hand, the Co-ion in SCN10 and SCT10 have a mixed oxidation state of $Co^{2+/3+}$ above 650 °C as shown in Figure 5.3b.[97, 172] Since possible spin-states for Co^{3+} are high-spin $(t_{2g}^4 e_g^2)$ or intermediate-spin $(t_{2g}^5 e_g^1)$, [81] whereas high-spin

state ($t_{2g}^5 e_g^2$) is known for Co^{2+},[81, 103-104] electrons will fill up $E_g(\sigma^*)$ for all the possible spin states of Co-ion, which results in the Fermi level lying at $E_g(\sigma^*)$ for both $(CoNb)O_6$ and $(CoTa)O_6$ octahedra. As a result, the energy barrier (Δ_E) for $V_O^{\cdot\cdot}$ migration is higher for SCT10 than SCN10, which is consistent with the above results on $\widetilde{D}_{V_O^{\cdot\cdot}}$.

The modeled $k_{s,f}$ for SCT10 as well as SCN10 are shown in Figure 5.4 (b) and Table 5.1. The $k_{s,f}$ shows the same trend as $\widetilde{D}_{V_O^{\cdot\cdot}}$ for SCN10 and SCT10, *i.e.* SCN10 has a higher $\widetilde{D}_{V_O^{\cdot\cdot}}$ and $k_{s,f}$, and lower E_a than SCT10. Understanding that the bulk migration of oxygen species (such as $V_O^{\cdot\cdot}$, O^-, O_2^- or O_2^{2-}) also links to the surface exchange rate in MIECs,[33, 35] the same trend of $k_{s,f}$ and $\widetilde{D}_{V_O^{\cdot\cdot}}$ is thus expected.[178]

The oxygen-ion diffusion coefficient ($\widetilde{D}_{O^{2-}}$) is correlated with $\widetilde{D}_{V_O^{\cdot\cdot}}$ by [165]

$$\tilde{D}_{O^{2-}} = \frac{\delta}{3-\delta}\tilde{D}_{V_O^{\cdot\cdot}} \tag{5-24}$$

The results are compared with the reported values in Table 5.2, where $\widetilde{D}_{V_O^{\cdot\cdot}}$ and k_s of SCN10 and SCT10 are shown in the same order of magnitude as those state-of-the-art MIECs, further demonstrating the validity of our modeled results.

Table 5.2 Comparison of oxygen diffusion coefficients and surface exchange rate obtained in this work with literature data at 800 °C (unless specifically indicated).

Composition	$\widetilde{D}_{O^{2-}}$ (cm^2 s^{-1})	k_s (cm s^{-1})	Method	Ref.
$Ba_{0.5}Sr_{0.5}Co_{0.8}Fe_{0.2}O_{3-\delta}$	4.59×10^{-6}	4.73×10^{-4}	Oxygen Permeation Feed: 0.07-0.39 atm Sweep: 0.005-0.05 atm	167
$Ba_{0.5}Sr_{0.5}Co_{0.8}Fe_{0.2}O_{3-\delta}$	3.0×10^{-6}	4.6×10^{-4}	Conductivity relaxation P_{O_2}range: 1-0.33 atm	179
$La_{0.6}Sr_{0.4}Co_{0.2}Fe_{0.8}O_{3-\delta}$	4.13×10^{-6} ($\widetilde{D}_{V_O^{\cdot\cdot}}$)	2.44×10^{-5}	Oxygen permeation Feed:0.21-1 atm	158

			Sweep: 0.00046-0.0023 atm	
$La_{0.58}Sr_{0.4}Co_{0.2}Fe_{0.8}O_{3-\delta}$	2.01×10^{-5}	-	Conductivity relaxation P_{O_2} range: 0.21-0.1 atm	180
$SrCo_{0.95}Sc_{0.05}O_{3-\delta}$ (700 °C)	1.82×10^{-4}	1.67×10^{-3}	Conductivity relaxation P_{O_2} range: 0.21-0.1 atm	181
$La_{0.1}Sr_{0.9}Co_{0.9}Nb_{0.1}O_{3-\delta}$ (750 °C)	1.94×10^{-4}	4.52×10^{-2}	Conductivity relaxation P_{O_2} range: 0.21-0.05	182
SCN10	**1.22×10^{-4} ($\widetilde{D}_{V_O^{\cdot\cdot}}$: 7.54 $\times10^{-4}$)**	**3.83×10^{-3}**	**Oxygen permeation Calculated with δ at 0.21 atm**	**This work**
SCT10	**6.48×10^{-5} ($\widetilde{D}_{V_O^{\cdot\cdot}}$: 4.09 $\times10^{-4}$)**	**2.95×10^{-3}**		**This work**

- 5.4.3 Oxygen-ion conductivity (σ_i)

The oxide-ion conductivity σ_i are calculated by Nernst-Einstein equation $\sigma_{V_O^{\cdot\cdot}} = \frac{z_{V_O^{\cdot\cdot}}^2 F^2 c_{V_O^{\cdot\cdot}} D_{V_O^{\cdot\cdot}}}{RT}$. $D_{V_O^{\cdot\cdot}}$ is calculated by equation below.[165, 183]

$$D_{V_O^{\cdot\cdot}} = \tilde{D}_{V_O^{\cdot\cdot}} \frac{\partial ln c_{V_O^{\cdot\cdot}}}{\partial ln a_{V_O^{\cdot\cdot}}} = \tilde{D}_{V_O^{\cdot\cdot}} \frac{\partial ln\delta}{\partial ln P_{O_2}} \quad (5\text{-}25)$$

where $c_{V_O^{\cdot\cdot}}$ is calculated from eq. (5-17) with V_m taken from Ref.[97, 172] The δ and $\frac{\partial ln\delta}{\partial ln P_{O_2}}$ are calculated from eq. (5-18) and (5-19). The calculated σ_i are plotted in Figure 5.6 (a) as a function of T, where σ_i (at P_{O_2}=0.21 atm) of SCN10 and SCT10 are shown to be 1.08 and 0.70 S cm^{-1} at 800 °C, and 0.34 and 0.17 S cm^{-1} at 650 °C, respectively, comparable with the reported values for $SrCoO_{3-\delta}$, $Ba_{0.5}Sr_{0.5}Co_{0.8}Fe_{0.2}O_{3-\delta}$ and $La_{0.2}Sr_{0.8}Co_{0.8}Fe_{0.2}O_{3-\delta}$.[184-186] The magnitude and activation energy of σ_i for these two MIECs are higher and smaller than those of pure oxygen-ion conductors, respectively. The dominating electronic conduction apparently promotes the migration of oxygen vacancies through the known

"drag-pull" mechanism mandated by the local charge neutrality.[165, 170] The σ_i at 700 and 800 °C in a typical P_{O_2} range of 0.001-1 atm are also calculated in Figure 5.6 (b). σ_i of SCN10 and SCT10 follows well with P_{O_2} by the power law $\sigma_i = \sigma_{i,0}(P_{O_2})^m$, where $\sigma_{i,0}$ is the conductivity at P_{O_2} =1 atm. The small and constant m value indicates the nature of ionic conduction. Similar behavior has also been observed in (LaSr)$CoO_{3-\delta}$ [187] and (LaCa)$CrO_{3-\delta}$[188] systems.

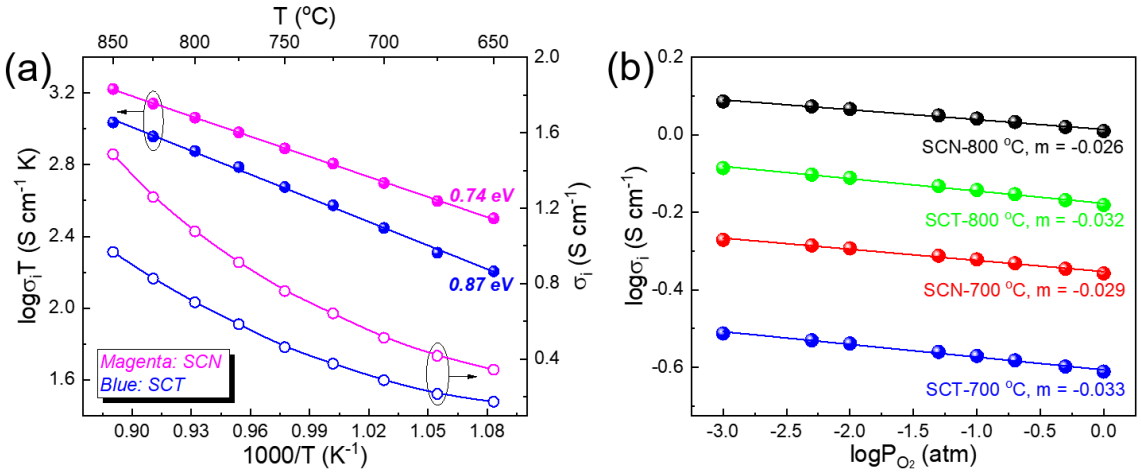

Figure 5.6 The calculated σ_i of SCN10 and SCT10. (a) Arrhenius plot at P_{O_2}=0.21 atm; (b) vs P_{O_2}. The data from 2.35 mm membranes are used for the calculation.

- 5.4.4 Electrical conductivity

The electrical conductivity of SCT10 is much higher than that of SCN10 below 400 °C but come close to each other above that, as seen in Figure 5.7. The conductivity of SYC10 is also added into comparison and found much higher than SCT10 or SCN10 above 350 °C. In general, hopping of electrons between two neighboring Co-ions is mediated by the conduction band formed by the orbital overlap between Co-3d and O-2p commonly known as a double exchange phenomenon.[189] The stronger the overlap, the easier for electrons to hop. Lattice size of SCT10 is smaller than SCN10 below 400 °C (Figure 4.5), which means

a shorter Co-O length, closer overlap of Co-3d/O-2p, and broader band for the charge carriers moving. At T>400 ºC, the lattice sizes of SCN10 and SCT10 are almost identical. The slightly higher Co-ion oxidation state of SCT10 (Figure 4.8) accounts for its slightly higher electrical conductivity, as it promises higher $h^{\cdot}$ concentration and better overlap between Co-3d and O-2p.[190-191] A schematic energy diagram of Co-3d and O-2p in anti-bonding MOs ($T_{2g}(\pi^*, HOMO)$ and $E_g(\sigma^*, LUMO)$) for Co^{2+}, Co^{3+} and Co^{4+} is shown in Figure 5.8. As for the much higher conductivity of SYC10, the much smaller lattice of SYC10 than SCN10 or SCT10 shown in Figure 4.5 gives the stronger orbital overlap between Co-3d and O-2p, which offer SYC10 broader band for $h^{\cdot}$ conduction even though it has lower average Co-ion oxidation state as shown in Figure 4.8.

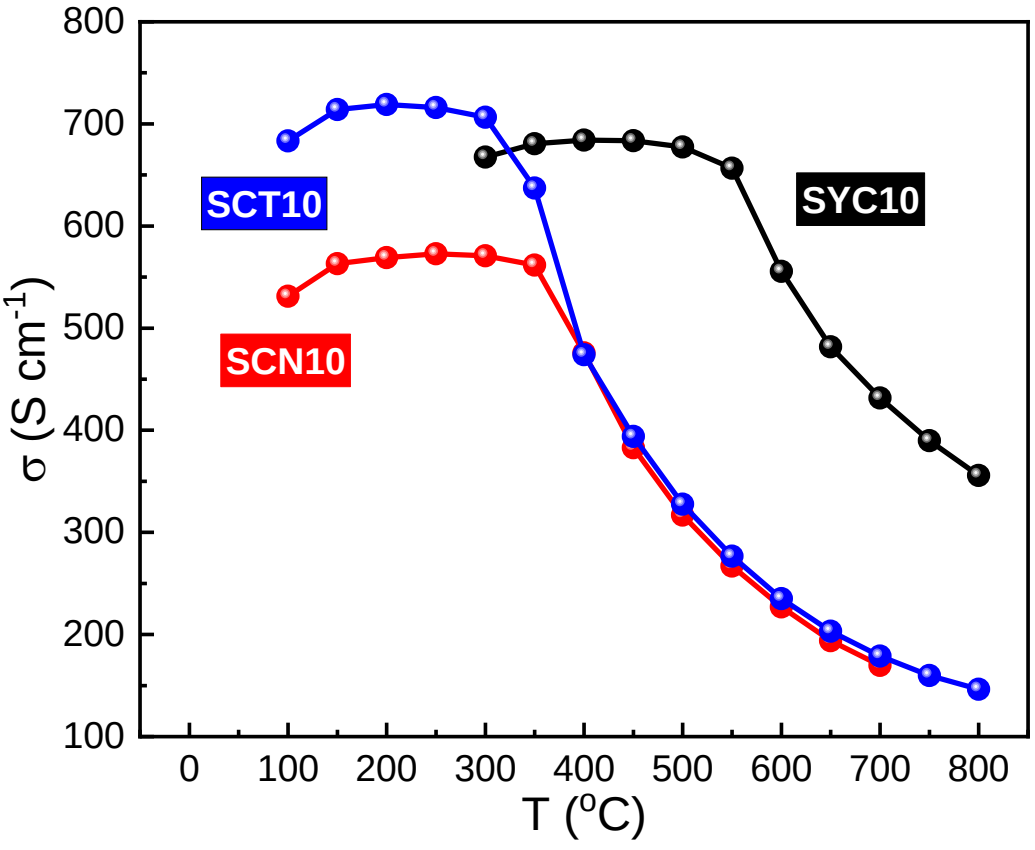

Figure 5.7 Electrical conductivity of SCN10, SCT10 and SYC10 in air.

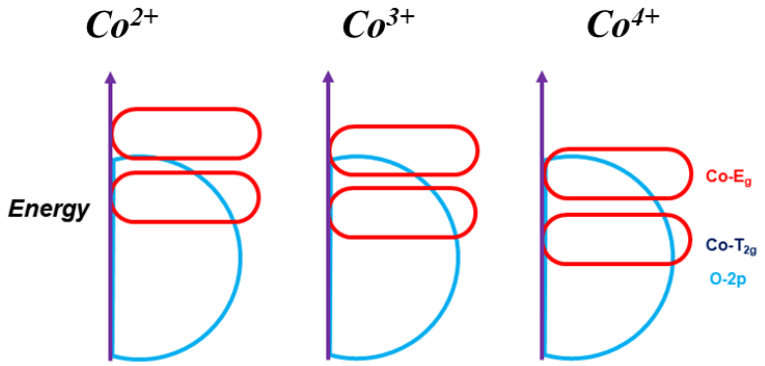

Figure 5.8 A schematic energy diagram of Co-3d and O-2p in anti-bonding T_{2g} and E_g.

The isothermal time-dependence of σ(t) for the SCT10 is shown in Figure 5.9 (a). Over a 150-h period, σ remains constant at 500, 600 and 700 ºC, reflecting good thermal stability of the material. Only at 800 ºC does σ exhibit a slight degradation. Upon returning to 500 ºC, SCT10 cannot recover to its original value, inferring a change in phase composition. A subsequent RT-XRD analysis shown in Figure 5.9 (b) confirms the formation of the less conductive hexagonal $Sr_6Co_5O_{15}$ phase through the formation of orthorhombic $Sr_2Co_2O_5$ at higher temperatures, which is deemed responsible for the loss of conductivity. In comparison, its rivalry SCN10 shown in the inset exhibits a noticeable decay in σ at a lower 700 ºC. This is clearly attributed to a weaker Nb-O bonding, resulting in earlier decomposition.[58] The sample after long-term conductivity measurement suggests a partial phase decomposition. Therefore, use of SCT10 in SOFC at ≥800 ºC should be cautioned. The low Bragg intensities of the impurities suggests that the reaction to form hexagonal $Sr_6Co_5O_{15}$ is a rather slow process.

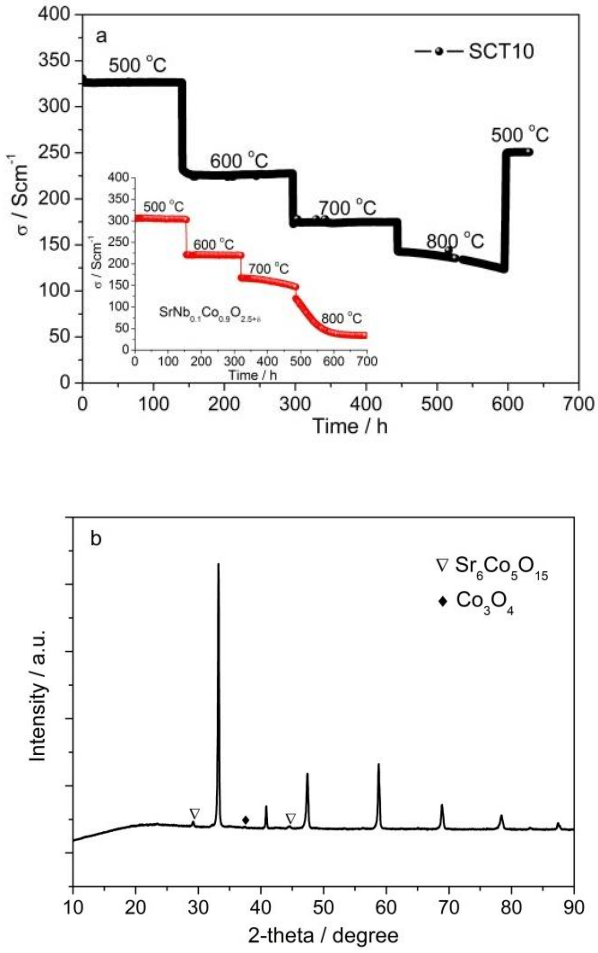

Figure 5.9 (a) Electronic conductivity stability of SCT10 at different temperatures. The inset shows conductivity stability of $SrCo_{0.9}Nb_{0.1}O_{3-\delta}$ (SCN10)[58]; (b) RT-XRD pattern of SCT10 after long-term conductivity measurement.

- 5.4.5 Evaluation of electrochemical activity

The polarization resistances of SCT10 and SCN10 vs temperature are shown in Figure 5.10, with the values of SYC10 and the benchmark cathode LSCF ($La_{0.60}Sr_{0.40}Co_{0.20}Fe_{0.80}O_{3-\delta}$) also being added into comparison. All the doped-SCOs show much lower R_P than LSCF. SCN10 is more active than SCT10, consistent with the molecular orbital energy analysis

in section 5.4.2. The polarization resistances of SYC10 are much higher, which is consistent with the much larger energy gap between the Fermi level and O-2p band level in SYC10 due to the shorter Co-O bond length and lower oxidation states of Co-ion. The electrochemical stability of the more active SCN10 and SCT10 are also evaluated at 700 ^{o}C as shown in Figure 5.11. While the initial R_P of SCT10 is higher than SCN10, SCT10 is rather stable over a period of 2,000 h. In comparison, SCN10 shows a R_P continuously increasing with time. After 500 h, the projected SCN10's R_P surpasses SCT10. A better thermal stability of SCT10 than SCN10 as indicated by the above results is the fundamental reason for the stable R_P observed.

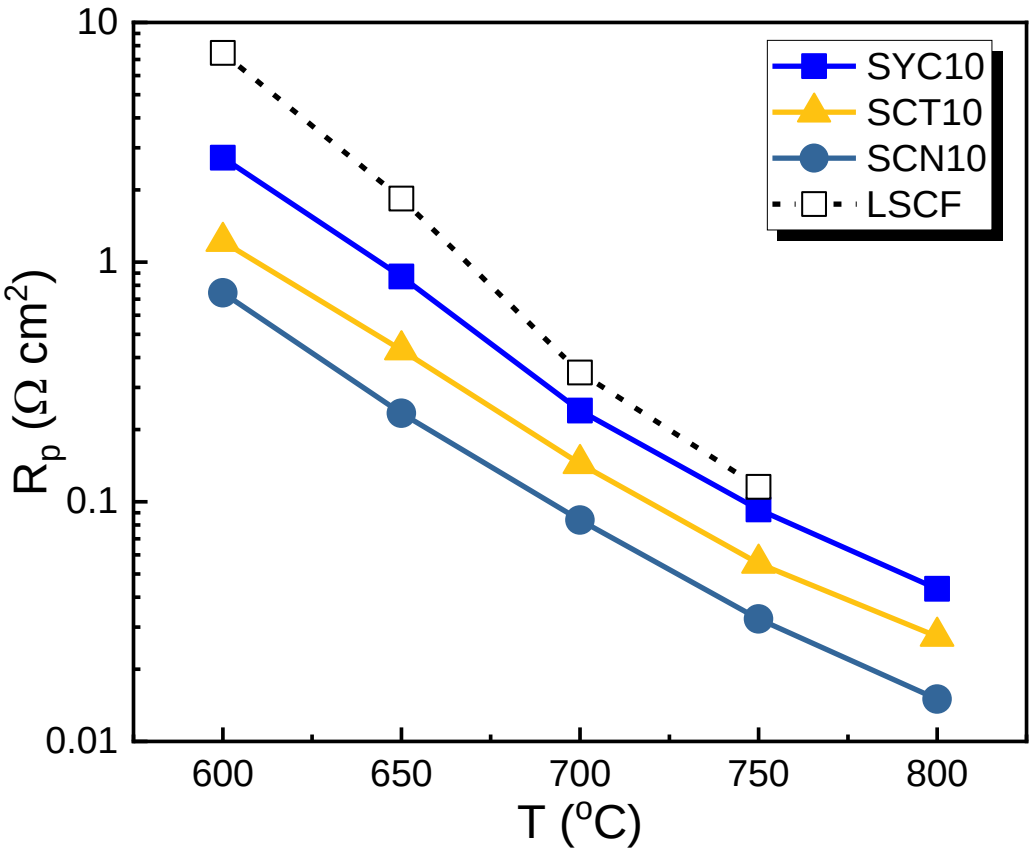

Figure 5.10 Polarization resistances in air for SYC10, SCN10 and SCT10.

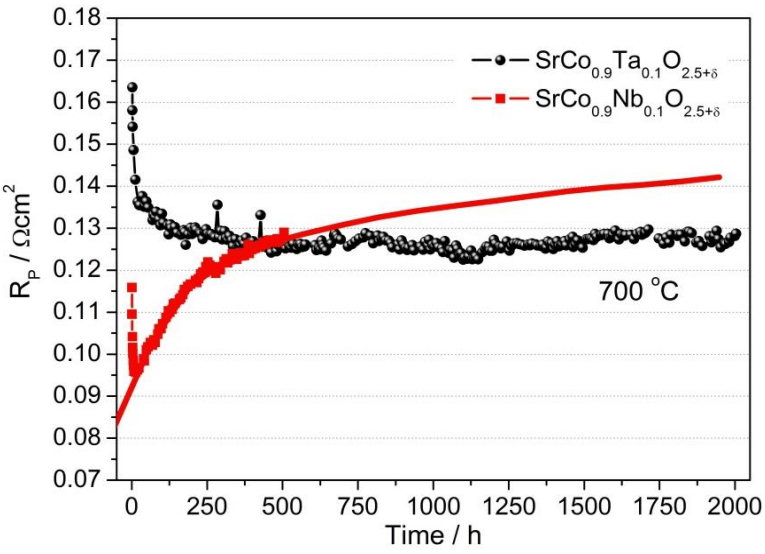

Figure 5.11 R_P of SCT10 *vs* time and its comparison with SCN10[58].

5.5 Conclusions

In summary, a combined experimental and theoretical method to derive important oxide-ion transport properties of SCN10 and SCT10, two well-known MIECs, is demonstrated through experimental J_{O_2} *vs* P_{O_2} data and a diffusion model. The bulk oxygen diffusion coefficients and surface oxygen exchange rate constants for SCN10 and SCT10 are found comparable with other state-of-the-art MIECs. Compared to SCT10, SCN10 shows a higher $\widetilde{D}_{V_O^{\cdot\cdot}}$ and $k_{s,f}$ with a corresponding lower E_a. The molecular orbital energy analysis reveals that the outer orbital electron configuration in Ta^{5+} and Nb^{5+} plays a major role in the energy barrier for $V_O^{\cdot\cdot}$ migration. The obtained σ_i of SCN10 and SCT10 are insensitive to the change of P_{O_2} and are nearly one order of magnitude higher than pure ionic conductors.

The shorter Co-O bond length or higher Co-ion oxidation state give a better overlap between Co-3d and O2-2p, and thus broader band for charge carrier migration. The conductivity measurement indeed unveils that SYC10 has a much higher electrical conductivity than SCN10 and SCT10, even though its average Co-ion oxidation state is lower. Molecular orbital energy analysis shows the energy gaps between Fermi level and O-2p level follow the sequence that SYC10 > SCT10 > SCN10, consistent with the trend of their polarization resistance. However, the long-term tests of the more active SCN10 and SCT10 show that SCT10 has a better thermal and electrochemical stability than SCN10. The fundamental reason for the improved stability is the stronger Ta-O bond than Nb-O bond in doped SCOs.

CHAPTER 6

THE EVALUATION OF SCT10 IN REAL SOFC CATHODE

6.1 Introduction

The commercial development of solid oxide fuel cell (SOFC) technology in recent decades has been mainly focused on how to lower the working temperature so that cost and reliability can both be improved to meet the targets for commercial applications.[108, 192] The current benchmark cathodes generally have insufficiently fast kinetics towards oxygen reduction reaction (ORR) to yield a low enough polarization resistance in reduced temperature ranges.[193] A representative of the first-generation benchmark cathodes is $La_{1-x}Sr_xMnO_{3-\delta}$ (LSM), a pure electronic conductor. Therefore, its ORR kinetics relies solely on the density of triple-phase (air/cathode/electrolyte) boundaries (3PBs),[194] which limits this class of SOFC cathodes to work at a temperature as high as 900-1000 ºC.

Replacement of LSM with mixed ionic and electronic conductors (MIECs) extends the ORR-active sites from 3PBs to air/cathode two-phase boundaries (2PBs), thus significantly increasing reaction areas and enhancing ORR-kinetics. Representatives of this second-generation benchmark cathodes are oxygen-deficient perovskites such as $(Sm,Sr)CoO_{3-\delta}$[11-12], $(Ba,Sr)(Co,Fe)O_{3-\delta}$[13, 108], and $(La,Sr)(Co,Fe)O_{3-\delta}$ [16, 18]. Due to the high ORR-activity, this class of SOFC cathodes is suited for intermediate-temperature SOFCs

(IT-SOFCs). However, the high ORR-activity of these materials is accompanied by a much higher thermal expansion coefficient (TEC) than that of electrolyte (*e.g.* 20 *vs* 10 ppm/K), making them a direct use as bulk cathode in IT-SOFCs impossible.[195-197] To avoid the TEC problem while still utilizing the high ORR activity, these materials are often employed in form of nanoparticles (NPs) supported on a TEC-compatible skeleton.[198-200,201-202] At elevated temperatures, however, NPs are prone to sinter, resulting in performance degradation. [72, 203-204] Some studies have informed us that by coating NPs with a continuous and conformal layer using atomic layer deposition (ALD) can effectively decrease the rate of NPs coarsening. [205-206]

Note that most of ORR-active perovskites uses Sr as a dopant to increase electronic conductivity and oxygen vacancy concentration. One critical issue with these Sr-doped perovskites (SDPs) such as $La_{0.6}Sr_{0.4}Co_{0.2}Fe_{0.8}O_{3-\delta}$ (LSCF) and $La_{0.6}Sr_{0.4}CoO_{3-\delta}$ (LSCo) is the Sr-segregation originated from the electrostatic interaction between dopant (Sr'_{La}) and oxygen vacancy ($V_O^{\cdot\cdot}$)[207-208], a leading cause for the performance degradation[18, 209-210]. Similar to NPs coarsening mitigation, some early studies have shown the effectiveness of overcoating a conformal less reducible oxide-layer over SDPs to diminish the concentration of $V_O^{\cdot\cdot}$ and thus the driving force for Sr-segregation. [205-206]

In this chapter, a new coarsening-resistant and Sr-segregation free, yet highly active, cathode for IT-SOFCs is presented. The new cathode consists of a continuous $SrCo_{0.9}Ta_{0.1}O_{3-\delta}$ (SCT10) nano-scaled thin-film, over an LSCF skeleton. In such a structure, ORR mainly takes place on the surface of SCT10 while porous LSCF skeleton provides electronic/ionic conduction, gas transport and mechanical support. The structure may have less reactive surface areas than conventional discrete NPs, but it is more resistant to

coarsening. The reduced surface area can be compensated by the high intrinsic ORR-activity in SCT10. [172, 211-212] More importantly, Sr-segregation mechanism is completely shut down in SCT10 since there is no negatively charged dopant Sr'_{La} to electrostatically attract positively charged $V_O^{\cdot\cdot}$.

6.2 Experimental Method

- 6.2.1 Preparation of SCT10 precursor solution

To make the SCT10@LSCF structure, we used an aqueous solution containing Sr, Co and Ta as the precursor and infiltrated it into the LSCF skeleton. To make the solution, citric acid (Sigma-Aldrich) was first dissolved in a de-ionized water, followed by adding a stoichiometric amount of $Sr(NO_3)_2$ (Alfa Aesar) and $Co(NO_3)_2{\cdot}6H_2O$ (Alfa Aesar) under stirring. A separate solution containing ethylene diamine tetraacetic acid (EDTA, Sigma-Aldrich) dissolved in a diluted ammonia water was then mixed with the above solution. The pH of the solution was adjusted to 8. A stoichiometric amount of $Ta(OC_2H_5)_5$ (Sigma-Aldrich) was last dissolved into pure ethanol and then slowly added into the above solution to complete the solution preparation for infiltration. The total metal-ions concentration was 0.2 M. The molar ratio of citric acid to EDTA to metal ions was 2:1:1. The volume ratio between de-ionized water and ethanol was 5:1 in the final solution.

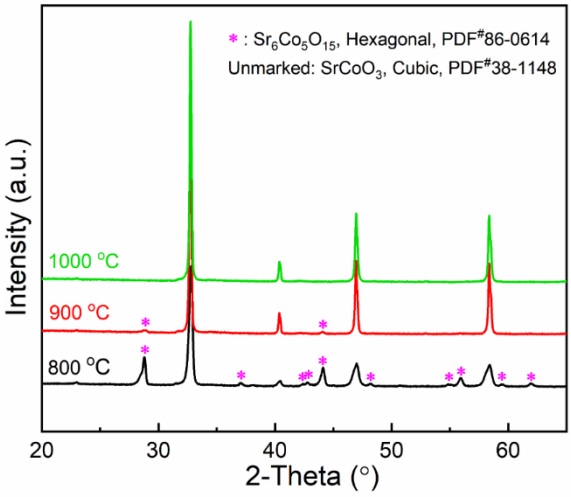

Figure 6.1 XRD patterns of solution-derived samples calcined at different temperatures.

To determine the right post-infiltration calcination temperature to form single-phase SCT10, a portion of the above solution was collected, dried at 80 °C and then ignited at 500 °C for 1 h. The resulting powder was then fired at 800, 900 and 1000 °C for 2 h, respectively. Figure 6.1 shows XRD patterns of samples calcined at different temperatures; it is evident that 1000 °C is the onset temperature for the formation of pure SCT10 phase from solution.

In addition to the pure phase formation, calcining SCT precursor at higher temperature also favors the formation of a continuous thin-film over the LSCF skeleton. We show the evidence in later section. This is different with those reported in the literature that only the transition from discrete to continuous layer of NPs over the skeleton were observed when calcinating at higher temperature.[213-214]

- 6.2.2 Fabrication of SCT10@LSCF symmetrical cells

The symmetrical cell was first fabricated by screen printing an LSCF ink (purchased from Fuelcellmaterials) on both side of a 500 μm thick $Gd_{0.2}Ce_{0.8}O_{2-\delta}$ (GDC20, Fuelcellmaterials) dense pellet, followed by firing at 1100 ºC for 2 h. The electrode has an effective electrode geometrical area of 1.27 cm^2 and a thickness of *ca.* 40 μm. A 10 μL of SCT10 solution was then dropped into each side of the porous LSCF skeleton, followed by thermal treatment at 80 ºC and 500 ºC for 1 h, respectively. The above process was repeated 9× to reach 20% SCT10 loading. The samples were finally fired at 1000 ºC for 2 h to form a pure SCT10 phase that covers completely the surface of LSCF skeleton. For all electrochemical testing, silver paste (c8829a, Heraeus) and silver mesh were attached as current collectors to both sides of the electrode and cured at 600 ºC for 1 h before use.

- 6.2.3 Electrochemical Impedance Spectroscopy (EIS)

The EIS spectra of symmetrical cells were collected with a 1470/1455B electrochemical station (Solartron) in a frequency range of 0.01 Hz-1 MHz and AC amplitude of 10 mV. The collected EIS spectra were analyzed with equivalent circuit method by ZSimpWin software.

- 6.2.4 Microstructure and phases characterization

The microstructures of electrodes were characterized by a field emission scanning electron microscope (FESEM, Zeiss Ultraplus) and high-resolution transmission electron microscope (HRTEM, Hitachi H-9500). A scanning transmission electron microscope (STEM, Hitachi HD-2000) equipped with EDX was also employed to obtain images as well as analyze chemical compositions. The resolutions for STEM-EDX are 0.8, 0.5 and 0.3 nm for spot, line-scan and mapping modes, respectively. X-ray photoelectron

spectroscopy (XPS) (Kratos AXIS Ultra DLD XPS) were performed to specifically analyze surface chemistry, particularly Sr-concentration, of cathode. To ensure the accuracy, the binding energy (BE) was calibrated by the C-1s photoemission peak at 284.6 eV. The phases were examined by an X-ray diffractometer (Rigaku MiniFlex II) equipped with graphite-monochromatized Cu Kα radiation (λ= 1.5418 Å).

6.3 Results and Discussion

- 6.3.1 The microstructure of SCT10@LSCF cathode

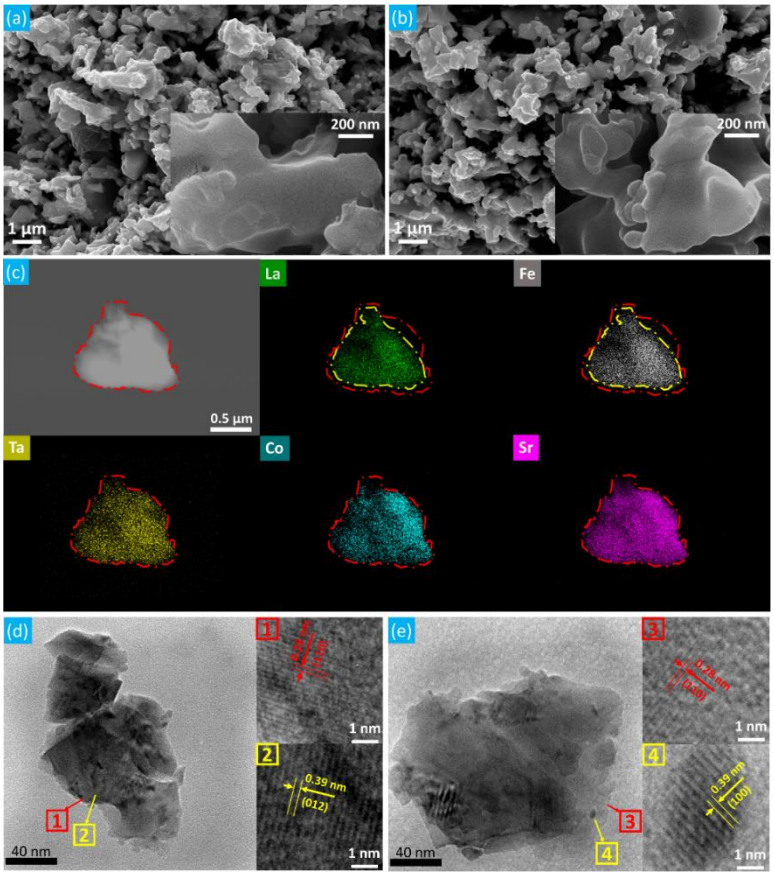

Figure 6.2 The SEM images of (a) as-prepared LSCF and (b) SCT10@LSCF cathodes. The insets are images at higher magnification; (c) the STEM-EDX mapping of as-prepared SCT10@LSCF particle; (d) and (e) are the HRTEM images of as-prepared LSCF and SCT10@LSCF particles, respectively.

The microstructures of the as-prepared SCT10@LSCF and pristine LSCF cathodes captured by SEM are shown in Figure 6.2 (a) and (b), respectively, where almost identical particle morphology, porosity and particle sizes are observed. A further compositional analysis by STEM-EDX indicates that the elemental distributions in the as-prepared SCT10@LSCF is not uniform. Figure 6.2 (c) shows that La and Fe from LSCF only exist in the core of particles, around which Ta from SCT distributes evenly. The spatial distributions of those shared elements in SCT10@LSCF (Co, Sr) are also consistent with the bilayer structure. Note that both SCT10 and LSCF are perovskites with corner-shared 3*d* metal-oxygen octahedra.[172, 215] Indeed, HRTEM images of Figure 6.2 (d) and (e) indicate that both SCT10 and LSCF are crystalized into similar structure with identical *d*-spacings. It is, therefore, reasonable to postulate that an iso-structured bilayer has been formed. The more active SCT10 outer layer is expected to provide a high ORR activity while porous LSCF under layer to provide an electron/ion conducting pathway, channel for gas transport and mechanical support.

The formation of bilayer architecture is originated from the high calcination temperature and the isostructural SCT10 and LSCF. Early studies have shown that the morphology of infiltrants depends largely upon the calcination temperature. Lou et al. reported a NP-skeleton morphology for the isostructural infiltration of $Sm_{0.5}Sr_{0.5}O_{3-\delta}$ into $La_{0.6}Sr_{0.4}Co_{0.2}Fe_{0.8}O_{3-\delta}$ when calcinating at much lower temperature of 800 ^{o}C.[202] Similar morphologies are also obtained in this work when calcinating at 800 ^{o}C as shown in Figure 6.3. For heterostucture infitration, higher calcinating temperature only leads to the transition of discrete-to-continuous layer of NPs, such as $La_{0.6}Sr_{0.4}Co_{0.2}Fe_{0.8}O_{3-\delta}$ into GDC at 1200 ^{o}C[213], Sm, Ce-doped $SrCoO_{3-\delta}$ into $Sm_{0.2}Ce_{0.8}O_{1.9}$[214], $LaNi_{0.6}FeO_{3-\delta}$ into porous

yttria-stablized zirconia at 1100 ºC[216]. A schematic illustration of temperature and crystal structure effects on the morphology of bilayer architecture is given in Figure 6.4.

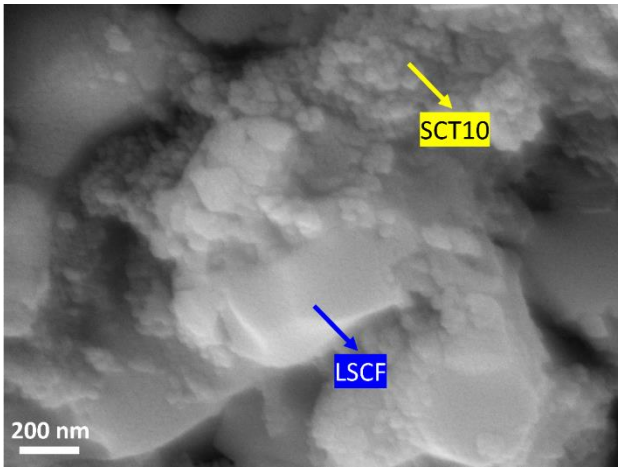

Figure 6.3 The SEM images of SCT10@LSCF cathode calcinated at 800 ºC for 1 h after infiltration.

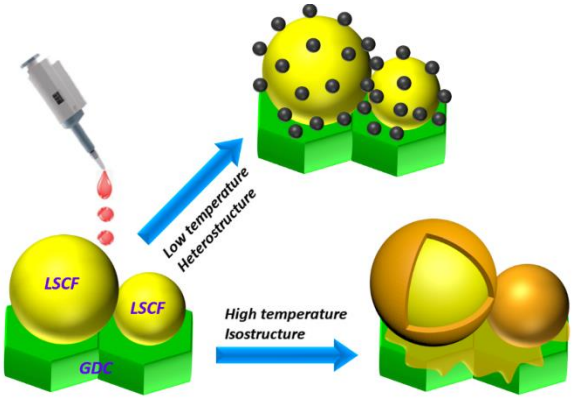

Figure 6.4 The mechanism schematic of bilayer structured cathode particles.

- 6.3.2 Stability test on symmetrical cell

The stability of SCT10@LSCF and pristine LSCF cathodes was tested for 5,000 h in symmetrical cells at 700 ºC in air; the results are shown in Figure 6.5 (a). It is evident that

the polarization resistance of the pristine LSCF, R_P, doubles from 0.40 to 0.81 Ω cm^2 after 5,000 h. A SEM examination shown in Figure 3b on the post-test LSCF cathode indicates an increased particle size in comparison to the original morphology shown in Figure 6.1 (a). It appears that particle coarsening is one of the reasons that causes degradation. In contrast, Figure 6.5 (a) shows only 21% increase (from 0.28 to 0.34 Ω cm^2) in R_P of the SCT10@LSCF cathode after 5,000 h. The post-test SEM analysis shown in Figure 6.5 (c) reveals less particle agglomeration than the pristine LSCF.

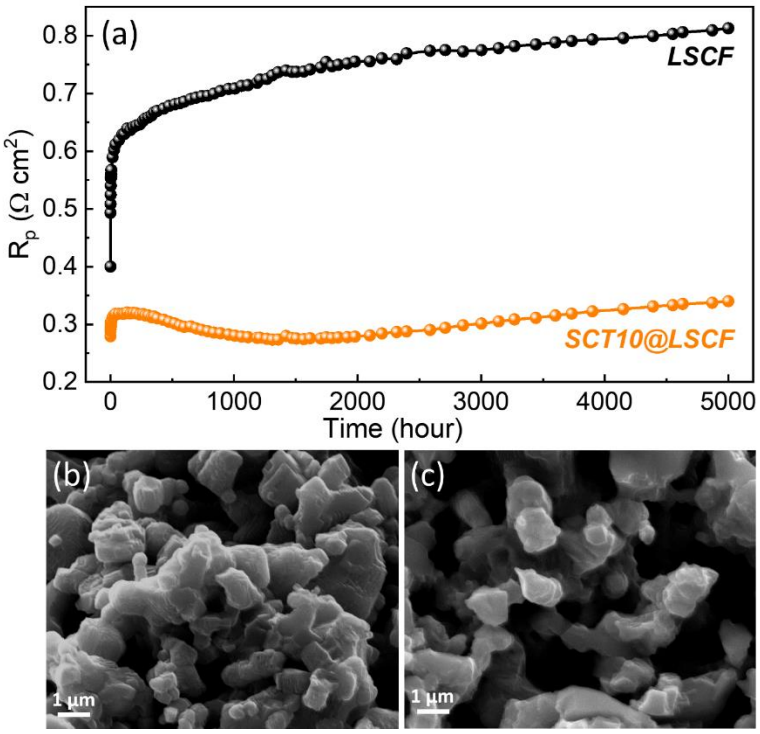

Figure 6.5 (a) The time-dependent polarization resistances at 700 °C; the cathode morphology in symmetrical cells of (b) LSCF and (c) LSCF-SCT after 5000 h test at 700 °C.

Another source of degradation for the pristine LSCF cell is the well-documented Sr-segregation.[18, 207-210] The morphology of the post-test samples shows an evidence of segregated Sr-compound in the pristine LSCF, see Figure 6.6.[18] To further verify the SEM

observation, XPS was performed on a separate set of the sinter samples annealed at 700 ºC for only 200 h. with a goal of determining the surface Sr-concentration.[217-218] Figure 6.7 (a) shows that the ratio of surface-Sr/lattice-Sr in the pristine LSCF increases from 45.4/54.6 to 54.5/45.5 after the annealing, while Figure 6.7 (b) shows an almost constant ration for SCT10@LSCF. These results suggest that the SCT10@LSCF has a much better resistance to the Sr-segregation than LSCF. The excellent stability and low R_P of SCT10@LSCF suggest that the isostructural bilayer design is a promising strategy for commercially viable IT-cathodes.

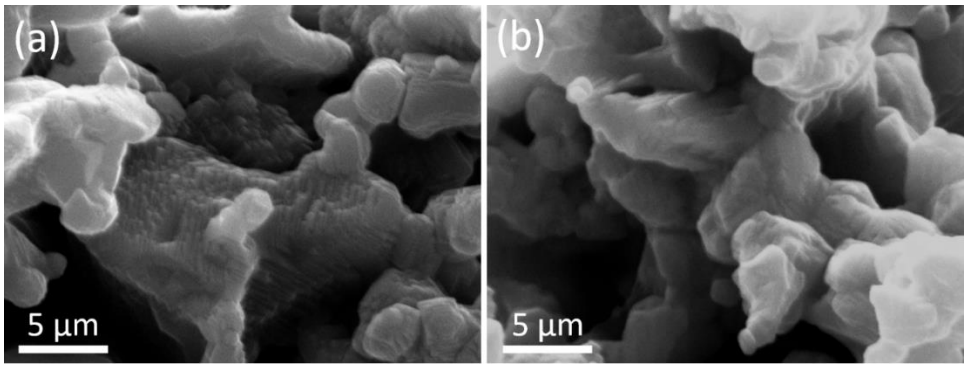

Figure 6.6 The cathode morphology after 5000 h test at 700 ºC of (a) LSCF and (b) SCT10@LSCF.

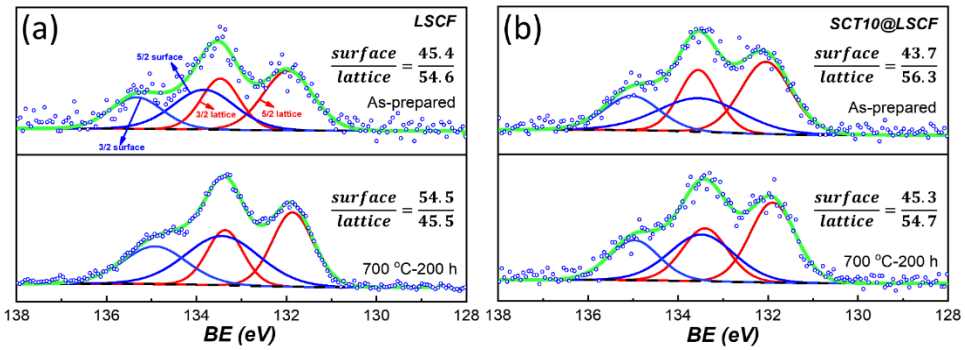

Figure 6.7 The Sr-3*d* XPS patterns of samples before and after annealing at 700 ºC for 200 h.

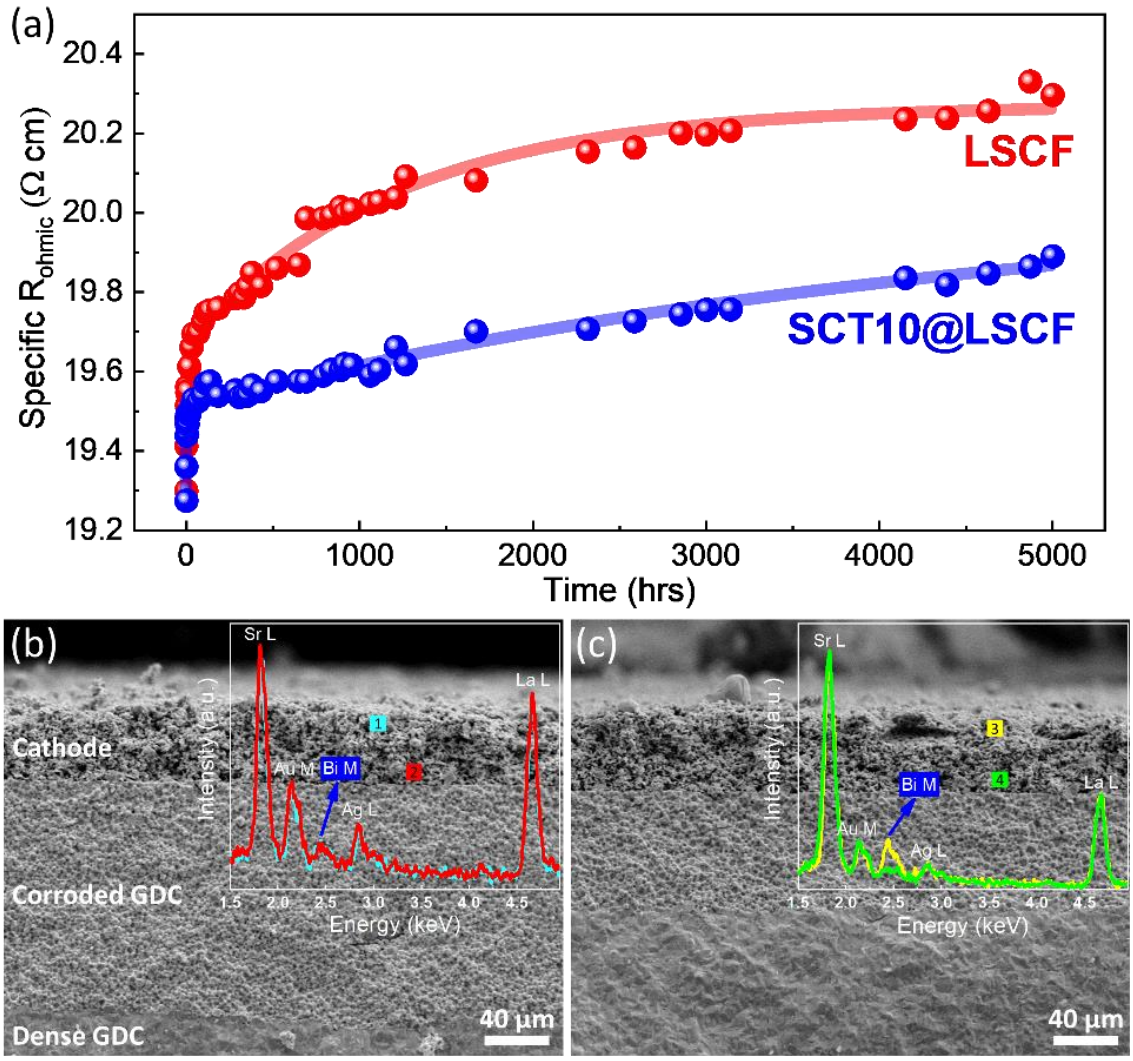

Figure 6.8 (a) The time dependent ohmic resistances of symmetrical cells with (a) LSCF and SCT10@LSCF as cathode at 700 ºC; (b) cross-sectional view of LSCF/GDC and (c) SCT10@LSCF/GDC interfaces after 5,000 h test. The insets are the SEM-EDX in those areas marked by the numbers.

We recently reported a "bismuth attack" from the commercial current collector silver paste to GDC electrolyte.[219] The SCT-layer shows another advantage of lessening such an attack as seen from the less degradation and thinner corroded layer in Figure 6.8. The specific resistance increases from 19.30 to 20.30 Ω cm for the cell with LSCF as cathode, while the one with LSCF-SCT as cathode only increase from 19.27 to 19.89 Ω

cm after 5000 h test at 700 ºC, as seen in Figure 6.8 (a). The bismuth migration path of silver paste-to-cathode-to-electrolyte is blocked for the infiltrated sample, probably arise from the adsorbing effect of the SCT-layer. To confirm this hypothesis, we performed EDS analysis in various regions of the electrodes; the results are shown in the insets of Figure 6.8 (b) and (c). A strong Bi-presence is observed in both the top and bottom regions of LSCF (Figure 6.8 (b)), whereas the Bi-presence in SCT10@LSCF bulk is much more weakened at the bottom than the top region (Figure 6.8 (c)). The absorbing effect of SCT10-shell might also be applied to mitigate the Cr-poisoning issue in SOFC stack, as analogous to the "Cr-getter" based on SrO-containing compounds.[220]

- 6.3.3 Single cell performance

The peak power densities (P_{peak}) reach 1.32 and 0.48 W cm^{-2} for single cell with SCT10@LSCF as cathode at 700 and 600 ºC, respectively, as shown in Figure 6.9 (a). The power outputs easily outrun the single cell with LSCF as cathode at identical test conditions, the later only demonstrates P_{peak} of 0.75 and 0.28 W cm^{-2} at 700 and 600 ºC, respectively. The continually operating at *ca.* 70% of P_{peak} (0.6 V-potentiostatic) also shows that the sample with the bilayer structured cathode is more stable than the baseline sample, e.g. 0.92 to 0.41 W cm^{-2} *vs* 0.57 to 0.16 W cm^{-2} at 700 ºC for 100 h (Figure 6.9 (b)). The EIS of single cells in Figure 6.9 (c) indicate that the electrode polarization resistances increase from 0.06 to 0.18 Ω cm^2 for the baseline sample, but the cell with SCT10@LSCF as cathode only slight increases from 0.05 to 0.10 Ω cm^2 during the continually discharging. The single cell tests reaffirm the superiority of the bilayer structured SCT10@LSCF over the pure LSCF.

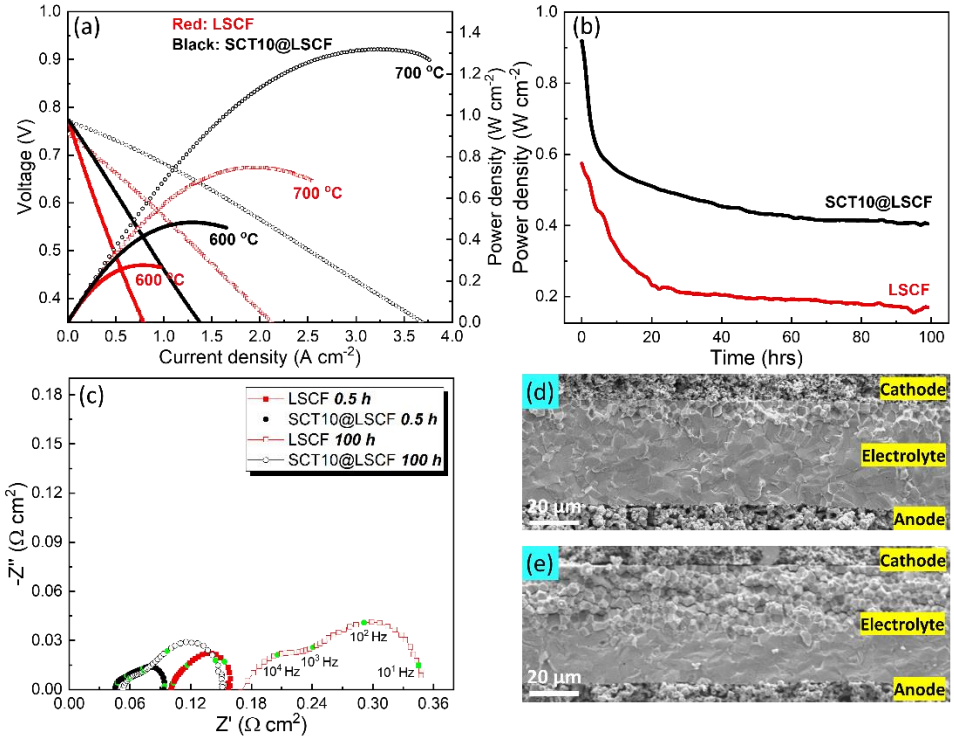

Figure 6.9 (a) short-term IV and current-power (IP) curves. (b) Power density vs time at 0.6 V, 700 ºC; corresponding EIS spectra (c); cross-sectional views of cells after testing with (d) SCT10@LSCF or (e) LSCF as cathode.

It is noticeable that the infiltration also decreases the ohmic resistances of single cells as seen from the top EIS patterns in Figure 6.9 (c). It is probably resulted from a higher conductivity of SCT than LSCF[172, 221] or lower contact resistance between cathode and electrolyte. After 100 h test, the ohmic resistance barely changes for the cell with SCT10@LSCF cathode; on the contrary, large increase is observed for the baseline cell. Figure 6.9 (d) and (e) shows the more severe morphology degradation with LSCF as cathode. Again, the SCT-layer shows its advantage of blocking the bismuth attack.

6.4 Conclusion

An effective combination between two isostructural materials, the benchmark LSCF and ORR-active SCT10, are realized in a form of bilayer structure through solution infiltration and high temperature calcination. The isostructural SCT10@LSCF cathode shows a dramatically enhanced ORR activity and stability. The polarization resistance of SCT10@LSCF remains mostly stable and low for 5,000 h in air at 700 ºC. The SCT10-outerlayer acts as an excellent ORR-catalyst, while inhibiting coarsening and Sr-segregation from the LSCF-underlayer. The stable and active isostructural SCT10@LSCF bilayer presented in this study promises a new approach to developing electrodes for commercial IT-SOFCs as well as IT solid oxide electrolysis cells (IT-SOECs) for H_2/CO production.

CHAPTER 7

SUMMARY

To achieve the ultimate goal of establishing structure-activity relationships, *in-situ* neutron diffraction (ND), thermogravimetric analysis (TGA), iodometric titration and electrochemical tests have been carried out to study the local structure, oxygen stoichiometry and oxygen reduction reaction (ORR) activity in solid oxide fuel cell (SOFC) operating temperature range for $Sr_{0.9}Y_{0.1}CoO_{3-\delta}$ (SYC10), $Sr_{0.9}Y_{0.3}CoO_{3-\delta}$ (SYC30), $SrCo_{0.9}Nb_{0.1}O_{3-\delta}$ (SCN10) and $SrCo_{0.9}Ta_{0.1}O_{3-\delta}$ (SCT10).

The ND reveals that the crystal structure of SYC30 contains alternate layered oxygen-deficient Co1-layer and oxygen-saturated Co2-layer in a new ordered perovskite lattice with a large unit cell (2a×2a×4a) and I4/mmm space group, from RT to 900 ºC. The way how $V_o^{\cdot\cdot}$ is distributed in SYC30 infers a 2D diffusion pathway in *ab* plane around Co1. The Fourier observed nuclear density map reveals that the nuclear density of O4-site expands with temperature in the *ab* plane, which is beneficial to oxygen migration. In comparison, SYC10 has a similar stacking sequence of Co1- and Co2-layer but crystalizes into a lattice with higher symmetry (a×a×2a, P4/mmm). The more symmetrical structure and $V_o^{\cdot\cdot}$ distribution, and higher $V_o^{\cdot\cdot}$ concentration in SYC10 indicate an easier $V_o^{\cdot\cdot}$ migration than SYC30. Molecular orbital energy analysis also indicates SYC30 has a higher Fermi level relative to O-2p energy level in the active Co1-polyhedra, and thus a higher motional

enthalpy for $V_O^{\cdot\cdot}$ migration. These observations are consistent with the electrochemical results, where SYC30 is found to have a higher polarization resistance and worse single-cell performance than SYC10.

For SCN10, at T< 75 ^oC, ND reveals a tetragonal (P4/mmm) structure with a G-type magnetic ordering. Above 75 ^oC, the nucleus structure remains the same while the magnetic ordering disappears. A phase transition from tetragonal (a×a×2a, P4/mmm) to cubic (a×a×a, Pm-3m) is observed at 412 ^oC, where the two Co-sites and three O-sites in the P4/mmm phase converge into one equivalent site, respectively. The phase transition temperature coincides with the peak temperature of oxygen uptake obtained by TGA. It is also observed that the Nb-dopant has no preferred Co-site to occupy. The oxygen vacancies are mostly located at the O3-site surrounding the Co1-site in the P4/mmm structure. The intermediate-spin state of Co^{3+} at the Co1-site is responsible for the observed distortions of CoO_6 octahedra, *i. e.* elongation of $Co1O_6$ octahedra and shortening of $Co2O_6$ octahedra along the c-axis, a phenomenon known as Jahn-Teller distortion. At high temperatures, large thermal displacement factor for O^{2-} is observed with high concentration of oxygen vacancies, providing a structural environment favorable to high O^{2-} conductivity in Nb-doped $SrCoO_3$-based oxygen electrode materials.

For SCT10, the high-temperature X-ray diffraction (HT-XRD) and ND studies reveal that it exhibits a single primitive cubic phase (a×a×a, Pm-3m) at ≥200 ^oC. In SOFC working temperature range, SCT10 and SCN10 have almost identical lattice and Co-ion oxidation states, while those for SYC10 are smaller. The smaller lattice renders SYC10 a higher electrical conductivity due to the stronger interaction between Co-3d and O-2p. The molecular orbital energy analysis, based on their lattice size and Co-ion oxidation states,

reveals that the energy gaps between Fermi level and O-2p level follow the sequence that SYC10 > SCT10 > SCN10. The electrochemical measurements unambiguously confirm that the energy gap can be used as a descriptor for the activities of $V_O^{\cdot\cdot}$ migration and the related ORR processes. The dependency of electronic conductivity and electrochemical activity on temperature and time for the more active SCN10 and SCT10 suggest that SCT10 is a better and more stable ORR catalyst, making it more attractive for practical applications. A summary of the key parameters at 700 ºC for SYC10, SCN10 and SCT10 are listed below.

Parameters	SYC10	SCN10	SCT10
δ (TGA)	2.52	2.56	2.59
Co-ion oxidation state (TGA)	2.94	2.91	2.97
BVS	2.76 (Co1)	3.02	3.02
Co-O bond length	1.96 (Co1)	1.97	1.97
Lattice size (Å)	3.91	3.95	3.95
$\Delta E_{Fermi\text{-}O\ 2p}$	Large	Small	Medium
R_p (Ω cm^{-2})	0.24	0.08	0.14

The practical application of SCT10 is evaluated as nanostructured particles, synthesized via a solution infiltration and high temperature sintering method, anchored on a commercial LSCF cathode to mitigate its incompatible thermal expansion with electrolytes. The new cathode shows a bilayer structure consisting of a continuous, nanoscale SCT10 thin layer covering a commercial isostructural perovskite LSCF cathode skeleton. The SCT10-outerlayer acts as an excellent ORR-catalyst, while inhibiting coarsening and Sr-segregation from the LSCF-underlayer. The polarization resistance of SCT10@LSCF is only 40% that of the pristine LSCF after 5,000 h stability test at 700 ºC. The peak power density reaches 1.32 W cm^{-2} for single cell with SCT10@LSCF as cathode at 700 ºC, while the one with LSCF as cathode only reaches 0.75 W cm^{-2}. The stable and

active isostructural SCT10@LSCF bilayer demonstrates a new promising approach to developing electrodes for commercial IT-SOFCs as well as IT solid oxide electrolysis cells (IT-SOECs) for H_2/CO production.

REFERENCES

1. Outlook, B. E., edition (2017). 2017.
2. Solomon, S.; Plattner, G.-K.; Knutti, R.; Friedlingstein, P., Irreversible climate change due to carbon dioxide emissions. *Proceedings of the national academy of sciences* **2009,** *106* (6), 1704-1709.
3. Crabtree, G.; Misewich, J.; Ambrosio, R.; Clay, K.; DeMartini, P.; James, R.; Lauby, M.; Mohta, V.; Moura, J.; Sauer, P., Integrating renewable electricity on the grid, *AIP Conference Proceedings*, AIP: 2011; pp 387-405.
4. Kobayashi, Y.; Ando, Y.; Kabata, T.; Nishiura, M.; Tomida, K.; Matake, N., Extremely high-efficiency thermal power system-solid oxide fuel cell (SOFC) triple combined-cycle system. *Mitsubishi Heavy Industries Technical Review* **2011,** *48* (3), 9-15.
5. Revankar, S. T.; Majumdar, P., Fuel cells: principles, design, and analysis. *CRC press*: 2014.
6. Bard, A. J.; Faulkner, L. R.; Leddy, J.; Zoski, C. G., Electrochemical methods: fundamentals and applications. *Wiley New York*: 1980; Vol. 2.
7. Sun, C.; Hui, R.; Roller, J., Cathode materials for solid oxide fuel cells: a review. *Journal of Solid State Electrochemistry* **2010,** *14* (7), 1125-1144.
8. Jacobson, A. J., Materials for solid oxide fuel cells. *Chemistry of Materials* **2009,** *22* (3), 660-674.
9. Van Heuveln, F.; Bouwmeester, H. J., Electrode properties of Sr-Doped $LaMnO_3$ on yttria-stabilized Zirconia II. electrode kinetics. *Journal of the Electrochemical Society* **1997,** *144* (1), 134-140.
10. Murray, E. P.; Barnett, S., (La, Sr)MnO_3–(Ce, Gd)O_{2-x} composite cathodes for solid oxide fuel cells. *Solid State Ionics* **2001,** *143* (3), 265-273.
11. Xia, C.; Liu, M., Low-temperature SOFCs based on $Gd_{0.1}Ce_{0.9}O_{1.95}$ fabricated by dry pressing. *Solid State Ionics* **2001,** *144* (3), 249-255.
12. Nicholas, J. D.; Barnett, S. A., Measurements and modeling of $Sm_{0.5}Sr_{0.5}CoO_{3-x}$–$Ce_{0.9}Gd_{0.1}O_{1.95}$ SOFC cathodes produced using infiltrate solution additives. *Journal of the Electrochemical Society* **2010,** *157* (4), B536-B541.
13. Shao, Z.; Haile, S. M.; Ahn, J.; Ronney, P. D.; Zhan, Z.; Barnett, S. A., A thermally self-sustained micro solid-oxide fuel-cell stack with high power density. *Nature* **2005,** *435* (7043), 795-798.
14. Shao, Z.; Haile, S. M., A high-performance cathode for the next generation of solid-oxide fuel cells. *Nature* **2004,** *431* (7005), 170-173.
15. Zhou, W.; Ran, R.; Shao, Z., Progress in understanding and development of $Ba_{0.5}Sr_{0.5}Co_{0.8}Fe_{0.2}O_{3-\delta}$-based cathodes for intermediate-temperature solid-oxide fuel cells: A review. *Journal of Power Sources* **2009,** *192* (2), 231-246.

16. Murray, E. P.; Sever, M.; Barnett, S., Electrochemical performance of (La, Sr)(Co, Fe)O_3–(Ce, Gd)O_2 composite cathodes. *Solid State Ionics* **2002,** *148* (1), 27-34.
17. Hwang, H. J.; Moon, J.-W.; Lee, S.; Lee, E. A., Electrochemical performance of LSCF-based composite cathodes for intermediate temperature SOFCs. *Journal of Power Sources* **2005,** *145* (2), 243-248.
18. Oh, D.; Gostovic, D.; Wachsman, E. D., Mechanism of $La_{0.6}Sr_{0.4}Co_{0.2}Fe_{0.8}O_3$ cathode degradation. *Journal of Materials Research* **2012,** *27* (15), 1992-1999.
19. Amow, G.; Davidson, I.; Skinner, S., A comparative study of the Ruddlesden-Popper series, $La_{n+1}Ni_nO_{3n+1}$ (n= 1, 2 and 3), for solid-oxide fuel-cell cathode applications. *Solid State Ionics* **2006,** *177* (13), 1205-1210.
20. Aguadero, A.; Alonso, J.; Escudero, M.; Daza, L., Evaluation of the $La_2Ni_{1-x}Cu_xO_{4+\delta}$ system as SOFC cathode material with 8YSZ and LSGM as electrolytes. *Solid State Ionics* **2008,** *179* (11), 393-400.
21. Shen, Y.; Zhao, H.; Liu, X.; Xu, N., Preparation and electrical properties of Ca-doped $La_2NiO_{4+\delta}$ cathode materials for IT-SOFC. *Physical Chemistry Chemical Physics* **2010,** *12* (45), 15124-15131.
22. Chen, D.; Ran, R.; Zhang, K.; Wang, J.; Shao, Z., Intermediate-temperature electrochemical performance of a polycrystalline $PrBaCo_2O_{5+\delta}$ cathode on samarium-doped ceria electrolyte. *Journal of Power Sources* **2009,** *188* (1), 96-105.
23. Kim, G.; Wang, S.; Jacobson, A.; Reimus, L.; Brodersen, P.; Mims, C., Rapid oxygen ion diffusion and surface exchange kinetics in $PrBaCo_2O_{5+x}$ with a perovskite related structure and ordered A cations. *Journal of Materials Chemistry* **2007,** *17* (24), 2500-2505.
24. Peña-Martínez, J.; Tarancón, A.; Marrero-López, D.; Ruiz-Morales, J., Evaluation of $GdBaCo_2O_{5+\delta}$ as Cathode Material for Doped Lanthanum Gallate Electrolyte IT-SOFCs. *Fuel Cells* **2008,** *8* (5), 351-359.
25. Rondinelli, J. M.; May, S. J.; Freeland, J. W., Control of octahedral connectivity in perovskite oxide heterostructures: An emerging route to multifunctional materials discovery. *MRS bulletin* **2012,** *37* (3), 261-270.
26. Yang, C.; Grimaud, A., Factors Controlling the Redox Activity of Oxygen in Perovskites: From Theory to Application for Catalytic Reactions. *Catalysts* **2017,** *7* (5), 149.
27. Kieslich, G.; Sun, S.; Cheetham, A. K., Solid-state principles applied to organic–inorganic perovskites: new tricks for an old dog. *Chemical Science* **2014,** *5* (12), 4712-4715.
28. Glazer, A., Simple ways of determining perovskite structures. *Acta Crystallographica Section A: Crystal Physics, Diffraction, Theoretical and General Crystallography* **1975,** *31* (6), 756-762.
29. West, A. R., *Solid state chemistry and its applications*. John Wiley & Sons: 2014.
30. Goodenough, J.; Zhou, J.-S., Localized to itinerant electronic transitions in transition-metal oxides with the perovskite structure. *Chemistry of Materials* **1998,** *10* (10), 2980-2993.
31. Cotton, F. A., Chemical applications of group theory. *John Wiley & Sons*: 2008.
32. Mefford, J. T.; Rong, X.; Abakumov, A. M.; Hardin, W. G.; Dai, S.; Kolpak, A. M.; Johnston, K. P.; Stevenson, K. J., Water electrolysis on $La_{1-x}Sr_xCoO_{3-\delta}$ perovskite electrocatalysts. *Nature Communications* **2016,** *7*, 11053.

33. Wang, L.; Merkle, R.; Mastrikov, Y. A.; Kotomin, E. A.; Maier, J., Oxygen exchange kinetics on solid oxide fuel cell cathode materials—general trends and their mechanistic interpretation. *Journal of Materials Research* **2012,** *27* (15), 2000-2008.
34. Mastrikov, Y. A.; Merkle, R.; Heifets, E.; Kotomin, E. A.; Maier, J., Pathways for oxygen incorporation in mixed conducting perovskites: A DFT-based mechanistic analysis for (La, Sr)$MnO_{3-\delta}$. *The Journal of Physical Chemistry C* **2010,** *114* (7), 3017-3027.
35. Kuklja, M.; Kotomin, E. A.; Merkle, R.; Mastrikov, Y. A.; Maier, J., Combined theoretical and experimental analysis of processes determining cathode performance in solid oxide fuel cells. *Physical Chemistry Chemical Physics* **2013,** *15* (15), 5443-5471.
36. Lee, Y.-L.; Kleis, J.; Rossmeisl, J.; Morgan, D., Ab initio energetics of $LaBO_3$ (001) (B= Mn, Fe, Co, and Ni) for solid oxide fuel cell cathodes. *Physical Review B* **2009,** *80* (22), 224101.
37. Choi, Y.; Mebane, D. S.; Lin, M.; Liu, M., Oxygen reduction on $LaMnO_3$-based cathode materials in solid oxide fuel cells. *Chemistry of Materials* **2007,** *19* (7), 1690-1699.
38. Lee, C.-W.; Behera, R. K.; Wachsman, E. D.; Phillpot, S. R.; Sinnott, S. B., Stoichiometry of the $LaFeO_3$ (010) surface determined from first-principles and thermodynamic calculations. *Physical Review B* **2011,** *83* (11), 115418.
39. Caillol, N.; Pijolat, M.; Siebert, E., Investigation of chemisorbed oxygen, surface segregation and effect of post-treatments on $La_{0.8}Sr_{0.2}MnO_3$ powder and screen-printed layers for solid oxide fuel cell cathodes. *Applied Surface Science* **2007,** *253* (10), 4641-4648.
40. Piskunov, S.; Jacob, T.; Spohr, E., Oxygen adsorption at $La_{1-x}Sr_xMnO_3$ (001) surfaces: Predictions from first principles. *Physical Review B* **2011,** *83* (7), 073402.
41. Wang, L.; Merkle, R.; Maier, J., Surface Kinetics and Mechanism of Oxygen Incorporation Into $Ba_{1-x}Sr_xCo_yFe_{1-y}O_{3-\delta}$ SOFC Microelectrodes. *Journal of The Electrochemical Society* **2010,** *157* (12), B1802-B1808.
42. Larsen, E.; La Mar, G. N., The angular overlap model. How to use it and why. *Journal of Chemical Education* **1974,** *51* (10), 633.
43. Zhou, J.-S.; Goodenough, J., Paramagnetic phase in single-crystal $LaMnO_3$. *Physical Review B* **1999,** *60* (22), R15002.
44. Huang, K.; Lee, H. Y.; Goodenough, J. B., Sr-and Ni-Doped $LaCoO_3$ and $LaFeO_3$ perovskites new cathode materials for solid-oxide fuel cells. *Journal of the Electrochemical Society* **1998,** *145* (9), 3220-3227.
45. Senarıs-Rodrıguez, M.; Goodenough, J., Magnetic and transport properties of the system $La_{1-x}Sr_xCoO_{3-\delta}$ ($0< x\leq 0.50$). *Journal of Solid State Chemistry* **1995,** *118* (2), 323-336.
46. Suntivich, J.; Gasteiger, H. A.; Yabuuchi, N.; Nakanishi, H.; Goodenough, J. B.; Shao-Horn, Y., Design principles for oxygen-reduction activity on perovskite oxide catalysts for fuel cells and metal–air batteries. *Nature Chemistry* **2011,** *3* (7), 546.
47. Hwang, J.; Rao, R. R.; Giordano, L.; Katayama, Y.; Yu, Y.; Shao-Horn, Y., Perovskites in catalysis and electrocatalysis. *Science* **2017,** *358* (6364), 751-756.
48. Lee, Y.-L.; Kleis, J.; Rossmeisl, J.; Shao-Horn, Y.; Morgan, D., Prediction of solid oxide fuel cell cathode activity with first-principles descriptors. *Energy & Environmental Science* **2011,** *4* (10), 3966-3970.

49. Jacobs, R.; Mayeshiba, T.; Booske, J.; Morgan, D., Material discovery and design principles for stable, high activity perovskite cathodes for solid oxide fuel cells. *Advanced Energy Materials* **2018**.
50. Lee, Y.-L.; Lee, D.; Wang, X. R.; Lee, H. N.; Morgan, D.; Shao-Horn, Y., Kinetics of oxygen surface exchange on epitaxial Ruddlesden–Popper phases and correlations to first-principles descriptors. *The Journal of Physical Chemistry Letters* **2016,** *7* (2), 244-249.
51. Gwon, O.; Yoo, S.; Shin, J.; Kim, G., Optimization of $La_{1-x}Sr_xCoO_{3-\delta}$ perovskite cathodes for intermediate temperature solid oxide fuel cells through the analysis of crystal structure and electrical properties. *International Journal of Hydrogen Energy* **2014,** *39* (35), 20806-20811.
52. Yang, W.; Zhang, H.; Sun, C.; Liu, L.; Alonso, J.; Fernández-Díaz, M.; Chen, L., Insight into the structure and functional application of the $Sr_{0.95}Ce_{0.05}Coo_{3-\delta}$ cathode for solid oxide fuel cells. *Inorganic Chemistry* **2015,** *54* (7), 3477-3484.
53. James, M.; Cassidy, D.; Wilson, K.; Horvat, J.; Withers, R., Oxygen vacancy ordering and magnetism in the rare earth stabilised perovskite form of "$SrCoO_{3-\delta}$". *Solid State Sciences* **2004,** *6* (7), 655-662.
54. Jiang, L.; Wang, J.; Xiong, X.; Jin, X.; Pei, Q.; Huang, K., Thermal and electrical stability of $Sr_{0.9}Y_{0.1}CoO_{2.5+\delta}$ as a promising cathode for intermediate-temperature solid oxide fuel cells. *Journal of the Electrochemical Society* **2016,** *163* (5), F330-F335.
55. Aguadero, A.; Calle, C. d. l.; Alonso, J.; Escudero, M.; Fernández-Díaz, M.; Daza, L., Structural and electrical characterization of the novel $SrCo_{0.9}Sb_{0.1}O_{3-\delta}$ perovskite: evaluation as a solid oxide fuel cell cathode material. *Chemistry of Materials* **2007,** *19* (26), 6437-6444.
56. Aguadero, A.; Pérez-Coll, D.; Alonso, J.; Skinner, S.; Kilner, J., A new family of Mo-doped $SrCoO_{3-\delta}$ perovskites for application in reversible solid state electrochemical cells. *Chemistry of Materials* **2012,** *24* (14), 2655-2663.
57. Chen, X.; Huang, L.; Wei, Y.; Wang, H., Tantalum stabilized $SrCoO_{3-\delta}$ perovskite membrane for oxygen separation. *Journal of Membrane Science* **2011,** *368* (1-2), 159-164.
58. Wang, J.; Jiang, L.; Xiong, X.; Zhang, C.; Jin, X.; Lei, L.; Huang, K., A broad stability investigation of Nb-doped $SrCoO_{2.5+\delta}$ as a reversible oxygen electrode for intermediate-temperature solid oxide fuel cells. *Journal of The Electrochemical Society* **2016,** *163* (8), F891-F898.
59. Lander, J., The crystal structures of NiO-3BaO, NiO-BaO, $BaNiO_3$ and intermediate phases with composition near $Ba_2Ni_2O_5$; with a note on NiO. *Acta Crystallogr* **1951,** *4* (2), 148-156.
60. Harrison, W. T.; Hegwood, S. L.; Jacobson, A. J., A powder neutron diffraction determination of the structure of $Sr_6Co_5O_{15}$, formerly described as the low-temperature hexagonal form of $SrCoO_{3-x}$. *Journal of the Chemical Society, Chemical Communications* **1995,** (19), 1953-1954.
61. De la Calle, C.; Aguadero, A.; Alonso, J.; Fernández-Díaz, M., Correlation between reconstructive phase transitions and transport properties from $SrCoO_{2.5}$ brownmillerite: A neutron diffraction study. *Solid State Sciences* **2008,** *10* (12), 1924-1935.

62. Karvonen, L.; Valkeapää, M.; Liu, R.-S.; Chen, J.-M.; Yamauchi, H.; Karppinen, M., O-K and Co-L XANES study on oxygen intercalation in perovskite $SrCoO_{3-\delta}$. *Chemistry of Materials* **2009,** *22* (1), 70-76.
63. Muñoz, A.; de La Calle, C.; Alonso, J.; Botta, P.; Pardo, V.; Baldomir, D.; Rivas, J., Crystallographic and magnetic structure of $SrCoO_{2.5}$ brownmillerite: Neutron study coupled with band-structure calculations. *Physical Review B* **2008,** *78* (5), 054404.
64. Le Toquin, R.; Paulus, W.; Cousson, A.; Prestipino, C.; Lamberti, C., Time-resolved in situ studies of oxygen intercalation into $SrCoO_{2.5}$, performed by neutron diffraction and X-ray absorption spectroscopy. *Journal of American Chemical Society* **2006,** *128* (40), 13161-13174.
65. Rodriguez, J.; Gonzalez-Calbet, J.; Grenier, J.; Pannetier, J.; Anne, M., Phase transitions in $Sr_2Co_2O_5$: a neutron thermodiffractometry study. *Solid State Communications* **1987,** *62* (4), 231-234.
66. Hu, S.; Seidel, J., Oxygen content modulation by nanoscale chemical and electrical patterning in epitaxial $SrCoO_{3-\delta}$ ($0< \delta\leq 0.5$) thin films. *Nanotechnology* **2016,** *27* (32), 325301.
67. Hu, S.; Wang, Y.; Cazorla, C.; Seidel, J., Strain-enhanced oxygen dynamics and redox reversibility in topotactic $SrCoO_{3-\delta}$ ($0< \delta\leq 0.5$). *Chemistry of Materials* **2017,** *29* (2), 708-717.
68. Usiskin, R. E.; Davenport, T. C.; Wang, R. Y.; Guan, W.; Haile, S. M., Bulk properties of the oxygen reduction catalyst $SrCo_{0.9}Nb_{0.1}O_{3-\delta}$. *Chemistry of Materials* **2016,** *28* (8), 2599-2608.
69. Yoo, C.-Y.; Park, J. H.; Yun, D. S.; Lee, Y. A.; Yun, K. S.; Lee, J. H.; Yoon, H.; Joo, J. H.; Yu, J. H., Unraveling crystal structure and transport properties of fast ion conducting $SrCo_{0.9}Nb_{0.1}O_{3-\delta}$. *The Journal of Physical Chemistry C* **2016,** *120* (39), 22248-22256.
70. Li, M.; Zhou, W.; Peterson, V. K.; Zhao, M.; Zhu, Z., A comparative study of $SrCo_{0.8}Nb_{0.2}O_{3-\delta}$ and $SrCo_{0.8}Ta_{0.2}O_{3-\delta}$ as low-temperature solid oxide fuel cell cathodes: effect of non-geometry factors on the oxygen reduction reaction. *Journal of Materials Chemistry A* **2015,** *3* (47), 24064-24070.
71. Ai, N.; Jiang, S. P.; Lü, Z.; Chen, K.; Su, W., Nanostructured (Ba, Sr)(Co, Fe) $O_{3-\delta}$ Impregnated (La, Sr) MnO3 Cathode for Intermediate-Temperature Solid Oxide Fuel Cells. *Journal of the Electrochemical Society* **2010,** *157* (7), B1033-B1039.
72. Ren, Y.; Cheng, Y.; Gorte, R. J.; Huang, K., Toward stabilizing Co_3O_4 nanoparticles as an oxygen reduction reaction catalyst for intermediate-temperature SOFCs. *Journal of The Electrochemical Society* **2017,** *164* (10), F3001-F3007.
73. Ding, D.; Li, X.; Lai, S. Y.; Gerdes, K.; Liu, M., Enhancing SOFC cathode performance by surface modification through infiltration. *Energy & Environmental Science* **2014,** *7* (2), 552.
74. Wang, J.; Yang, T.; Lei, L.; Huang, K., Ta-Doped $SrCoO_{3-\delta}$ as a promising bifunctional oxygen electrode for reversible solid oxide fuel cells: a focused study on stability. *Journal of Materials Chemistry A* **2017,** *5* (19), 8989-9002.
75. Li, M.; Zhao, M.; Li, F.; Zhou, W.; Peterson, V. K.; Xu, X.; Shao, Z.; Gentle, I.; Zhu, Z., A Niobium and Tantalum co-doped perovskite cathode for solid oxide fuel cells operating below 500 ºC. *Nature Communications* **2017,** *8*, 13990.

76. Usiskin, R. E.; Davenport, T. C.; Wang, R. Y.; Guan, W.; Haile, S. M., Bulk properties of the oxygen reduction catalyst $SrCo_{0.9}Nb_{0.1}O_{3-\delta}$. *Chemistry of Materials* **2016,** *28* (8), 2599-2608.
77. Yang, W.; Zhang, H.; Sun, C.; Liu, L.; Alonso, J. A.; Fernandez-Diaz, M. T.; Chen, L., Insight into the structure and functional application of the $Sr_{0.95}Ce_{0.05}CoO_{3\text{-delta}}$ cathode for solid oxide fuel cells. *Inorganic Chemistry* **2015,** *54* (7), 3477-84.
78. Li, M.; Zhou, W.; Peterson, V. K.; Zhao, M.; Zhu, Z., A comparative study of $SrCo_{0.8}Nb_{0.2}O_{3-\delta}$ and $SrCo_{0.8}Ta_{0.2}O_{3-\delta}$ as low-temperature solid oxide fuel cell cathodes: effect of non-geometry factors on the oxygen reduction reaction. *Journal of Materials Chemistry A* **2015,** *3* (47), 24064-24070.
79. Yang, W.; Hong, T.; Li, S.; Ma, Z.; Sun, C.; Xia, C.; Chen, L., Perovskite $Sr_{1-x}Ce_xCoO_{3\text{-delta}}$ ($0.05 < x < 0.15$) as superior cathodes for intermediate temperature solid oxide fuel cells. *ACS Applied Materials & Interfaces* **2013,** *5* (3), 1143-8.
80. Istomin, S. Y.; Grins, J.; Svensson, G.; Drozhzhin, O.; Kozhevnikov, V.; Antipov, E.; Attfield, J., Crystal structure of the novel complex cobalt oxide $Sr_{0.7}Y_{0.3}CoO_{2.62}$. *Chemistry of Materials* **2003,** *15* (21), 4012-4020.
81. Li, Y.; Kim, Y. N.; Cheng, J.; Alonso, J. A.; Hu, Z.; Chin, Y.-Y.; Takami, T.; Fernández-Díaz, M. T.; Lin, H.-J.; Chen, C.-T., Oxygen-deficient perovskite $Sr_{0.7}Y_{0.3}CoO_{2.65-\delta}$ as a cathode for intermediate-temperature solid oxide fuel cells. *Chemistry of Materials* **2011,** *23* (22), 5037-5044.
82. Cascos, V.; Martinez-Coronado, R.; Alonso, J.; Fernández-Díaz, M., Visualization by neutron diffraction of 2D oxygen diffusion in the $Sr_{0.7}Ho_{0.3}CoO_{3-\delta}$ cathode for solid-oxide fuel cells. *ACS Applied Materials & Interfaces* **2014,** *6* (12), 9194-9200.
83. Liu, T.; Li, Y.; Goodenough, J. B., $Sr_{0.7}Ho_{0.3}CoO_{3-\delta}$ as a potential cathode material for intermediate-temperature solid oxide fuel cells. *Journal of Power Sources* **2012,** *199*, 161-164.
84. Withers, R.; James, M.; Goossens, D., Atomic ordering in the doped rare earth cobaltates $Ln_{0.33}Sr_{0.67}CoO_{3-\delta}$ (Ln= Y^{3+}, Ho^{3+} and Dy^{3+}). *Journal of Solid State Chemistry* **2003,** *174* (1), 198-208.
85. James, M.; Avdeev, M.; Barnes, P.; Morales, L.; Wallwork, K.; Withers, R., Orthorhombic superstructures within the rare earth strontium-doped cobaltate perovskites: $Ln_{1-x}Sr_xCoO_{3-\delta}$ (Ln=Y^{3+}, Dy^{3+}–Yb^{3+}; $0.750 \leqslant x \leqslant 0.875$). *Journal of Solid State Chemistry* **2007,** *180* (8), 2233-2247.
86. Khalyavin, D. D.; Chapon, L. C.; Suard, E.; Parker, J. E.; Thompson, S. P.; Yaremchenko, A. A.; Kharton, V. V., Complex room-temperature ferrimagnetism induced by zigzag stripes of oxygen vacancies in$Sr_3YCo_4O_{10+\delta}$. *Physical Review B* **2011,** *83* (14).
87. Yang, T.; Mattick, V. F.; Chen, Y.; An, K.; Ma, D.; Huang, K., Crystal Structure and Transport Properties of Oxygen-Deficient Perovskite $Sr_{0.9}Y_{0.1}CoO_{3-\delta}$. *ACS Applied Energy Materials* **2018,** *1* (2), 822-832.
88. Gong, Y.; Sun, C.; Huang, Q.-a.; Alonso, J. A.; Fernández-Díaz, M. T.; Chen, L., Dynamic octahedral breathing in oxygen-deficient $Ba_{0.9}Co_{0.7}Fe_{0.2}Nb_{0.1}O_{3-\delta}$ perovskite performing as a cathode in intermediate-temperature SOFC. *Inorganic Chemistry* **2016,** *55* (6), 3091-3097.
89. Lu, Y.; López, C. A.; Wang, J.; Alonso, J. A.; Sun, C., Insight into the structure and functional application of Mg-doped $Na_{0.5}Bi_{0.5}TiO_3$ electrolyte for solid oxide fuel cells. *Journal of Alloys and Compounds* **2018,** *752*, 213-219.

90. An, K., VDRIVE-Data reduction and interactive visualization software for event mode neutron diffraction. *ORNL Report No. ORNL-TM-2012-621, Oak Ridge National Laboratory, Oak Ridge, TN* **2012**.
91. Chen, Y.; Rangasamy, E.; dela Cruz, C. R.; Liang, C.; An, K., A study of suppressed formation of low-conductivity phases in doped $Li_7La_3Zr_2O_{12}$ garnets by in situ neutron diffraction. *Journal of Materials Chemistry A* **2015,** *3* (45), 22868-22876.
92. Larson, A.; Von Dreele, R., General Structure Analysis System, LANSCE, MS-H805, Los Alamos, New Mexico 1994; b) BH Toby. *Journal of Applied Crystallography* **2001,** *34*, 210-213.
93. Toby, B. H., EXPGUI, a graphical user interface for GSAS. *Journal of Applied Crystallography* **2001,** *34* (2), 210-213.
94. Le Bail, A., Whole powder pattern decomposition methods and applications: A retrospection. *Powder Diffraction* **2005,** *20* (4), 316-326.
95. Momma, K.; Izumi, F., VESTA 3 for three-dimensional visualization of crystal, volumetric and morphology data. *Journal of Applied Crystallography* **2011,** *44* (6), 1272-1276.
96. Sears, V. F., Neutron scattering lengths and cross sections. *Neutron News* **1992,** *3* (3), 26-37.
97. Yang, T.; Wang, J.; Chen, Y.; An, K.; Ma, D.; Vogt, T.; Huang, K., A combined variable-temperature neutron diffraction and thermogravimetric analysis study on a promising oxygen electrode, $SrCo_{0.9}Nb_{0.1}O_{3-\delta}$, for reversible solid oxide fuel cells. *ACS Applied Materials & Interfaces* **2017,** *9* (40), 34855-34864.
98. Sarno, C.; Yang, T.; Di Bartolomeo, E.; Huq, A.; Huang, K.; McIntosh, S., Oxygen vacancy localization and anisotropic oxygen anion transport in $Sr_{1-x}Y_xCoO_{3-\delta}$ (x= 0.1, 0.2) under solid oxide fuel cell cathode conditions. *Solid State Ionics* **2018,** *321*, 34-42.
99. Rupasov, D.; Chroneos, A.; Parfitt, D.; Kilner, J.; Grimes, R.; Istomin, S. Y.; Antipov, E., Oxygen diffusion in $Sr_{0.75}Y_{0.25}CoO_{2.625}$: A molecular dynamics study. *Physical Review B* **2009,** *79* (17), 172102.
100. McIntosh, S.; Vente, J. F.; Haije, W. G.; Blank, D. H.; Bouwmeester, H. J., Oxygen stoichiometry and chemical expansion of $Ba_{0.5}Sr_{0.5}Co_{0.8}Fe_{0.2}O_{3-\delta}$ measured by in situ neutron diffraction. *Chemistry of Materials* **2006,** *18* (8), 2187-2193.
101. Martínez-Coronado, R.; Alonso, J.; Fernández-Díaz, M., $SrMo_{0.9}Co_{0.1}O_{3-\delta}$: A potential anode for intermediate-temperature solid-oxide fuel cells (IT-SOFC). *Journal of Power Sources* **2014,** *258*, 76-82.
102. Perry, N. H.; Ishihara, T., Roles of bulk and surface chemistry in the oxygen exchange kinetics and related properties of mixed conducting perovskite oxide electrodes. *Materials* **2016,** *9* (10), 858.
103. Hollmann, N.; Hu, Z.; Valldor, M.; Maignan, A.; Tanaka, A.; Hsieh, H.; Lin, H.-J.; Chen, C.; Tjeng, L., Electronic and magnetic properties of the kagome systems $YBaCo_4O_7$ and $YBaCo_3MO_7$ (M= Al, Fe). *Physical Review B* **2009,** *80* (8), 085111.
104. Hu, Z.; Wu, H.; Haverkort, M.; Hsieh, H.; Lin, H.-J.; Lorenz, T.; Baier, J.; Reichl, A.; Bonn, I.; Felser, C., Different look at the spin state of Co^{3+} Ions in a CoO_5 pyramidal coordination. *Physical Review Letters* **2004,** *92* (20), 207402.

105. Mamtsev, D.; Murzakaev, A., High resolution electron microscopy study of phase composition of yttrium oxide nanoparticles. *Russian Physics Journal* **2015,** *58* (6), 781-784.
106. Jauch, W.; Reehuis, M.; Bleif, H.; Kubanek, F.; Pattison, P., Crystallographic symmetry and magnetic structure of CoO. *Physical Review B* **2001,** *64* (5), 052102.
107. Takeda, Y.; Kanno, R.; Noda, M.; Tomida, Y.; Yamamoto, O., Cathodic polarization phenomena of perovskite oxide electrodes with stabilized zirconia. *Journal of The Electrochemical Society* **1987,** *134* (11), 2656-2661.
108. Shao, Z.; Haile, S. M., A high-performance cathode for the next generation of solid-oxide fuel cells. In *Materials for Sustainable Energy: A Collection of Peer-Reviewed Research and Review Articles from Nature Publishing Group*, World Scientific: 2011; pp 255-258.
109. Ren, C.; Gan, Y.; Lee, M.; Yang, C.; He, F.; Jiang, Y.; Dong, G.; Green, R. D.; Xue, X., Fabrication and characterization of high performance intermediate temperature micro-tubular solid oxide fuel cells. *Journal of The Electrochemical Society* **2016,** *163* (9), F1115-F1123.
110. Zhou, W.; Shao, Z.; Ran, R.; Jin, W.; Xu, N., A novel efficient oxide electrode for electrocatalytic oxygen reduction at 400–600 °C. *Chemical Communications* **2008,** (44), 5791-5793.
111. Zhu, Y.; Chen, Z. G.; Zhou, W.; Jiang, S.; Zou, J.; Shao, Z., An A-Site-deficient perovskite offers high activity and stability for low-temperature solid-oxide fuel cells. *ChemSusChem* **2013,** *6* (12), 2249-2254.
112. Cascos, V.; Martínez-Coronado, R.; Alonso, J., New Nb-doped $SrCo_{1-x}Nb_xO_{3-\delta}$ perovskites performing as cathodes in solid-oxide fuel cells. *International Journal of Hydrogen Energy* **2014,** *39* (26), 14349-14354.
113. Zhou, W.; Jin, W.; Zhu, Z.; Shao, Z., Structural, electrical and electrochemical characterizations of $SrNb_{0.1}Co_{0.9}O_{3-\delta}$ as a cathode of solid oxide fuel cells operating below 600° C. *International Journal of Hydrogen Energy* **2010,** *35* (3), 1356-1366.
114. Zhang, K.; Ran, R.; Ge, L.; Shao, Z.; Jin, W.; Xu, N., Systematic investigation on new $SrCo_{1-y}Nb_yO_{3-\delta}$ ceramic membranes with high oxygen semi-permeability. *Journal of Membrane Science* **2008,** *323* (2), 436-443.
115. Chen, D.; Chen, C.; Gao, Y.; Zhang, Z.; Shao, Z.; Ciucci, F., Evaluation of pulsed laser deposited $SrNb_{0.1}Co_{0.9}O_{3-\delta}$ thin films as promising cathodes for intermediate-temperature solid oxide fuel cells. *Journal of Power Sources* **2015,** *295*, 117-124.
116. Wang, F.; Zhou, Q.; He, T.; Li, G.; Ding, H., Novel $SrCo_{1-y}Nb_yO_{3-\delta}$ cathodes for intermediate-temperature solid oxide fuel cells. *Journal of Power Sources* **2010,** *195* (12), 3772-3778.
117. Zhu, Y.; Lin, Y.; Shen, X.; Sunarso, J.; Zhou, W.; Jiang, S.; Su, D.; Chen, F.; Shao, Z., Influence of crystal structure on the electrochemical performance of A-site-deficient $Sr_{1-x}Nb_{0.1}Co_{0.9}O_{3-\delta}$ perovskite cathodes. *RSC Advances* **2014,** *4* (77), 40865-40872.
118. Zeng, P.; Shao, Z.; Liu, S.; Xu, Z. P., Influence of M cations on structural, thermal and electrical properties of new oxygen selective membranes based on $SrCo_{0.95}M_{0.05}O_{3-\delta}$ perovskite. *Separation and Purification Technology* **2009,** *67* (3), 304-311.
119. Chen, Y.; Rangasamy, E.; Liang, C.; An, K., Origin of high Li+ conduction in doped $Li_7La_3Zr_2O_{12}$ garnets. *Chemistry of Materials* **2015,** *27* (16), 5491-5494.
120. Larson, A. C.; Von Dreele, R. B., Gsas. *Report lAUR* **1994**, 86-748.

121. Toby, B. H., CMPR–a powder diffraction toolkit. *Journal of Applied Crystallography* **2005,** *38* (6), 1040-1041.
122. Xie, C.; Nie, Y.; Wells, B.; Budnick, J.; Hines, W.; Dabrowski, B., Magnetic phase separation in $SrCoO_x$ ($2.5 \leq x \leq 3$). *Applied Physics Letters* **2011,** *99* (5), 052503.
123. Callori, S.; Hu, S.; Bertinshaw, J.; Yue, Z.; Danilkin, S.; Wang, X.; Nagarajan, V.; Klose, F.; Seidel, J.; Ulrich, C., Strain-induced magnetic phase transition in $SrCoO_{3-\delta}$ thin films. *Physical Review B* **2015,** *91* (14), 140405.
124. McCusker, L.; Von Dreele, R.; Cox, D.; Louër, D.; Scardi, P., Rietveld refinement guidelines. *Journal of Applied Crystallography* **1999,** *32* (1), 36-50.
125. Aguadero, A.; Alonso, J. A.; Pérez-Coll, D.; de la Calle, C.; Fernández-Díaz, M. a. T.; Goodenough, J. B., $SrCo_{0.95}Sb_{0.05}O_{3-\delta}$ as cathode material for high power density solid oxide fuel cells. *Chemistry of Materials* **2009,** *22* (3), 789-798.
126. Jiang, L.; Wang, J.; Xiong, X.; Jin, X.; Pei, Q.; Huang, K., Thermal and electrical stability of $Sr_{0.9}Y_{0.1}CoO_{2.5+\delta}$ as a promising cathode for intermediate-temperature solid oxide fuel cells. *Journal of The Electrochemical Society* **2016,** *163* (5), F330-F335.
127. Maier, J., Physical chemistry of ionic materials: ions and electrons in solids. *John Wiley & Sons*: 2004.
128. Wang, J.; Jin, X.; Huang, K., A new defect chemistry model for Nb-doped $SrCoO_{2.5+\delta}$: The role of oxygen interstitials and delocalized-to-localized electron holes. *Journal of Solid State Chemistry* **2017,** *246*, 97-106.
129. Brown, I.; Altermatt, D., Bond-valence parameters obtained from a systematic analysis of the inorganic crystal structure database. *Acta Crystallographica Section B: Structural Science* **1985,** *41* (4), 244-247.
130. Green, R.; Vogt, T., Structures and self-activating photoluminescent properties of $Sr_{3-x}A_xGaO_4F$ (A= Ba, Ca) materials. *Journal of Solid State Chemistry* **2012,** *194*, 375-384.
131. Jahn, H. A.; Teller, E., Stability of polyatomic molecules in degenerate electronic states-I—Orbital degeneracy. *Proceedings of the Royal Society of London A* **1937,** *161* (905), 220-235.
132. Yashima, M.; Tsuji, T., Structural investigation of the cubic perovskite-type doped lanthanum cobaltite $La_{0.6}Sr_{0.4}CoO_{3-\delta}$ at 1531 K: possible diffusion path of oxygen ions in an electrode material. *Journal of Applied Crystallography* **2007,** *40* (6), 1166-1168.
133. Yashima, M.; Nomura, K.; Kageyama, H.; Miyazaki, Y.; Chitose, N.; Adachi, K., Conduction path and disorder in the fast oxide-ion conductor $(La_{0.8}Sr_{0.2})(Ga_{0.8}Mg_{0.15}Co_{0.05})O_{2.8}$. *Chemical Physical Letters* **2003,** *380* (3-4), 391-396.
134. Shannon, R. D., Revised effective ionic radii and systematic studies of interatomic distances in halides and chalcogenides. *Acta crystallographica section A: crystal physics, diffraction, theoretical and general crystallography* **1976,** *32* (5), 751-767.
135. Voorhoeve, R.; Remeika, J.; Trimble, L., Defect chemistry and catalysis in oxidation and reduction over perovskite-type oxides. *Annals of the New York Academy of Sciences* **1976,** *272* (1), 3-21.
136. Li, S.; Jin, W.; Huang, P.; Xu, N.; Shi, J.; Lin, Y.; Hu, M. Z.-C.; Payzant, E. A., Comparison of oxygen permeability and stability of perovskite type $La_{0.2}A_{0.8}Co_{0.2}Fe_{0.8}O_{3-\delta}$ (A= Sr, Ba, Ca) membranes. *Industrial & Engineering Chemistry Research* **1999,** *38* (8), 2963-2972.

137. Pauling, L. Nature of the chemical bond and the structure of molecules and crystals: anintroduction to modern structural chemistry; 1960.
138. Matsunaga, N.; Rogers, D. W.; Zavitsas, A. A., Pauling's electronegativity equation and a new corollary accurately predict bond dissociation enthalpies and enhance current understanding of the nature of the chemical bond. *The Journal of Organic Chemistry* **2003,** *68* (8), 3158-3172.
139. Huq, A.; Hodges, J. P.; Gourdon, O.; Heroux, L., Powgen: A third-generation high-resolution high-throughput powder diffraction instrument at the Spallation Neutron Source. *Z. Kristallogr. Proc* **2011,** *1*, 127-135.
140. Zhao, H.; Xu, N.; Cheng, Y.; Wei, W.; Chen, N.; Ding, W.; Lu, X.; Li, F., Investigation of mixed conductor $BaCo_{0.7}Fe_{0.3-x}Y_xO_{3-\delta}$ with high oxygen permeability. *The Journal of Physical Chemistry C* **2010,** *114* (41), 17975-17981.
141. Shen, Y.; Wang, F.; Ma, X.; He, T., $SrCo_{1-y}Ti_yO_{3-\delta}$ as potential cathode materials for intermediate-temperature solid oxide fuel cells. *Journal of Power Sources* **2011,** *196* (18), 7420-7425.
142. Teraoka, Y.; Zhang, H.-M.; Furukawa, S.; Yamazoe, N., Oxygen permeation through perovskite-type oxides. *Chemistry Letters* **1985,** *14* (11), 1743-1746.
143. Chen, C.; Bouwmeester, H. J.; Van Doorn, R.; Kruidhof, H.; Burggraaf, A., Oxygen permeation of $La_{0.3}Sr_{0.7}CoO_{3-\delta}$. *Solid State Ionics* **1997,** *98* (1-2), 7-13.
144. Zeng, Y.; Lin, Y.; Swartz, S., Perovskite-type ceramic membrane: synthesis, oxygen permeation and membrane reactor performance for oxidative coupling of methane. *Journal of Membrane Science* **1998,** *150* (1), 87-98.
145. Shao, Z.; Yang, W.; Cong, Y.; Dong, H.; Tong, J.; Xiong, G., Investigation of the permeation behavior and stability of a $Ba_{0.5}Sr_{0.5}Co_{0.8}Fe_{0.2}O_{3-\delta}$ oxygen membrane. *Journal of Membrane Science* **2000,** *172* (1-2), 177-188.
146. Cheng, Y.; Zhao, H.; Teng, D.; Li, F.; Lu, X.; Ding, W., Investigation of Ba fully occupied A-site $BaCo_{0.7}Fe_{0.3-x}Nb_xO_{3-\delta}$ perovskite stabilized by low concentration of Nb for oxygen permeation membrane. *Journal of Membrane Science* **2008,** *322* (2), 484-490.
147. Fang, W.; Liang, F.; Cao, Z.; Steinbach, F.; Feldhoff, A., A mixed ionic and electronic conducting dual-phase membrane with high oxygen permeability. *Angewandte Chemie International Edition* **2015,** *54* (16), 4847-4850.
148. Qiu, L.; Lee, T.; Liu, L.-M.; Yang, Y.; Jacobson, A., Oxygen permeation studies of $SrCo_{0.8}Fe_{0.2}O_{3-\delta}$. *Solid State Ionics* **1995,** *76* (3-4), 321-329.
149. Teraoka, Y.; Honbe, Y.; Ishii, J.; Furukawa, H.; Moriguchi, I., Catalytic effects in oxygen permeation through mixed-conductive LSCF perovskite membranes. *Solid State Ionics* **2002,** *152*, 681-687.
150. Jin, Y.; Meng, X.; Meng, B.; Yang, N.; Zhang, C., Simulation of oxygen permeation through $La_{0.6}Sr_{0.4}Co_{0.2}Fe_{0.8}O_{3-\delta}$ tubular membrane reactor with POM reactions. *International Journal of Hydrogen Energy* **2016,** *41* (39), 17399-17407.
151. Hayamizu, Y.; Kato, M.; Takamura, H., Effects of surface modification on the oxygen permeation of $Ba_{0.5}Sr_{0.5}Co_{0.8}Fe_{0.2}O_{3-\delta}$ membrane. *Journal of Membrane Science* **2014,** *462*, 147-152.
152. Yan, A.; Maragou, V.; Arico, A.; Cheng, M.; Tsiakaras, P., Investigation of a $Ba_{0.5}Sr_{0.5}Co_{0.8}Fe_{0.2}O_{3-\delta}$ based cathode SOFC: II. The effect of CO_2 on the chemical stability. *Applied Catalysis B: Environmental* **2007,** *76* (3-4), 320-327.

153. Engels, S.; Markus, T.; Modigell, M.; Singheiser, L., Oxygen permeation and stability investigations on MIEC membrane materials under operating conditions for power plant processes. *Journal of Membrane Science* **2011,** *370* (1-2), 58-69.
154. Tan, X.; Liu, N.; Meng, B.; Sunarso, J.; Zhang, K.; Liu, S., Oxygen permeation behavior of $La_{0.6}Sr_{0.4}Co_{0.8}Fe_{0.2}O_3$ hollow fibre membranes with highly concentrated CO_2 exposure. *Journal of Membrane Science* **2012,** *389*, 216-222.
155. Luo, H.; Jiang, H.; Efimov, K.; Caro, J.; Wang, H., Influence of the preparation methods on the microstructure and oxygen permeability of a CO_2-stable dual phase membrane. *AIChE Journal* **2011,** *57* (10), 2738-2745.
156. Luo, H.; Efimov, K.; Jiang, H.; Feldhoff, A.; Wang, H.; Caro, J., CO_2-stable and cobalt-free dual-phase membrane for oxygen separation. *Angewandte Chemie International Edition* **2011,** *50* (3), 759-763.
157. van Hassel, B. A.; Kawada, T.; Sakai, N.; Yokokawa, H.; Dokiya, M.; Bouwmeester, H. J., Oxygen permeation modelling of perovskites. *Solid State Ionics* **1993,** *66* (3-4), 295-305.
158. Xu, S. J.; Thomson, W. J., Oxygen permeation rates through ion-conducting perovskite membranes. *Chemical Engineer Science* **1999,** *54* (17), 3839-3850.
159. Kim, S.; Yang, Y.; Jacobson, A.; Abeles, B., Diffusion and surface exchange coefficients in mixed ionic electronic conducting oxides from the pressure dependence of oxygen permeation. *Solid State Ionics* **1998,** *106* (3-4), 189-195.
160. Behrouzifar, A.; Asadi, A. A.; Mohammadi, T.; Pak, A., Experimental investigation and mathematical modeling of oxygen permeation through dense $Ba_{0.5}Sr_{0.5}Co_{0.8}Fe_{0.2}O_{3-\delta}$ (BSCF) perovskite-type ceramic membranes. *Ceramics International* **2012,** *38* (6), 4797-4811.
161. Zhu, Y.; Li, W.; Liu, Y.; Zhu, X.; Yang, W., Selection of oxygen permeation models for different mixed ionic-electronic conducting membranes. *AIChE Journal* **2017,** *63* (9), 4043-4053.
162. Kruidhof, H.; Bouwmeester, H. J.; Doorn, R. v.; Burggraaf, A., Influence of order-disorder transitions on oxygen permeability through selected nonstoichiometric perovskite-type oxides. *Solid State Ionics* **1993,** *63*, 816-822.
163. Ishigaki, T.; Yamauchi, S.; Kishio, K.; Mizusaki, J.; Fueki, K., Diffusion of oxide ion vacancies in perovskite-type oxides. *Journal of Solid State Chemistry* **1988,** *73* (1), 179-187.
164. Newman, J.; Thomas-Alyea, K. E., Electrochemical systems. *John Wiley & Sons*: 2012.
165. Gellings, P. J.; Bouwmeester, H., Handbook of solid state electrochemistry. *CRC press*: 1997.
166. Lin, Y. S.; Wang, W.; Han, J., Oxygen permeation through thin mixed-conducting solid oxide membranes. *AIChE journal* **1994,** *40* (5), 786-798.
167. Zhu, X.; Liu, H.; Cong, Y.; Yang, W., Permeation model and experimental investigation of mixed conducting membranes. *AIChE Journal* **2012,** *58* (6), 1744-1754.
168. Zhu, X.; Yang, W., Mixed conducting ceramic membranes. *Springer*: 2017.
169. Wang, J.; Jin, X.; Huang, K., A new defect chemistry model for Nb-doped $SrCoO_{2.5+\delta}$: the role of oxygen interstitials and delocalized-to-localized electron holes. *Journal of Solid State Chemistry* **2017,** *246*, 97-106.

170. Jin, X.; Wang, J.; Huang, K., Defect chemistry and transport properties of $SrCo_{1-x}Ta_xO_{2.5+\delta}$ as a promising oxygen electrocatalyst for reversible solid oxide fuel cells. *Solid State Ionics* **2017,** *309*, 48-57.
171. Maier, J., On the correlation of macroscopic and microscopic rate constants in solid state chemistry. *Solid State Ionics* **1998,** *112* (3), 197-228.
172. Wang, J.; Yang, T.; Lei, L.; Huang, K., Ta-Doped $SrCoO_{3-\delta}$ as a promising bifunctional oxygen electrode for reversible solid oxide fuel cells: a focused study on stability. *Journal of Materials Chemistry A* **2017,** *5* (19), 8989-9002.
173. Jin, X.; White, R. E.; Huang, K., Simulating charge transport in solid oxide mixed ionic and electronic conductors: Nernst-Planck Theory vs Modified Fick's Law. *Journal of The Electrochemical Society* **2016,** *163* (13), A2702-A2719.
174. Jin, X.; Wang, J.; Jiang, L.; White, R. E.; Huang, K., A finite length cylinder model for mixed oxide-ion and electron conducting cathodes suited for intermediate-temperature solid oxide fuel cells. *Journal of the Electrochemical Society* **2016,** *163* (6), F548-F563.
175. Nagai, T.; Ito, W.; Sakon, T., Relationship between cation substitution and stability of perovskite structure in $SrCoO_{3-\delta}$-based mixed conductors. *Solid State Ionics* **2007,** *177* (39-40), 3433-3444.
176. Cotton, F. A., Chemical applications of group theory. *John Wiley & Sons*: 2003.
177. Miessler, G. L.; Tarr, D., Inorganic Chemistry, 2011. *Pearson Education*.
178. Merkle, R.; Maier, J.; Bouwmeester, H. J., A linear free energy relationship for gas-solid interactions: correlation between surface rate constant and diffusion coefficient of oxygen tracer exchange for electron-rich perovskites. *Angewandte Chemie International Edition* **2004,** *43* (38), 5069-5073.
179. Yakovlev, S.; Yoo, C.-Y.; Fang, S.; Bouwmeester, H. J., Phase transformation and oxygen equilibration kinetics of pure and Zr-doped $Ba_{0.5}Sr_{0.5}Co_{0.8}Fe_{0.2}O_{3-\delta}$ perovskite oxide probed by electrical conductivity relaxation. *Applied physics letters* **2010,** *96* (25), 254101.
180. Niedrig, C.; Wagner, S. F.; Menesklou, W.; Baumann, S.; Ivers-Tiffée, E., Oxygen equilibration kinetics of mixed-conducting perovskites BSCF, LSCF, and PSCF at 900° C determined by electrical conductivity relaxation. *Solid State Ionics* **2015,** *283*, 30-37.
181. Chen, D.; Chen, C.; Zhang, Z.; Baiyee, Z. M.; Ciucci, F.; Shao, Z., Compositional engineering of perovskite oxides for highly efficient oxygen reduction reactions. *ACS Applied Materials & Interfaces* **2015,** *7* (16), 8562-8571.
182. Zhao, J.; Sunarso, J.; Zhou, W.; Shao, Z.; Ran, R.; Liu, S., A Comparative Structure and Performance Study of $La_{1-x}Sr_xCoO_{3-\delta}$ and $La_{1-x}Sr_xCo_{0.9}Nb_{0.1}O_{3-\delta}$ (x= 0.5, 0.7, 0.9, and 1.0) Oxygen Permeable Mixed Conductors. *Journal of The Electrochemical Society* **2011,** *158* (3), H299-H304.
183. Weppner, W.; Huggins, R. A., Determination of the kinetic parameters of mixed-conducting electrodes and application to the system Li3Sb. *Journal of The Electrochemical Society* **1977,** *124* (10), 1569-1578.
184. Deng, Z.; Yang, W.; Liu, W.; Chen, C., Relationship between transport properties and phase transformations in mixed-conducting oxides. *Journal of Solid State Chemistry* **2006,** *179* (2), 362-369.

185. Chen, Z.; Shao, Z.; Ran, R.; Zhou, W.; Zeng, P.; Liu, S., A dense oxygen separation membrane with a layered morphologic structure. *Journal of Membrane Science* **2007,** *300* (1-2), 182-190.
186. Stevenson, J.; Armstrong, T.; Carneim, R.; Pederson, L. R.; Weber, W., Electrochemical properties of mixed conducting perovskites $La_{1-x}m_xCo_{1-y}Fe_yO_{3-\delta}$ (m= Sr, Ba, Ca). *Journal of the Electrochemical Society* **1996,** *143* (9), 2722-2729.
187. Mizusaki, J.; Mima, Y.; Yamauchi, S.; Fueki, K.; Tagawa, H., Nonstoichiometry of the perovskite-type oxides $La_{1-x}Sr_xCoO_{3-\delta}$. *Journal of Solid State Chemistry* **1989,** *80* (1), 102-111.
188. van Hassel, B. A.; Kawada, T.; Sakai, N.; Yokokawa, H.; Dokiya, M., Oxygen permeation modelling of $La_{1-y}Ca_yCrO_{3-\delta}$. *Solid State Ionics* **1993,** *66* (1-2), 41-47.
189. Zener, C., Interaction between the d-shells in the transition metals. II. Ferromagnetic compounds of manganese with perovskite structure. *Physical Review* **1951,** *82* (3), 403.
190. Mefford, J. T.; Rong, X.; Abakumov, A. M.; Hardin, W. G.; Dai, S.; Kolpak, A. M.; Johnston, K. P.; Stevenson, K. J., Water electrolysis on $La_{1-x}Sr_xCoO_{3-\delta}$ perovskite electrocatalysts. *Nature Communications* **2016,** *7*.
191. Duan, Y.; Sun, S.; Xi, S.; Ren, X.; Zhou, Y.; Zhang, G.; Yang, H.; Du, Y.; Xu, Z. J., Tailoring the Co 3d-O 2p covalency in $LaCoO_3$ by Fe substitution to promote oxygen evolution reaction. *Chemistry of Materials* **2017,** *29* (24), 10534-10541.
192. Wachsman, E. D.; Lee, K. T., Lowering the temperature of solid oxide fuel cells. *Science* **2011,** *334* (6058), 935-939.
193. Ahn, J. S.; Yoon, H.; Lee, K.; Camaratta, M.; Wachsman, E., Performance of IT-SOFC with $Ce_{0.9}Gd_{0.1}O_{1.95}$ functional layer at the interface of $Ce_{0.9}Gd_{0.1}O_{1.95}$ electrolyte and Ni-$Ce_{0.9}Gd_{0.1}O_{1.95}$ anode. *Fuel Cells* **2009,** *9* (5), 643-649.
194. Carpanese, M.; Clematis, D.; Bertei, A.; Giuliano, A.; Sanson, A.; Mercadelli, E.; Nicolella, C.; Barbucci, A., Understanding the electrochemical behaviour of LSM-based SOFC cathodes. Part I—experimental and electrochemical. *Solid State Ionics* **2017,** *301*, 106-115.
195. Chen, X.; Yu, J.; Adler, S. B., Thermal and chemical expansion of Sr-doped lanthanum cobalt oxide ($La_{1-x}Sr_xCoO_{3-\delta}$). *Chemistry of Materials* **2005,** *17* (17), 4537-4546.
196. Yaremchenko, A.; Mikhalev, S.; Kravchenko, E.; Frade, J., Thermochemical expansion of mixed-conducting (Ba, Sr)$Co_{0.8}Fe_{0.2}O_{3-\delta}$ ceramics. *Journal of the European Ceramic Society* **2014,** *34* (3), 703-715.
197. Cetin, D.; Poizeau, S.; Pietras, J.; Gopalan, S., Decomposition of La_2NiO_4 in $Sm_{0.2}Ce_{0.8}O_2$-La_2NiO_4 composites for solid oxide fuel cell applications. *Solid State Ionics* **2017,** *300*, 91-96.
198. Craciun, R.; Park, S.; Gorte, R.; Vohs, J.; Wang, C.; Worrell, W., A novel method for preparing anode cermets for solid oxide fuel cells. *Journal of The Electrochemical Society* **1999,** *146* (11), 4019-4022.
199. Vohs, J. M.; Gorte, R. J., High-performance SOFC cathodes prepared by infiltration. *Advanced Materials* **2009,** *21* (9), 943-956.
200. Ding, D.; Li, X.; Lai, S. Y.; Gerdes, K.; Liu, M., Enhancing SOFC cathode performance by surface modification through infiltration. *Energy & Environmental Science* **2014,** *7* (2), 552-575.

201. Huang, Y.-L.; Hussain, A. M.; Wachsman, E. D., Nanoscale cathode modification for high performance and stable low-temperature solid oxide fuel cells (SOFCs). *Nano Energy* **2018,** *49*, 186-192.
202. Lou, X.; Wang, S.; Liu, Z.; Yang, L.; Liu, M., Improving $La_{0.6}Sr_{0.4}Co_{0.2}Fe_{0.8}O_{3-\delta}$ cathode performance by infiltration of a $Sm_{0.5}Sr_{0.5}CoO_{3-\delta}$ coating. *Solid State Ionics* **2009,** *180* (23-25), 1285-1289.
203. Si, F.; Zhang, G.; Huang, K., Communication—Improving intermediate-temperature performance of a screen-printed LSCF cathode with infiltrated LSCF nanoparticles. *Journal of The Electrochemical Society* **2016,** *163* (7), F626-F628.
204. Si, F.; Shao, L.; Kang, X.; Qin, C.; Huang, K.; Fu, X.; Luo, J., Infiltrated $Sr_{0.9}Y_{0.1}CoO_{2.5+\delta}$ nanoparticles as a cathode material for solid oxide fuel cells operated at 450–650° C. *International Journal of Hydrogen Energy* **2018**.
205. Tsvetkov, N.; Lu, Q.; Sun, L.; Crumlin, E. J.; Yildiz, B., Improved chemical and electrochemical stability of perovskite oxides with less reducible cations at the surface. *Nature Materials* **2016,** *15* (9), 1010.
206. Gong, Y.; Palacio, D.; Song, X.; Patel, R. L.; Liang, X.; Zhao, X.; Goodenough, J. B.; Huang, K., Stabilizing nanostructured solid oxide fuel cell cathode with atomic layer deposition. *Nano letters* **2013,** *13* (9), 4340-4345.
207. Jung, W.; Tuller, H. L., Investigation of surface Sr segregation in model thin film solid oxide fuel cell perovskite electrodes. *Energy & Environmental Science* **2012,** *5* (1), 5370-5378.
208. Lee, W.; Han, J. W.; Chen, Y.; Cai, Z.; Yildiz, B., Cation size mismatch and charge interactions drive dopant segregation at the surfaces of manganite perovskites. *Journal of the American Chemical Society* **2013,** *135* (21), 7909-7925.
209. Wang, H.; Yakal-Kremski, K. J.; Yeh, T.; Rupp, G. M.; Limbeck, A.; Fleig, J.; Barnett, S. A., Mechanisms of performance degradation of (La, Sr)(Co, Fe)$O_{3-\delta}$ solid oxide fuel cell cathodes. *Journal of The Electrochemical Society* **2016,** *163* (6), F581-F585.
210. Pişkin, F.; Bliem, R.; Yildiz, B., Effect of crystal orientation on the segregation of aliovalent dopants at the surface of $La_{0.6}Sr_{0.4}CoO_3$. *Journal of Materials Chemistry A* **2018**.
211. Li, M.; Zhou, W.; Zhu, Z., Highly CO_2-tolerant cathode for intermediate-temperature solid oxide fuel cells: Samarium-doped Ceria-protected $SrCo_{0.85}Ta_{0.15}O_{3-\delta}$ hybrid. *ACS Applied Materials & Interfaces* **2017,** *9* (3), 2326-2333.
212. Li, M.; Zhao, M.; Li, F.; Zhou, W.; Peterson, V. K.; Xu, X.; Shao, Z.; Gentle, I.; Zhu, Z., A Niobium and Tantalum co-doped perovskite cathode for solid oxide fuel cells operating below 500 °C. *Nature Communications* **2017,** *8*, 13990.
213. Shah, M.; Barnett, S., Solid oxide fuel cell cathodes by infiltration of $La_{0.6}Sr_{0.4}Co_{0.2}Fe_{0.8}O_{3-\delta}$ into Gd-Doped Ceria. *Solid State Ionics* **2008,** *179* (35-36), 2059-2064.
214. Chen, D.; Yang, G.; Ciucci, F.; Tadé, M. O.; Shao, Z., 3D core–shell architecture from infiltration and beneficial reactive sintering as highly efficient and thermally stable oxygen reduction electrode. *Journal of Materials Chemistry A* **2014,** *2* (5), 1284-1293.
215. Corbel, G.; Mestiri, S.; Lacorre, P., Physicochemical compatibility of CGO fluorite, LSM and LSCF perovskite electrode materials with $La_2Mo_2O_9$ fast oxide-ion conductor. *Solid State Sciences* **2005,** *7* (10), 1216-1224.

216. Lee, S.; Bevilacqua, M.; Fornasiero, P.; Vohs, J.; Gorte, R., Solid oxide fuel cell cathodes prepared by infiltration of $LaNi_{0.6}Fe_{0.4}O_3$ and $La_{0.91}Sr_{0.09}Ni_{0.6}Fe_{0.4}O_3$ in porous yttria-stabilized zirconia. *Journal of Power Sources* **2009,** *193* (2), 747-753.
217. Van Der Heide, P., Systematic x-ray photoelectron spectroscopic study of $La_{1-x}Sr_x$-based perovskite-type oxides. *Surface and Interface Analysis: An International Journal devoted to the development and application of techniques for the analysis of surfaces, interfaces and thin films* **2002,** *33* (5), 414-425.
218. Crumlin, E. J.; Mutoro, E.; Liu, Z.; Grass, M. E.; Biegalski, M. D.; Lee, Y.-L.; Morgan, D.; Christen, H. M.; Bluhm, H.; Shao-Horn, Y., Surface strontium enrichment on highly active perovskites for oxygen electrocatalysis in solid oxide fuel cells. *Energy & Environmental Science* **2012,** *5* (3), 6081-6088.
219. Yang, T.; Huang, K., A bismuth attack at grain-boundaries of ceria-based electrolytes. *Journal of the Electrochemical Society*, Accepted.
220. Schuler, J. A.; Wuillemin, Z.; Hessler-Wyser, A.; Comminges, C.; Steiner, N. Y., Cr-poisoning in (La, Sr)(Co,Fe)O_3 cathodes after 10,000 h SOFC stack testing. *Journal of Power Sources* **2012,** *211*, 177-183.
221. Cacciuttolo, Q.; Vulliet, J.; Lair, V.; Cassir, M.; Ringuedé, A., Influence of pressure on the electrical and electrochemical behaviour of high-temperature steam electrolyser $La_{0.6}Sr_{0.4}Co_{0.2}Fe_{0.8}O_3$ anode. *Journal of Solid State Electrochemistry* **2018**, 1-9.